Dissertation zur Erlangung des Doktorgrades
der Fakultät für Chemie und Pharmazie
der Ludwig-Maximilians-Universität München

DELIVERY OF CHEMOTHERAPEUTICS BY METAL-ORGANIC NANOPHARMACEUTICALS

von

Benjamin Steinborn

aus

Dresden, Deutschland

2020

Erklärung

Diese Dissertation wurde im Sinne von § 7 der Promotionsordnung vom 28. November 2011 von Herrn Prof. Dr. Ernst Wagner betreut.

Eidesstattliche Versicherung

Diese Dissertation wurde eigenständig und ohne unerlaubte Hilfe erarbeitet.

München, den 17.12.2019

.....

Benjamin Steinborn

Dissertation eingereicht am 17.12.2019

1. Gutachter: Prof. Dr. Ernst Wagner

2. Gutachter: Prof. Dr. Stefan Wuttke

Mündliche Prüfung am: 05.02.2020

Meiner Familie

“I am always looking, like a child, for wonders I know I am going to find.”

Richard Feynman

Table of contents

1 Introduction

This chapter was partially adapted from:

B. Steinborn, P. Hirschle, M. Höhn, T. Bauer, M. Barz, S. Wuttke, E. Wagner, U. Lächelt. *Core-Shell Functionalized Zirconium-Pemetrexed Coordination Nanoparticles as Carriers with a High Drug Content*. Advanced Therapeutics **2019**, 2, 1900120.

B. Steinborn, U. Lächelt. *Metal-Organic Nanopharmaceuticals*. Pharmaceutical Nanotechnology **2020,** Manuscript accepted.

1.1 Chemotherapy and drug delivery by nanotechnology

Due to the wonders of modern life sciences and an overall increase in living standards, life expectancies in the industrialized world have improved considerably within the last 100 years and are expected to continue doing so.[1] Currently, the cumulative cancer lifetime risk for an individual is estimated at about 44%,[2] however, this number is expected to climb since cancer typically displays elevated incidence rates at older ages.[3]

Thankfully, our understanding of nanotechnology, medicine, physics, cancer biology and thereby possible points of intervention also grew significantly during the last decades and has led to the exploration of new curative strategies as illustrated by continuous progress with innovative concepts such as photodynamic therapy[4], antibodies[5], kinase inhibitors[6], radiotherapy[7], immunotherapy[8], antisense oligonucleotides[9] and chemotherapeutic nanoformulations.[10]

However, additional approaches are always needed since the small molecule chemotherapeutic treatment schemes frequently used in the clinic often display unfavorable pharmacokinetic properties leading to rapid drug excretion, limited tumor accumulation and major systemic toxicity. As a consequence, efficient tumor treatment requires high loading doses but the severe dose-limiting off-target effects determine a narrow therapeutic window, impair patient benefits in the clinical practice[11] and negatively affect therapeutic outcomes.

Such unfavorable pharmacokinetic properties also affect commonly used small molecule drugs and cannot be changed without derivatization which would very likely also impact their pharmacodynamics. However, nanotechnology offers a solution.

The first encounters with nanotechnology can be traced back to at least 300 – 400 A.D. where gold-silver alloyed nanoparticles, most likely serendipitously discovered and not understood at the time, gave the Lycurgus cup its fascinating ability to change color upon illumination.[12] Damascus steel swords forged at a similar age owed their exceptional strength to embedded wire-like nanoparticles and provide another example.[13]

It took us approximately another 1500 years to develop the technologies necessary to begin to understand, actively manipulate and harness phenomena at the nanoscale in a biomedical context.

At present, about 40 nanomedicines covering a wide range of indications such as cancer therapy[14], fungal diseases[15], viral vaccines[16], analgesics[17], photodynamic therapy[18] and imaging contrast agents[19] have received market approval.[20]

In the context of cancer treatment, current approaches in nanotechnology work towards ameliorating problems inherent to small molecule chemotherapeutics. Here, nanoparticles (NPs) are highly attractive materials for the utilization as drug carriers as their pharmacokinetic properties can be tuned without affecting pharmacodynamics of the enclosed drug.

NP drug delivery systems are therefore being investigated to overcome the poor selectivity and major side effects frequently associated with chemotherapy.[21]

Multiple factors contribute to the benefits of nanoparticular drug delivery.

Nanoformulations improve limited solubilities of hydrophobic drugs as exemplified by clinically approved propofol emulsions with droplet sizes between 100 and 300 nm.[22] Such a feature is also interesting for certain chemotherapeutics, for instance vincristine or taxol. As they lack sufficient aqueous solubilities, i.v. formulations require high concentrations of surfactants which in turn contribute to adverse reactions.[23]

Nanoformulations also enable targeted drug delivery by providing a particle surface that allows for modification with targeting ligands[24] or protect labile cargos by encapsulation.[25]

Additionally, if tailored to an adequate size range, NPs may utilize the leaky tumor vasculature[26] to passively extravasate to and accumulate in the tumor microenvironment based on the enhanced permeability and retention (EPR) effect.[27]

Whereas a minimum hydrodynamic NP diameter of about 5.5 nm is mandatory in order to prevent immediate renal clearance,[28] the optimal upper size limit strongly depends on the tumor type. A size below 12 nm seems to benefit delivery across the blood brain barrier,[29] pancreatic cancer favors NPs below 100 nm[30] and particles of approximately 300 nm benefit pulmonary delivery[31] which illustrates the importance of rational and precise size control based on the intended therapeutic application.

Surface charge and chemistry constitute additional critical parameters that must be considered since they influence protein corona formation[32], cytotoxicity[33], uptake[33], immune recognition[34] and circulation times[35] of nanomaterials.

As our understanding of the tumor microenvironment[36] is steadily increasing but nevertheless still limited, early research on nanoparticular chemotherapeutic drug delivery systems was primarily aimed at designing PEGylated nanocarriers with long circulation times and little systemic losses in order to maximize EPR-based tumor accumulation. A selection of FDA approved chemotherapeutic nanoformulations following this strategy is listed in **Table 1**.

Table 1 Selected chemotherapeutic nanoformulations with FDA approval

Name	Drug	Formulation	Company	Indication(s)	Approval	Ref.
Daunoxome	Daunorubicin	Liposome	Galen Pharm.	Kaposi sarcoma	1996	[14a]
Abraxane	Paclitaxel	Drug bound to Albumin	Celgene	NSCLC, metastatic breast cancer	2005	[14b]
Lipoplatin	Cisplatin	PEGylated Liposome	Regulon	Head and neck cancer, breast cancer	2012	[37]
Onivyde	Irinotecan	PEGylated Liposome	Merrimack Pharm.	Pancreatic cancer	2015	[38]
Doxil/Caelyx	Doxorubicin	PEGylated Liposome	Johnson & Johnson	Ovarian cancer, Kaposi sarcoma	1995	[39]

In contrast, **Table 2** lists chemotherapeutics that received FDA approval in 2019 and reveals an increasing importance of targeted treatments with all of the approved drugs belonging either to the class of highly selective antibodies or small molecules aimed at specific targets, a marked contrast to the broadly cytotoxic drugs with low selectivities developed during the earlier days of chemotherapy.

This provides a glimpse at what may be in store for cancer nanoparticles. So far, to the best of my knowledge, no actively targeted anticancer nanoformulation has received market approval, but encouraging *in vitro* and *in vivo* data - some of which will be discussed in chapter **1.3.** - allows for a cautiously optimistic outlook.

Table 2 Chemotherapeutics that received FDA approval in 2019. Data was scraped from reference [40].

Name	Drug	Type	Company	Indication(s)	Target
Balversa	Erdafitinib	Small molecule	Janssen Oncology	Urothelial carcinoma	Fibroblast growth factor receptor
Bavencio	Avelumab	Antibody	Merck and Pfizer	Advanced renal cell carcinoma	PD-L1
Cyramza	Ramucirumab	Antibody	Eli Lilly	Hepatocellular carcinoma	VEGFR2
Keytruda	Pembrolizumab	Antibody	Merck	Recurrent esophageal cancer	PD-L1
Nubeqa	Darolutamide	Small molecule	Bayer	Castration-resistant prostate cancer	Androgen receptor
Piqray	Alpelisib	Small molecule	Novartis	Metastatic breast cancer	PI3K
Polivy	Polatuzumab and Vedotin	Antibody drug conjugate	Genentech	Diffuse large B-cell lymphoma	CD79b
Rozlytrek	Entrectinib	Small molecule	Genentech	Non-small cell lung cancer	Tropomyosin receptor kinases A,B,C
Tecentriq	Atezolizumab	Antibody	Genentech and Roche	Extensive-stage small cell lung cancer	PD-L1
Turalio	Pexidartinib	Small molecule	Daiichi Sankyo	Symptomatic tenosynovial giant cell tumor	CSF1R
Venclextra and Gazyva	Venetoclax and Obinutuzumab	Small molecule and antibody	Genentech and AbbVie	Chronic lymphocytic leukemia	BCL-2 and CD20
Xpovio	Selinexor	Small molecule	Karyopharm Therapeutics	Multiple myeloma	Exportin 1

1.2 Metal-organic framework nanoparticles in a biomedical context

***Background**. This chapter provides an introduction to the underlying chemistry, key features and applications of metal-organic framework (MOF) nanoparticles. Due to the width of the field, it will briefly mention non-biomedical use cases but focus on MOFs in the context of chemotherapeutic drug delivery.*

Since their inception around 1990[41] and the subsequent establishment of the term by Prof. Yaghi, MOFs, in a broader sense also referred to as coordination polymers or crystalline porous scaffolds, have attracted considerable attention by the research community.

Due to their modular nature and the virtually unlimited choice of suitable building blocks, ten thousands of distinct MOF-like structures have been reported so far with hundreds of them also being porous to a varying degree.[42] Of all the possible candidates, **Table 1** depicts the subset of MOFs used within this thesis.

An explanation for the observed spike of publications (**Figure 1**) lies within their intriguing and highly attractive properties which have sparked research interest from multidisciplinary areas such as catalysis[43], gas storage[44], separation[45], sensing[46], drug delivery[47], photovoltaics[48], imaging[49], photodynamic therapy[4] and energy storage.[50]

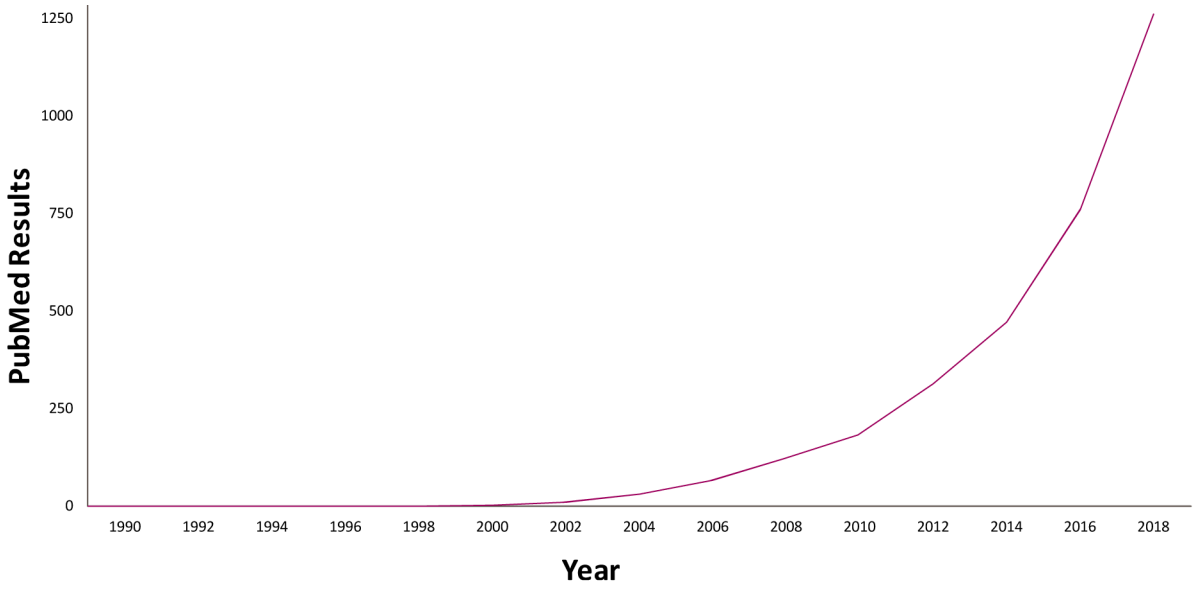

Figure 1 Development of PubMed hits for the search term “metal-organic framework” since 1990 illustrating the ever increasing research interest continuing to this day. Data was scraped from PubMed using reference [51].

In general, MOFs are composed of multivalent metal ions and polydentate organic linker molecules. During a typical MOF synthesis, discrete elementary cells, also referred to as secondary building units (SBU), are generated in a first step by coordinative metal-linker interactions.[52] Here, the spatial structure of the formed SBUs highly depends on the used metal ion and linker.[53] In a second step, cross-linking of individual SBUs by additional linker molecules gives rise to the MOF superstructure. **Scheme 1** depicts a simplified version of the assembly process with commonly used parameters.

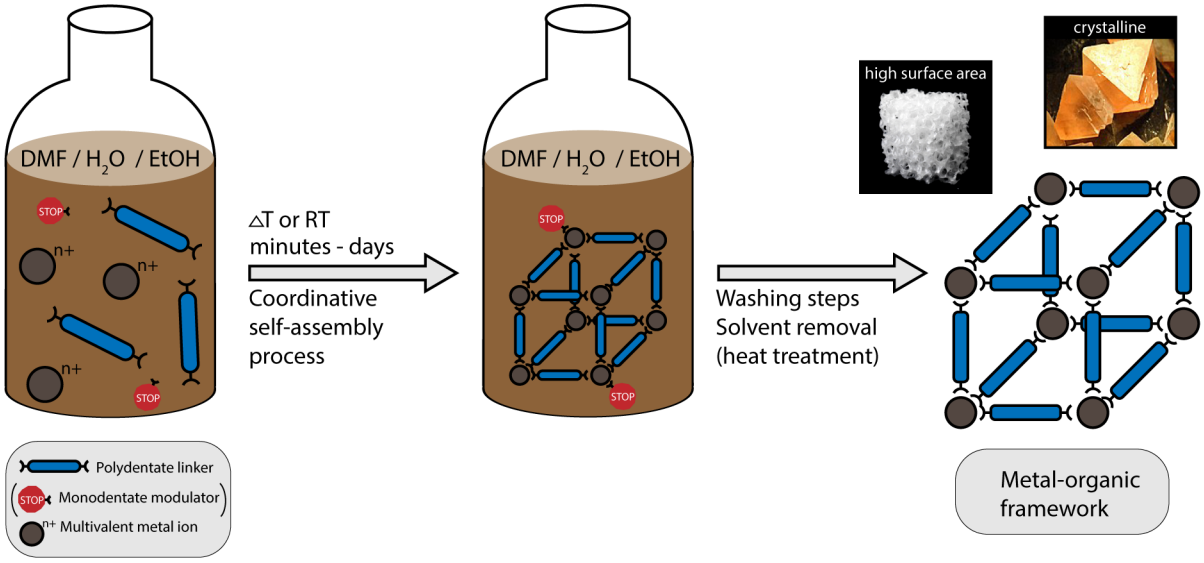

Scheme 1 Illustration of a synthetic approach used to generate MOFs. The scheme depicts a frequently used solvothermal reaction but should not be considered representative for all types of MOFs since their synthetic conditions are too diverse to be summarized within a single graphic. Blue bars serve as polydentate linker molecules, gray circles depict metal ions and the stop sign illustrates a monodentate modulator used for the synthesis of certain MOFs in order to control growth kinetics and the final particle size. The resulting framework has been simplified with regard to topology and the initial assembly of secondary building units (SBUs) is not shown.

From a materials science point of view, an especially prominent MOF feature lies within the very large surface areas that have undergone successive evolution with values reaching 310 $m^2\ g^{-1}$ by 1998[54], 3800 $m^2\ g^{-1}$ by 2005[55] and 5200 $m^2\ g^{-1}$ by 2009.[56] Today, selected MOFs exceed 7000 $m^2\ g^{-1}$[57] by BET nitrogen sorption which currently comprises the highest surface area reported for any type of nanostructure and easily surpasses other highly porous materials such as activated carbon (typically <1000 $m^2\ g^{-1}$)[58] and zeolites (typically around 500 $m^2\ g^{-1}$).[59]

It is also worth mentioning that pore sizes and affinities for selected cargo molecules can be tuned based on the chosen linker molecule.[60]

Considering that by surface areas, a stadium-sized soccer field would comfortably fit within one gram of the newest MOF generation, it is easy to see their enormous potential for applications such as catalysis and drug delivery.

Table 3 MOFs used within this thesis. MIL, Materials Institute Lavoisier; UiO, Universitetet i Oslo; HKUST, Hongkong University of Science and Technology; *fum*, fumarate; H_3BTC, benzenetricarboxylic acid; H_2BDC, benzenedicarboxylic acid.

Preparation technique	MOF	Metal ion	Linker component	Ref.
Microwave-assisted	MIL-88A	Fe^{3+}	Fumaric acid	[61]
Solvo/hydrothermal	MIL-100 (Fe)	Fe^{3+}	H_3BTC	[62]
Solvo/hydrothermal	UiO-66	Zr^{4+}	H_2BDC	[63]
Sonochemical	HKUST-1	Cu^{2+}	H_3BTC	[64]
Solvo/hydrothermal	Zr-*fum*	Zr^{4+}	Fumaric acid	[65]
Solvo/hydrothermal	MIL-101(Cr)	Cr^{3+}	H_2BDC	[55]

As particle size is another decisive attribute for a nanomaterial,[66] multiple approaches have been developed to control crystal growth rates and thereby final sizes of the obtained MOFs. Those strategies include optimizing reagent concentrations,[67] the used metal salt,[68] reaction temperature and duration,[61] control at the nucleation level by addition of a surfactant[69] and addition of monodentate carboxylate modulators as depicted in Scheme 1.[70]

At present, a wide range of functional motifs have been successfully used as the linking moiety as exemplified by MOFs employing linkers based on chemical entities such as carboxylates,[65] phenolates,[64] amino acids,[71] imidazolates[70] and sulfonates[72].

From a purely chemical perspective, a rich selection of metal ions appears initially suitable for MOF construction and, accordingly, frameworks based on metals such as iron,[61-62] zirconium,[63, 65] copper,[64] chromium,[73] zinc[70], gadolinium,[74] hafnium[75] and cadmium[76] have been reported.

However, with a biomedical application in mind, toxicity concerns narrow down the sensible choice considerably, yet little is known about MOF toxicity in general so far.

In a biomedical context, it seems like a viable strategy to employ linker molecules present in the human body *a priori* to MOF administration. A structure such as fumaric acid would address this requirement and additionally entails the advantage of partaking in the citric acid cycle[77] which offers a direct metabolization pathway without risking toxic intermediate formation.

Concerning the metal component, based on rat LD_{50} doses and *in vitro* studies utilizing HeLa cells, Horcajada *et al.* perceive Ca, Mg, Zn, Fe, Ti and Zr as most suitable. [42a, 78]

Wuttke *et al.* examined the nanosafety profile of three selected MOFs, MIL-100(Fe), MIL-101(Cr) and Zr-*fum*. Notably, it was found that even for the same MOF, toxicities and interactions with cells may differ according to effector cell types and applications.[79]

Baati *et al.* evaluated the *in vivo* toxicity of three iron-based MOFs, namely MIL-88A, MIL-100(Fe) and MIL-88B_4CH_3.[80] In their rat model, MOF doses between 100 and 200 mg/kg (remarkably, scaled to the body weight of an average person of 70 kg, this would correspond to high doses of 7-14 g MOF) did not result in changes of behavior, acute toxicities or deaths after 7 days. Apart from minor lung embolisms caused by pulmonal nanoparticle aggregates – an observation which was later actually utilized for a therapeutic application[81] - and a temporary spike in liver and spleen iron levels, no pathological organ chances were observed which illustrates the excellent tolerability of the screened iron-based MOFs.

Ruyra *et al.* investigated *in vivo* zebrafish embryo toxicities of selected MOFs and observed little to no toxicity for UiO-66, UiO-77, MOF-74 and Mg-MOF-74. Additionally, selected members of the Zeolitic imidazolate framework (ZIF) series of MOFs were evaluated. ZIFs are generated from tetrahedrally coordinated transition metal ions which are interconnected by imidazolate linkers. So far, approximately 100 ZIF topologies have been reported.[82] For the examined ZIF-7 and ZIF-8, strongly reduced hatching rates were observed.[83]

However, additional factors besides component and MOF toxicities have to be considered. For instance, Bellido *et al.* reported a heparin coating approach for MIL-100(Fe) which reduced complement activation, reactive oxygen species production and macrophage recognition[84] whereas Zimpel *et al.* found that coating Zr-*fum* with a polyglutamate-polysarcosine block-copolymer very similar to the one used within this thesis (chapter **3.2.3**) induced pH-independent colloidal stabilization in multiple environments such as water, protein-enriched buffer solutions and cell culture medium.[85] This constitutes an additional step towards mastering control of interactions occurring at the biointerface, a requirement for eventual clinical translation of MOF-based therapeutics.

Multiple strategies for the loading of cargos have been developed so far (**Scheme 2**). Due to the enormous porosities reported for certain MOFs, one approach lies within post-synthetically soaking porous MOFs in a small molecule solution (Scheme 2A). Here, both the properties of the utilized MOF and the drug dictate the loading efficiency. Although MOF scaffolds feature a certain flexibility,[86] cargos still need to be small enough to physically fit within the pores. Additionally, pore sizes are not the only limiting factor as the window sizes within the scaffold that limit the actual pore access are typically smaller than the pores themselves. In a chemotherapeutic context, many studies have employed such a loading mechanism for drugs such as cisplatin,[47b] methotrexate,[87] doxorubicin[88] and 5-fluorouracil.[89]

A different approach lies within postsynthetic covalent modification (Scheme 2B). For instance, typical MOF linkers modified with reactive amine groups – leading to structures such as 2-aminoterephthalic acid – are incorporated during synthesis and subsequently used as a cargo grafting site.[90] Frameworks such as MOF-46,[91] IRMOF-3[92] and NH_2-UiO-66[93] have been synthesized this way. The amines allow for stable cargo attachment due to covalent reactions,[94] but in a drug delivery setting, a possible drawback lies within reduced pharmacological activity as the molecular structure of the cargo is being modified. In a study using an UiO-67 derivative, azide- or acetylene-functionalized linkers were postsynthetically introduced into the framework by a linker exchange reaction.[95] Notably, the achieved incorporation of two distinct reactive groups allows for sequential and orthogonal click reactions.

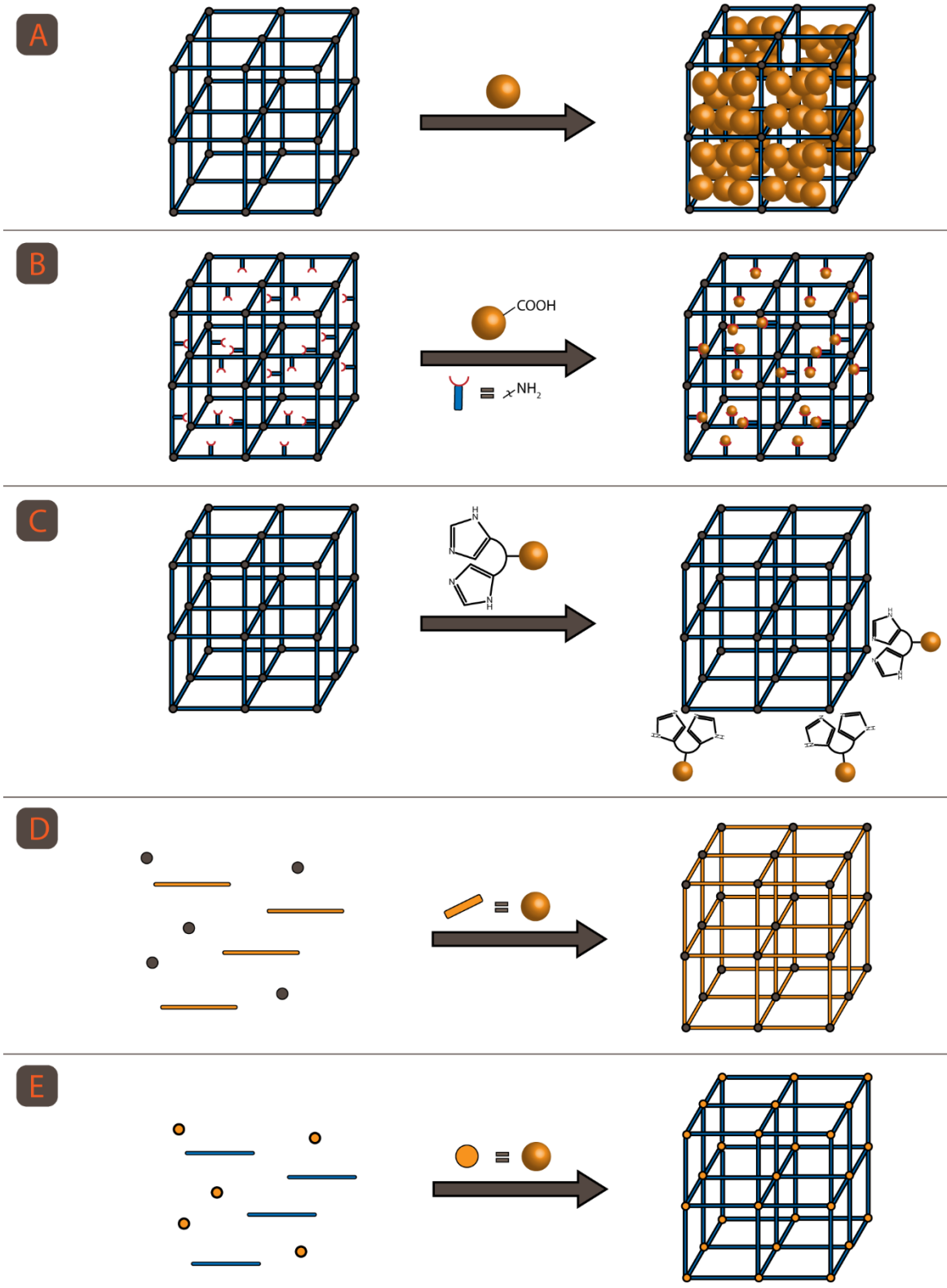

Scheme 2 MOF loading strategies. **A)** encapsulation into pores, **B)** covalent attachment exemplified by amine-modified linkers and a carboxylated cargo, **C)** coordinative attachment illustrated with a simplified His-tag **D)** direct framework incorporation by the intended cargo acting as a linker during MOF synthesis, **E)** incorporation of active metal ions during MOF synthesis.

Scheme 2C describes a coordinative surface anchoring strategy reported by Röder et al.[96] and utilizes coordinatively unsatured metal sites[97] (CUS) present on the MOF surface to reversibly attach cargos. Here, the desired cargo is initially modified with histidine tri- or hexapeptides and subsequently incubated with the MOF. An advantage lies within the broad range of possible cargos since the only requirement is a motif that allows for (reversible) His-tag modification but no intrinsic cargo affinity towards the chosen MOF is required. Additionally, multiple cargos may be co-delivered and the strategy is also suitable for proteins which are likely too bulky to fit within MOF pores. Conveniently, proteins are already routinely expressed with a (cleavable) His-tag as part of their structure.[98]

Scheme 2D depicts a strategy where the drug to be delivered directly serves as a building block for the MOF structure itself. The Lin group pioneered this approach for pharmacotherapy[75, 99] by synthesizing MOFs based on the photosensitizer 5,15-di(*p*-benzoato)porphyrin (H_2DBP) which contains two carboxylic acid groups and a rather rigid structure enabling it to act as the linker molecule. To the best of my knowledge, this currently represents the only example where APIs were directly utilized as MOF linker molecules.

For applications such as magnetic resonance imaging (MRI),[100] the metal ion providing the actual enhancement in contrast may also be directly incorporated into the framework during synthesis (Scheme 2E). Similarly, a MOF with an active metal component was designed for a radiotherapy application.[101] Here, the integrated Hf^{4+} mediates radiosensitization by X-ray attenuation.

However, when using active pharmaceutical ingredients (API) as linkers, it is difficult to predict if the synthesis will result in a MOF structure or rather lead to a nanoscale coordination polymer (NCP). As NCPs are structurally different from MOFs and also often directly created from APIs, the following chapter will introduce them in detail.

1.3 Nanoscale coordination polymers as multifunctional drug carriers

***Background**. Careful control of reaction parameters allows for the assembly of selected drug molecules with Lewis base functions into nanoscale coordination polymers (NCPs) by linkage through suitable metal ions. The following chapter distinguishes NCPs from MOFs, introduces recent developments of NCP research in the context of chemotherapeutic drug delivery and photodynamic therapy and additionally highlights potential advantages and applications for this rather novel class of nanomaterials.*

Although both MOFs and NCPs are generated by a coordinative bottom-up assembly approach, their properties may differ considerably as illustrated in **Scheme 3**.

As a rule of thumb, assembly at room temperature tends to lead to amorphous NCPs whereas solvothermal conditions favor the formation of crystalline MOFs.[102]

However, this rule just allows for an initial approximation and should be applied with care as exceptions do exist; both crystalline MOFs synthesized at room temperature[103] and crystalline NCPs synthesized under solvothermal conditions[104] have been reported.

Compared to MOFs of the later generation developed within the last twenty years that frequently feature satisfactory aqueous stabilities,[105] NCPs tend to be less stable in an aqueous environment which often necessitates stabilizing surface coatings.[106]

Although both MOFs and NCPs are held together by rather labile coordinative bonds, a possible explanation for the frequently observed lower NCP stabilities may lie within their typically non-crystalline structures.

Whereas for selected MOFs, certain regularly arranged bulky linkers sterically shield the metal coordination sites from water access and therefore generate an activation energy barrier[105a] which impairs linker displacement, the situation might be different for NCPs due to their less ordered structures potentially allowing for easier water access.

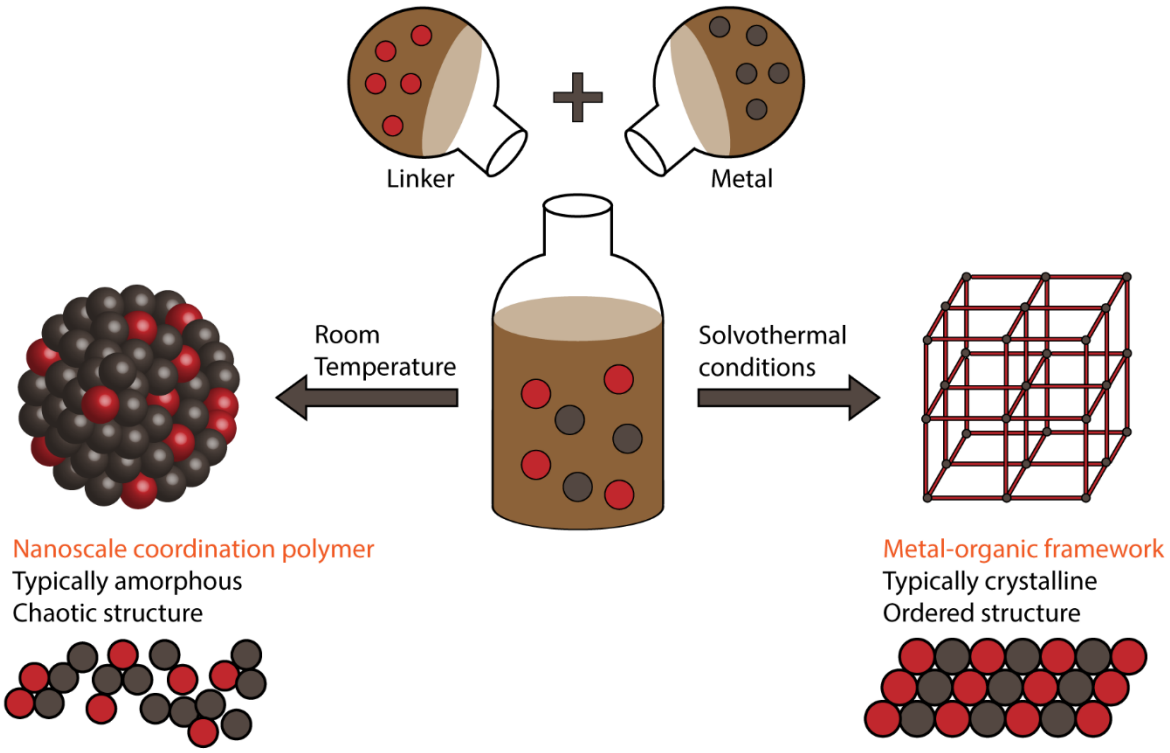

Scheme 3 Characteristic differences between NCPs and MOFs. Synthesis at room temperature (left) frequently favors the formation of non-crystalline NCPs whereas solvothermal conditions (right) tend to lead to crystalline MOFs. The scheme was adapted from reference [107].

Hypothetically speaking, if comparing a MOF and NCP structure, it could be envisioned that metal clusters within the MOF structure feature a higher average coordination number as the framework has more time to assemble in an orderly and regular fashion. With an elevated average coordination number, metal-ligand bond hydrolysis might be tolerated to a higher degree before the particle dissembles into its components.[105a] In case of identical coordination numbers, the highly regular crosslinking observed for MOFs might also result in their enhanced stabilities.

Thus, the NCP core is typically assembled in a first step and the obtained surface then subsequently coated with a stabilizing agent. Such a modification tends to be necessary in order to extend drug release profiles, prevent immediate burst release and increase particle degradation half-lives. Reported surface functionalization approaches include lipid bilayers[106c, 108], silica shells,[106b, 109] dopamine-modified alginate,[110] hyaluronic acid[111] and polyhistidine-PEG.[112] Additionally, selected coatings mediate colloidal stabilization which comprises an additional important requirement for a nanomaterial.

Another key aspect of NCPs lies within their very high material economy.[113] Here, in contrast to other drug delivery systems such as drug-loaded MOFs,[114] liposomes[115] or polymerosomes,[116] the cargo itself constitutes an essential building block of the drug delivery system. As a consequence, unprecedentedly high drug contents of up to 80% (weight/weight) have been reported.[117] Due to the simultaneous loading capacity for multiple different cargos, NCPs also provide the opportunity for spatiotemporal co-delivery of different agents thus allowing for combination therapies which makes them highly attractive for biomedical applications.

In a chemotherapeutic setting, numerous NCP formulations incorporating drugs such as doxorubicin[109, 117a, 118] (**Table 4**), platinum derivatives[106b, 106d, 112, 119] (**Table 5**) or photosensitizers[108a, 120] (**Table 6**) have been reported. For a subset of the summarized formulations, encouraging *in vivo* results were observed in chemotherapeutic mouse models. Of those, selected studies will be presented in detail as they illustrate the high clinical potential of NCP-based chemotherapeutic drug delivery.

Table 4 Selected nanoscale coordination polymers incorporating doxorubicin and their key properties. DOX, doxorubicin; bix, 1,4-bis(imidazol-1-ylmethyl)benzene; Ce6, chlorin e6.

Metal	Linker/Cargo	Preparation Technique	Drug Content [% w/w]	Surface Functionalization	Morphology	Size [nm, method]
Cu^{2+}, Fe^{3+}	DOX, Daunorubicin	Precipitation	67.4 and 9 (DOX/Cu), 48.4 and 16.4 (Dox/Fe)	None	Not reported	50-100 (SEM)
Zn^{2+}	DOX, Camptothecin, Daunomycin ,bix	Precipitation	up to 21	None	Not reported	controllable between 100-1500 (SEM, TEM)
Fe^{2+}	DOX, bix	Precipitation	40 (DOX)	Silica (TEOS), Folate targeting	Amorphous by XRD	150-250 (SEM/TEM)
Fe^{3+}	DOX, Polyphenol gallic acid	Microwave-assisted	48.3 (DOX)	None	Not reported	417 (FCG, DLS) 482 (FCG@Dox, DLS)
Hf^{4+}	DOX, chlorin e6, bis-(alkylthio)alkene,	Solvothermal	22.4 (Hf), 23 (Ce6), 45 (DOX)	Lipid bilayer, PEGylation	Core-shell	70 (as-synthesized NCP, TEM) 90 (NCP-Ce6-DOX-PEG, DLS)

Han *et al.* reported a formulation for NCP-based doxorubicin (DOX) delivery that additionally included polyphenol gallic acid to mitigate cardiotoxicity. Initially, the plain NCP scaffold was created from polyphenol gallic acid and Fe^{3+} (FGC). The scaffold was then loaded with DOX by coordinative interactions between deprotonated hydroxyl groups of the DOX anthracycline moiety and Fe^{3+}. As polyphenol gallic acid derivatives are investigated as adjuvants for chemotherapy,[121] this approach illustrates the aforementioned co-delivery of two active components. An *in vivo* therapeutic experiment utilizing H22 hepatoma xenografts in mice resulted in significantly enhanced tumor growth inhibition compared to free DOX. The treatment with FGC@DOX was also well tolerated. In contrast to free DOX, no loss of body weight and reduced cardial tissue lesions were observed.

Table 5 Selected nanoscale coordination polymers incorporating platinum drugs and their key properties. DSCP, c,c,t-(diamminedichlorodisuccinato)Pt(IV); bix, 1,4-bis(imidazol-1-ylmethyl)benzene; C18PMH-PEG, PEG-grafted poly (maleicanhydride-alt-1-octadecene); TEOS, tetraethyl orthosilicate; PVP, polyvinylpyrrolidon.

Metal	Linker/Cargo	Preparation Technique	Drug Content [% w/w]	Surface Functionalization	Morphology	Size [nm, method]
Tb^{3+}	DSCP	Precipitation	Not reported	PVP/TEOS, RGDfK-targeting	Amorphous by XRD	58 (DLS)
Zn^{2+}	bisphosphonic acid derivatives of Cisplatin or Oxaliplatin	Microemulsion	48 (Cisplatin) 45 (Oxaliplatin)	PEGylation	Amorphous by XRD	45 (DLS)
Zn^{2+}	Gemcitabine, Oxaliplatin	Microemulsion	30 (Oxaliplatin) 12(Gemcitabine)	Lipid bilayer, PEGylation	XRD not reported Spherical by TEM	40-50 (DLS)
Zn^{2+}	Cisplatin prodrug, Gemcitabine monophosphate, DSPE-siRNA	Microemulsion	25 (Cisplatin) 6 (siRNA)	Lipid bilayer	XRD not reported Spherical by TEM	105 (DLS)
Zn^{2+}, Ni^{2+}	DSCP, bix	Precipitation	56 (DSCP), 7.7 (Zn), 0.6 (Bix)	None	Amorphous by XRD	200 (DLS)
Ca^{2+}	Cisplatin prodrug	Precipitation	Not reported	polyhistidine-PEG	Amorphous by XRD	55 (DLS)

Multiple studies using formulations incorporating platinum drug derivatives also resulted in promising *in vivo* results. [106d, 119b, 119c, 122]

He *et al.* designed an NCP incorporating a cisplatin prodrug and siRNA for the combination therapy of chemoresistant ovarian cancer.[106d] The NCP co-delivers a bisphosphonate prodrug of cisplatin and pooled siRNAs targeting multiple multidrug resistance (MDR) genes.

The redox-responsive cisplatin prodrug was initially assembled into an NCP core by addition of Zn^{2+} ions and then coated by a reverse microemulsion approach leading to particles functionalized with DSPE-conjugated siRNA, cholesterol, DOPC and DSPE-PEG2k.

The *in vivo* efficiency of the formulation was then evaluated in subcutaneous SKOV-3 and intraperitoneal A2780/CDDP xenograft tumor mouse models which resulted in highly promising therapeutic outcomes as determined by strong tumor growth inhibitions.

Notably, repeated intraperitoneal injections of NCP-1/siRNAs were able to completely eradicate SKOV-3 tumors in 5 out of 6 mice. In an A2780/CDDP model, all tumors were eliminated which resulted in 100% survival for more than 90 days. This study thus illustrates the enormous potential of NCP-based platinum drug delivery.

Table 6 Selected nanoscale coordination polymers designed for photodynamic therapy and their key properties. TCPP, tetrakis(4-carboxyphenyl)porphyrin; pHis-PEG, polyhistidine-polyethyleneglycol; DSPC, 1,2-distearoyl-sn-glycero-3-phosphocholine; DSPE-PEG2K, 1,2-distearoyl-sn-glycero-3-phosphoethanolamine-N-[carboxy(polyethyleneglycol)-2000].

Metal	Linker/Cargo	Preparation Technique	Drug Content [% w/w]	Surface Functionalization	Morphology	Size [nm, method]
Ca^{2+}	AS1411 DNA aptamer, Chlorin e6, hemin	Precipitation	19.7 (AS1411), 4.45 (Ce6), 4.86 (Hemin)	pHis-PEG	XRD not reported Spherical by TEM	70 (DLS)
Hf^{4+}	tetrakis (4-carboxyphenyl) porphyrin	Solvothermal	54.6 (TCPP) 28.7 (Hf)	PEGylation	Cystalline	130 (DLS)
Zn^{2+}	cisplatin prodrug	Microemulsion	25 (cisplatin@core) 25 (pyrolipid@shell)	Pyrolipid, cholesterol, DSPC, DSPE-PEG2K	Core-shell	54 (DOPA-coated, DLS) 108 (NCP@pyrolipid, DLS)

He *et al.* combined chemotherapy and photodynamic therapy (PDT) into a core-shell NCP with a phospholipid-porphyrin (pyrolipid) coating for treatment of resistant head and neck cancers.[108a] The formulation was generated by initially assembling DOPA-capped particles from a mixture of a bisphosphonate cisplatin derivative, DOPA and Zn^{2+} by application of a reverse microemulsion strategy. PDT capacity and PEGylation were then added to the NCP by coating it with a mixture of pyrolipid, cholesterol, DSPC and DSPE-PEG2k giving rise to NCP@pyrolipid.

Evaluating NCP@pyrolipid uptake into SQ20B human head and neck cancer cells indicated a rapid uptake completed within 1h. Pharmacokinetic studies of NCP@pyrolipid in CT26 tumor bearing mice revealed prolonged component circulation half-lives. The *in vivo* antitumor efficiency was then investigated using a SQ20B mouse model. Whereas control tumors grew to approximate endpoint volumes of 1.6 cm^3, NCP@pyrolipid plus illumination resulted in drastic tumor shrinkage with final volumes of about 0.1 cm^3. TUNEL assay revealed a high apoptosis rate for NCP@pyrolipid plus illumination group (approximately 80 % TUNEL-positive cells) which additionally confirmed the potential of the NCP system for combined chemo- and photodynamic therapy.

In sum, this chapter traced the recent emergence of NCPs as a new class of nanomaterial with a broad range of possible biomedical applications such as drug delivery, PDT, cancer combination treatment, multimodal imaging and radiosensitization. A huge variety of suitable pharmaceutical building blocks combined with appropriate metal ions allows for innovative therapeutic and diagnostic nanosystems with clinical potential as illustrated by the presented *in vivo* studies.

1.4 Cancer treatment by pemetrexed and methotrexate

***Background**. This chapter briefly introduces the history, pharmacology and main applications of chemotherapeutic antifolate drugs with a focus on pemetrexed and methotrexate.*

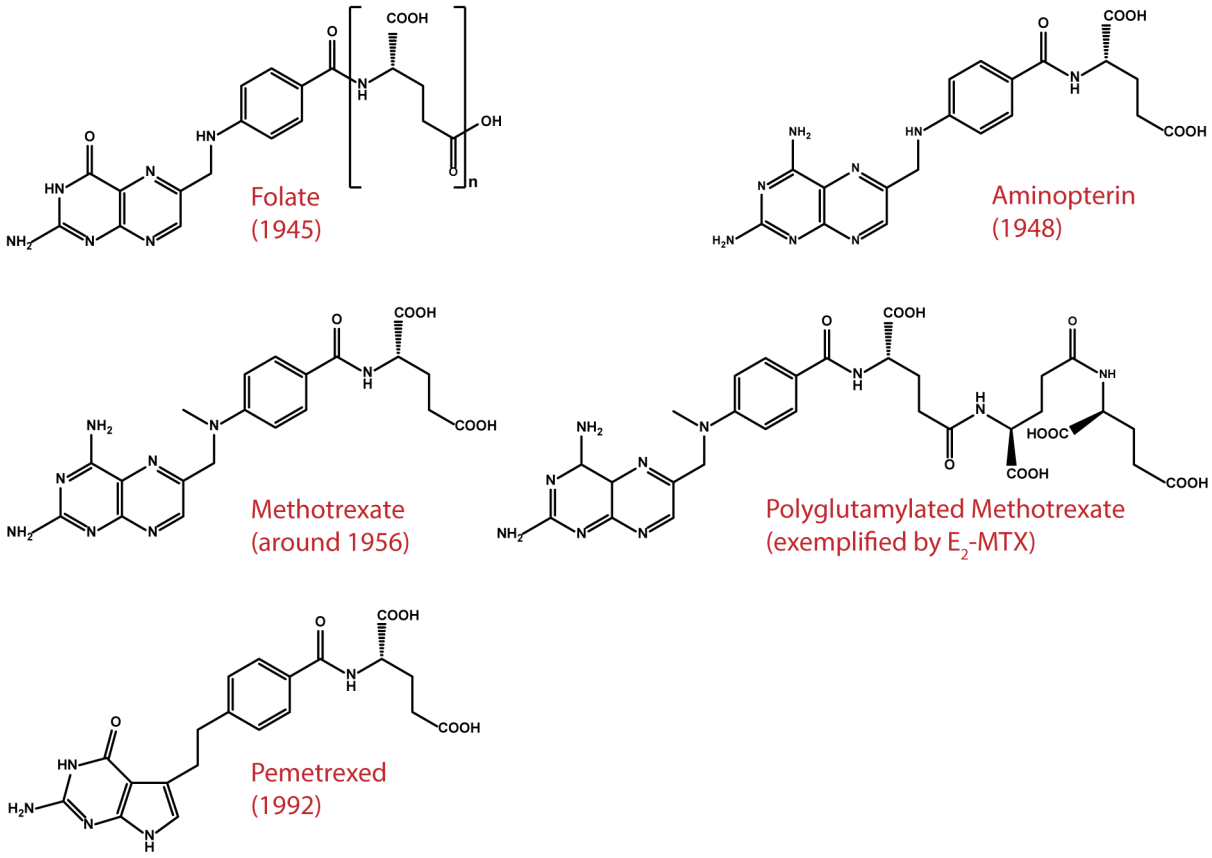

Scheme 4 Chemical structures of folate (top left), aminopterin (top right), methotrexate (mid left), a polyglutamylated methotrexate species (mid right) and pemetrexed (bottom left).

Since their discovery in the late 1940s, the class of antifolates, a selection of which next to folic acid is depicted in **Scheme 4**, has dramatically improved therapeutic outcomes for diseases such as pediatric acute lymphoblastic leukemia,[123] non-small cell lung cancer[124] and other maladies exemplified by psoriasis[125] and rheumatoid arthritis.[126] The development started in 1941 by the identification and isolation of folic acid, originally discovered in the context of antibiotics research.[127] In 1945, the newly discovered compound was then evaluated as a potential leukemia therapeutic and given to patients whose symptoms rapidly deteriorated. However, the observation sparked the hypothesis that folate antagonists might be useful therapeutic agents.[128]

In 1948, Farber *et al.* synthesized aminopterin, the first antifolate, which produced acute, but temporary, remission in children suffering from acute lymphocytic leukemia[129] and marked the dawn of the age of cancer chemotherapy. As aminopterin turned out to be too toxic and was difficult to synthesize,[128] the search for alternatives led to the development of structurally similar methotrexate (MTX) and its subsequent evaluation in an early clinical trial during the 1950s.[130]

To survive, cells have to perform constant *de novo* purine and thymidine generation as those structures are essential for the formation of DNA and RNA. The synthesis involves a complex, multi-step enzymatic interplay, a simplified version of which is shown in **Scheme 5**, and requires sufficient levels of fully reduced folates.

Antifolates mediate their therapeutic efficiency by competitively inhibiting selected enzymes within this pathway leading to a breakdown of DNA- and RNA synthesis. Here, dihydrofolate reductase (DHFR) plays a key role as it catalyzes two subsequent folate reduction steps. Initially, folate is taken up by cell and multiple uptake mechanisms are known. In this regard, the reduced folate carrier (RFC) mainly contributes to the uptake of reduced folate isoforms but displays a very low affinity for native folic acid (K_m 200-400 M)[128] which is preferably transported to the cytosol by the folate receptor (FR) with a very low K_d of 1 nM.[128] MTX is also taken up by the FR although its affinity towards it is lower compared to folate.[131] Additionally, the RFC contributes to cellular MTX entry and decreased RFC activity has been attributed to transporter-mediated MTX resistance[132] whereas the proton-coupled folate transporter (PCFT) supports folate uptake but also accepts pemetrexed (PMX) as a substrate.[133] In contrast, the adenosine triphosphate (ATP) binding cassette (ABC)[134] actively exports xenobiotics, including MTX and its polyglutamylated forms,[135] from the cytosol.

After their uptake, both folic acid and antifolates are subjected to polyglutamylation[136] at the γ-carboxyl moiety catalyzed by folylpolyglutamate synthase (FPGS). Here, typically 5-8 glutamate residues are attached[128] which results in cytosolic entrapment due to the added negative charge density and an increase in affinity towards enzymes partaking in one-carbon transfer reactions.[137] As both PMX[138] and MTX[139] undergo modification by FPGS which influences their intracellular concentrations, enzyme affinities and thus pharmacological activities, changes in polyglutamylation status comprise a major contributor to antifolate resistance.[140]

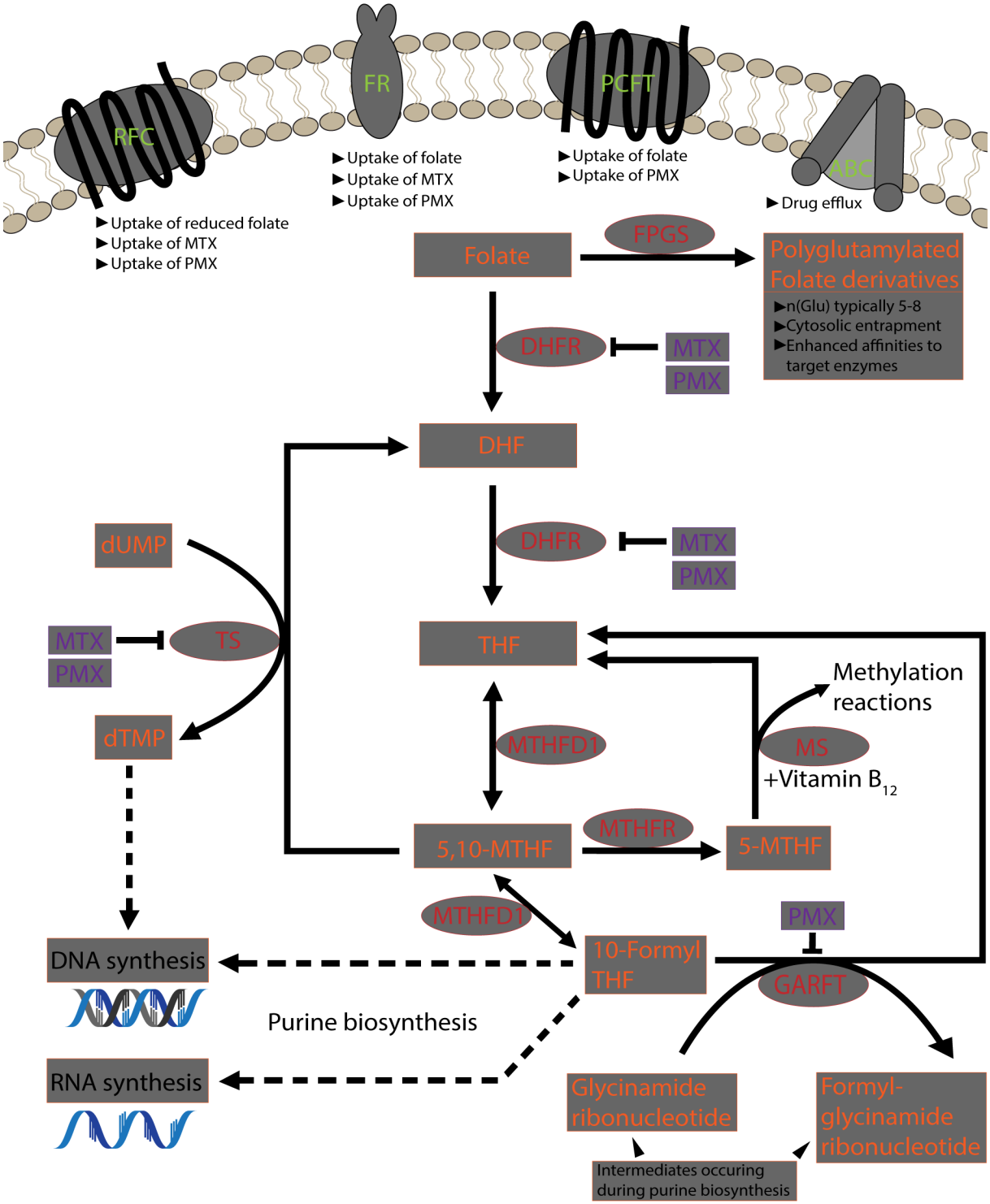

Scheme 5 Flowchart displaying key steps of folate metabolism, their connection to DNA- and RNA synthesis, main enzymes inhibited by chemotherapeutic drugs pemetrexed (PMX) or methotrexate (MTX) and main routes of uptake. Substrates and products are denoted in orange, enzymes in red, chemotherapeutics in purple and cellular uptake mechanisms in green. Abbreviations: DHF, dihydrofolate; THF, tetrahydrofolate; dUMP, desoxyuridinmonophosphate; dTMP, desoxythymidinemonophosphate; 5,10-MTHF, 5,10 methylenetetrahydrofolate; 5-MTHF, 5-methyltetrahydrofolate; 10-Formyl THF, 10-formyltetrahydrofolate. FPGS, folylpolyglutamate synthase; DHFR, dihydrofolate reductase; TS, thymidylate synthase; MTHFD1, methylenetetrahydrofolate dehydrogenase 1; MS, methionine synthase; MTHFR, methylenetetrahydrofolate reductase; GARFT, glycinamide ribonucleotide formyltransferase; RFC, reduced folate carrier; FR, folate receptor; PCFT, Proton-coupled folate transporter; ABC, ATP binding cassette. Intermediate steps not shown for simplicity are represented by dashed arrows.

After the poylglutamylation step, (DHF) is generated from folate and subsequently reduced again by the same enzyme to obtain fully reduced tetrahydrofolate (THF).

By conversion of THF, methylenetetrahydrofolate dehydrogenase 1 (MTHFD1) then generates 5,10-methylenetetrahydrofolate (5,10-MTHF) which serves as a cofactor necessary for the formation of desoxythymidinemonophosphate (dTMP) from desoxyuridinmonophosphate (dUMP) in a step catalyzed by thymidylate synthase (TS).

5,10-MTHF is also converted to 10-formyltetrahydrofolate (10-Formyl THF) which partakes in the synthesis of purine intermediates. Here, the scheme only shows the step catalyzed by glycinamide ribonucleotide formyltransferase (GARFT) due to GARFT being a target of PMX.

MTX reversibly inhibits DHFR but also targets TS[141] which results in DHF accumulation. As a consequence, a breakdown of purine biosynthesis occurs due to TS being directly inhibited. Additionally, the THF which is necessary to generate the 5,10-MTHF cofactor required by TS to function is no longer available in sufficient quantities due to upstream DHFR inhibition. Apart from inhibiting DHFR and TS, PMX additionally impairs GARFT and AICARFT, [128] enzymes partaking in the synthesis of purine intermediates.[142]

As ɣ-glutamylation enhances the bioactivity of both MTX[143] and PMX[144] and impaired polyglutamylation is additionally known to contribute to antifolate resistance,[140, 145] chapter **3.1.2** explored nanoparticular delivery of pre-polyglutamylated MTX derivatives by coordinative and/or electrostatic attachment to metal-organic framework (MOF) nanoparticles.

1.5 Aims of the thesis

Within this thesis, the results are structured in two main chapters each pursuing an individual goal.

Research as described in chapter **3.1.** investigated the delivery of chemotherapeutic MTX by attachment to metal-organic framework nanoparticles with the aim to create a delivery system for the drug.

To do so, a library of suitable peptide binding motifs that allow for MOF cargo attachment was initially identified and characterized using a panel of selected MOFs relevant in a biomedical context. This had to be done in order to obtain an understanding on how peptide tag properties such as length and charge influence tag binding capacities, since no such systematic screening has been conducted before. To maximize gained insights, the chosen MOFs had to include different metal components, linkers and porosities.

Then, one of the identified suitable tag binding motifs was applied for MOF-based delivery of chemotherapeutic pre-polyglutamylated MTX. Here, the pursued polyglutamylation approach was ultimately aimed at conferring MOF binding capacity to MTX while simultaneously addressing a known MTX resistance mechanism based on impaired polyglutamylation.

In contrast, results described in chapter **3.2**. explored the design and *in vitro* testing of a novel NCP based on chemotherapeutic PMX and zirconium ions. Here, the aim was the creation of a 'carrier-free' chemotherapeutic drug delivery system with a very high multifunctional efficiency[113] based on the previously observed glutamate-zirconium interactions. The drug-metal interactions were directly utilized for a controlled, coordinative bottom-up assembly of a small molecule chemotherapeutic drug into an NCP.

After establishing a suitable formulation method and subsequent characterization of the obtained drug-containing particle core, the thesis aimed at elucidating its *in vitro* behavior by assessing colloidal and serum stabilities and investigating the introduction of targeting ligands and their effect on uptake and toxicity. Ultimately, the aim was to deliver PMX and develop a formulation with the potential for co-delivery of other cargos as illustrated here with the co-integrated calcein.

2 Materials and Methods

2.1 Materials

2.1.1 Buffers and mobile phases

Table 1 Buffers and mobile phases used within this thesis.

Buffer	Composition
HEPES	20 mM HEPES, pH 7.4
PBS	0.137 M NaCl, 0.0027 M KCl, 0.01 M Na_2HPO4, 0.0018 M KH_2PO4, pH 7.4
HBG	20 mM HEPES, 5 % glucose, pH 7.4
TBE	89 mM Trizma® base, 89 mM boric acid, 2 mM EDTA-Na_2
10 mM HCl Size Exclusion Chromatography Mobile Phase	693 mL water, 300 mL acetonitrile, 7 mL 1 M HCl solution
HPLC aqueous phase containing 0.1 % (v/v) trifluoroacetic acid	999 mL water (purified and de-ionized), 1 mL trifluoroacetic acid
HPLC organic phase containing 0.1 % (v/v) trifluoroacetic acid	999 mL acetonitrile, 1 mL trifluoroacetic acid
Freeze-dry solvent	30% (v/v) acetonitrile in water

2.1.2 Solvents

Table 2 Solvents used within this thesis. Superscript numbers indicate respective purities.

Solvent	CAS-No.	Supplier
Acetonitrile[1]	75-05-8	VWR Int. (Darmstadt, Germany)
Dichloromethane[2]	75-09-2	Bernd Kraft (Duisburg, Germany)
*N,N-D*imethylformamide[3]	68-12-2	Iris Biotech (Marktredewitz, Germany)
Dimethyl sulfoxide[4]	67-68-5	Sigma-Aldrich (Munich, Germany)
Ethanol absolute[2]	64-17-5	VWR Int. (Darmstadt, Germany)
n-Hexane[5]	110-54-3	Brenntag (Mülheim/Ruhr, Germany)
Methyl-*tert*-butyl ether[6]	1634-04-4	Brenntag (Mülheim/Ruhr, Germany)
N-Methyl-2-pyrrolidone[3]	872-50-4	Iris Biotech (Marktredewitz, Germany)
Water[7]	7732-18-5	In-house purification

[1] HPLC grade, [2] analytical grade, [3] peptide grade, [4] BioReagent grade with a purity above 99.9 %, [5] purissimum, [6] synthesis grade; [7] purified and deionized with a conductivity below 0.055 µS cm^{-1}.

2.1.3 Reagents

Table 3 Reagents used within this thesis.

Reagent	CAS-No.	Supplier
1-Hydroxybenzotriazole hydrate	123333-53-9	Sigma-Aldrich (Munich, Germany)
2-Chlorotritylchloride resin	42074-68-0	Iris Biotech (Marktredewitz, Germany)
4-[N-(2,4-Diamino-6-pteridinylmethyl)-N-methylamino]benzoic acid hemihydrochloride hydrate	19741-14-1	
9-Acridinecarboxylic acid hydrate	332927-03-4	Sigma-Aldrich (Munich, Germany)
Ammonia solution 25%	1336-21-6	Carl Roth (Karlsruhe, Germany)
D-(+)-Glucose monohydrate	14431-43-7	Merck Millipore (Darmstadt, Germany)
EDTA disodium salt dihydrate	6381-92-6	Sigma-Aldrich (Munich, Germany)
Fmoc-Ala-OH	35661-39-3	Iris Biotech (Marktredewitz, Germany)
Fmoc-L-Glu-OtBu-OH	84793-07-7	Iris Biotech (Marktredewitz, Germany)
Fmoc-L-Glu-(OtBu)-OH	204251-24-1	Iris Biotech (Marktredewitz, Germany)
Fmoc-L-His(Trt)-OH	109425-51-6	Iris Biotech (Marktredewitz, Germany)
Fmoc-L-Lys(Boc)-OH	71989-26-9	Iris Biotech (Marktredewitz, Germany)
Folic acid	59-30-3	Sigma-Aldrich (Munich, Germany)
Formic acid	64-18-6	Sigma-Aldrich (Munich, Germany)
HEPES	7365-45-9	Biomol (Hamburg, Germany)
Hydrazine monohydrate	7803-57-8	Sigma-Aldrich (Munich, Germany)
Hydrochloric acid (1M)	7647-01-0	Sigma-Aldrich (Munich, Germany)
Methotrexate	133073-73-1	Sigma-Aldrich (Munich, Germany)
MTT	298-93-1	Sigma-Aldrich (Munich, Germany)
N-Fmoc-N″-succinyl-4,7,10-trioxa-1,13-tridecanediamine	172089-14-4	Sigma-Aldrich (Munich, Germany)
N,N-Diisopropylethylamine	7087-68-5	Iris Biotech (Marktredewitz, Germany)
N10-(Trifluoroacetyl)pteroic acid	37793-53-6	Clauson-Kaas A/S (Farum, Denmark)
Ninhydrin	485-47-2	Sigma-Aldrich (Munich, Germany)
Pemetrexed disodium heptahydrate	357166-29-1	Sigma-Aldrich (Munich, Germany)
Phenol	108-95-2	Sigma-Aldrich (Munich, Germany)
Piperidine	110-89-4	Iris Biotech (Marktredewitz, Germany)
Potassium cyanide	151-50-8	Sigma-Aldrich (Munich, Germany)
Pybop®	128625-52-5	Multisyntech GmbH (Witten, Germany)
Sephadex® G-10	9050-68-4	GE Healthcare (Freiburg, Germany)
Sodium hydroxide (anhydrous)	1310-73-2	Sigma-Aldrich (Munich, Germany)
Trifluoroacetic acid	76-05-1	Iris Biotech (Marktredewitz, Germany)
Triisopropylsilane	6485-79-6	Sigma-Aldrich (Munich, Germany)
Triton™ X-100	9002-93-1	Sigma-Aldrich (Munich, Germany)
Trizma® base	77-86-1	Sigma-Aldrich (Munich, Germany)
$ZrCl_4$ (anhydrous powder)	10026-11-6	Sigma-Aldrich (Munich, Germany)

2.1.4 Disposables and instrumentation for solid-phase synthesis

Synthesis utilizing microwave irradiation was carried out with a Biotage (Uppsala, Sweden) Initiator+ semiautomatic peptide synthesizer. Multisyntech (Witten, Germany) supplied disposable syringe microreactors (2 mL, 5 mL, and 10 mL) made from polypropylene (PP). All microreactors were purchased with pre-fitted polytetrafluoroethylene (PTFE) filters. For each individual synthesis, the reactor size was determined based on the used amount of resin and the manufacturers recommendations.

2.1.5 Cell culture

Table 7 Overview of the used cell lines and culture media.

Cell line	Description	Medium
KB	Human cervix carcinoma	RPMI-1640
L1210	Mouse lymphocytic leukemia	RPMI-1640
A549	Lung adenocarcinoma	RPMI-1640
H1299	Non-small cell lung carcinoma	RPMI-1640

Cell culture studies were carried out by Miriam Höhn (Pharmaceutical Biotechnology, Department of Pharmacy, LMU Munich). Invitrogen (Karlsruhe, Germany) supplied media, fetal bovine serum (FBS) and antibiotics. The absence of mycoplasm contamination was verified at regular intervals. Corresponding media used for the respective cell lines are listed in **Table 7**. In general, media were supplemented with 10 % FBS, 4 mM glutamine (stable form), 100 U/mL penicillin and 100 µg/mL streptomycin. Cells were cultured at 37 °C and 5 % CO_2. Upon reaching approximately 80 % confluency, adherent cells were detached from the collagen-coated culture flasks by addition of 1 mL trypsin-EDTA solution (Invitrogen, Karlsruhe, Germany) and subsequent incubation. After 5 minutes, cell detachment was quenched by addition of PBS and cells were split by transferring an aliquot of detached cells to a new culture flask pre-supplemented with medium. After approximately 20 passaging cycles, cells were generally discarded and replaced with freshly thawed aliquots. With the exception of experiments involving L1210 suspension cells, prior to performing cell-based experiments, respective cells were seeded at the desired density and generally allowed to settle for 24 hours.

2.2 Methods

Selected method descriptions were adapted from the following references:

B. Steinborn, P. Hirschle, M. Höhn, T. Bauer, M. Barz, S. Wuttke, E. Wagner, U. Lächelt. *Core-Shell Functionalized Zirconium-Pemetrexed Coordination Nanoparticles as Carriers with a High Drug Content*. Advanced Therapeutics **2019**, 2, 1900120.

P. Zhang, **B. Steinborn**, U. Lächelt, S. Zahler, E. Wagner, *Biomacromolecules* **2017**,18, 2509.

A. Zimpel, N. Al Danaf, **B. Steinborn**, J. Kuhn, M. Höhn, T. Bauer, P. Hirschle, W. Schrimpf, H. Engelke, E. Wagner, M. Barz, D. C. Lamb, U. Lächelt, S. Wuttke. *Coordinative Binding of Polymers to Metal-Organic Framework Nanoparticles for Control of Interactions at the Biointerface*. ACS Nano **2019**, 13, 3884.

2.2.1 Loading a 2-chlorotrityl chloride resin with an Fmoc-protected amino acid

Typically, 1000 mg 2-chlorotrityl chloride resin (1 eq, corresponding to 1.6 mmol chloride) were pre-swollen in anhydrous DCM for 30 minutes, the DCM was then removed by vacuum filtration. Then, a mixture of the first Fmoc-protected building block (0.5 eq amino acid per eq chloride, dissolved in 1:1 (v/v) dry DCM and DMF, 5 mL per gram resin) and DIPEA (3 eq.) were added to the reactor and subsequently incubated under agitation for 60 minutes. The solution was removed by vacuum filtration, replaced with a capping mixture consisting of 4 mL DCM, 3 mL MeOH and 500 µL DIPEA per gram resin and incubated under agitation for 30 minutes in order to transform residual free chlorides into unreactive methoxy ethers. The resin was washed (3 × DMF, 3 × DCM, 10 mL each per gram resin) and approximately 60 mg wet resin were drawn for Fmoc-quantification, dried under high vacuum and split into three samples. 20% piperidine in DMF (v/v, 1 mL) was added to each sample and incubated under agitation for 60 min (25 °C, 600 rpm). The samples were then vortexed and given 2 min for the beads to settle. 25 µL supernatant of each sample were diluted by addition of 975 µL DMF and measured at 301 nm against an equally diluted 20 % piperidine in DMF blank utilizing a Genesys 10S UV−vis photometer (Fisher Thermo Scientific, U.S.A.). For each sample, the resin load was calculated according to the following formula: resin load [mmol/g] = (A × 1000)/(m [mg] × 7800 × df) with df as a dilution factor. The average of three values gave the respective resin load. The remaining resin was Fmoc deprotected by 4 × 10 min treatment with 20 % piperidine in DMF, washed (3 × DMF, 3 × DCM), dried under high vacuum and stored at 4 ° C.

2.2.2 General description of a solid phase synthesis cycle

After pre-loading the resin with the first building block as described in **2.2.1.** and swelling it in DCM for 30 minutes, a cycle of iterative coupling and deprotection steps with the respective building blocks was carried out until the final structure was obtained which was then cleaved from the resin. If not stated otherwise, coupling steps were generally performed with 4 eq HOBt, 4 eq PyBOP, 8 eq DIPEA and 4 eq Fmoc-building block-OH. The respective molar amount of free amine present on the resin beads was regarded as 1 eq. In case of structures synthesized manually, the activating reagents and the building block were dissolved in 1:1 DCM/DMF. For synthetic approaches utilizing the automated synthesizer, DCM was replaced with NMP. After each coupling step, a Kaiser test (**2.2.3.**) was performed to verify the absence of free amines which would indicate non-quantitative couplings. Upon a negative Kaiser test, the protective group was removed (Fmoc: 4x 10 min 20% (v/v) piperidine in DMF, TFA: 4 × 30 min 1:1 25 % (v/v) ammonia solution in water and DMF) followed by a washing step (3x 1 min DMF, 3x 1 min DCM) and another Kaiser test performed subsequently to verify successful deprotection. **Table 6** provides an overview of such a synthetic cycle for structures synthesized manually, **Table 7** depicts those parameters for structures synthesized utilizing a Biotage (Uppsala, Sweden) Initiator+ semiautomatic peptide synthesizer and microwave irradiation. **Scheme 1** shows a graphical representation of a typical coupling cycle.

Table 8 Steps of a manual synthetic cycle

Step	Description	Solvent	Volume	Time
1	Coupling	DCM/DMF 50/50	5 mL/g resin	90 min
2	Wash	DMF, DCM	10 mL/g resin	3 x 1 min DMF 3 x 1 min DCM
3	Kaiser test	-	-	-
4	Fmoc deprotection	20 % piperidine in DMF	10 mL/g resin	4 x 10 min
5	Wash	DMF, DCM	10 mL/g resin	3 x 1 min DMF 3 x 1 min DCM
6	Kaiser test	-	-	-

Table 9 Steps of a synthetic cycle using a semiautomatic peptide synthesizer

Step	Description	Solvent	Volume	Time
1	Coupling	NMP/DMF	5 mL/g resin	12 min at 50°C
2	Cooling	-	-	3 min without heat
3	Coupling	NMP/DMF	5 mL/g resin	12 min at 50°C
4	Wash	DMF	8 mL/g resin	5 x 1 min
5	Fmoc deprotection	20 % piperidine/DMF	7 mL/g resin	4 x 10 min
6	Wash	DMF	8 mL/g resin	5 x 1 min

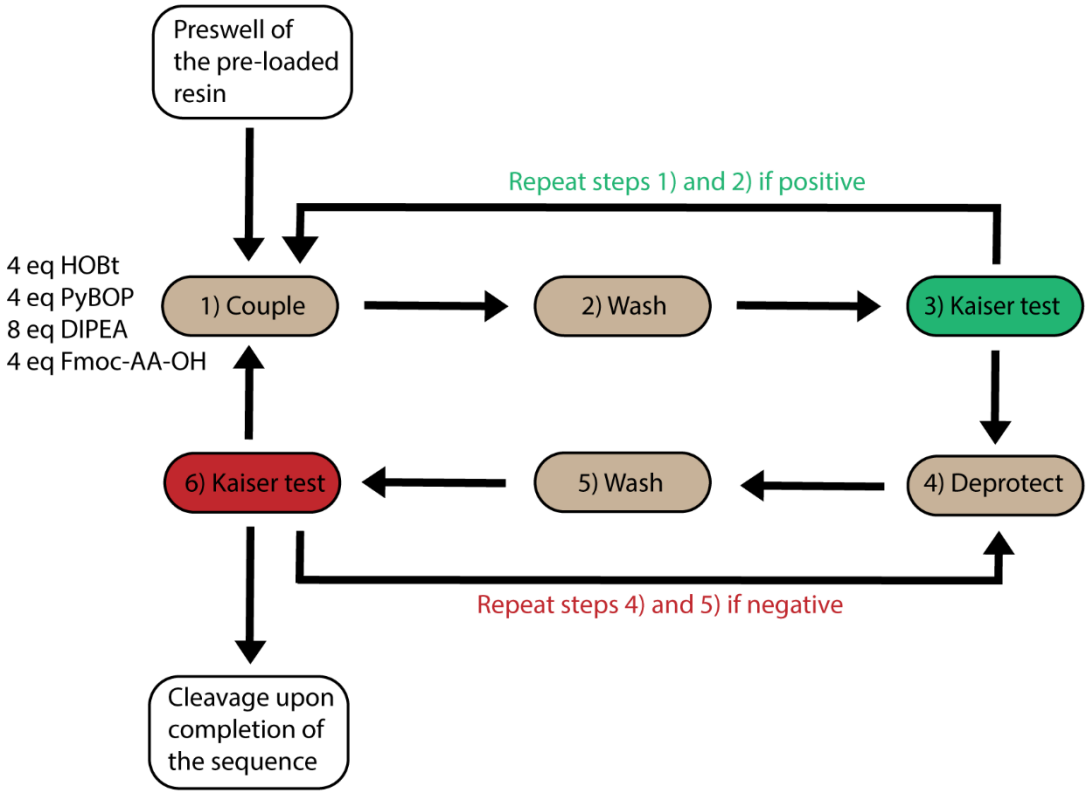

Scheme 6 Graphical representation of a typical coupling cycle. Steps 1) through 6) were repeated with the respective building block to be coupled until the final sequence was obtained and cleaved from the resin. The preswell step was performed only once at the beginning.

2.2.3 Kaiser test

Qualitative evaluation of free amines was performed based on the Kaiser test. A small amount of resin (typically approximately the tip of a spatula) washed with DCM was transferred into a 1.5 mL Eppendorf reaction tube and laced with a drop of each 80 % phenol in EtOH (w/v), 5 % ninhydrin in EtOH (w/v) and 20 µM potassium cyanide (KCN) in pyridine (mL aqueous 0.001 M KCN and 49 mL pyridine). The tube was then vortexed, briefly centrifuged, punctured at the top to allow for pressure equalization and incubated under agitation for 4 minutes at 99 °C. The absence of free amines was indicated by a pale yellow color whereas in case of residual free amines a deep blue color could be observed.

2.2.4 Cleavage and purification of structures generated by solid phase synthesis

In order to maximize yields, all resins were fully dried under high vacuum prior to cleavage. Structures were then cleaved from resins with a mixture of trifluoroacetic acid (TFA), triisopropylsilane (TIS) and water (95 : 2.5 : 2.5, v/v). The cleavage cocktail was dosed based on the amount of resin (10 mL g^{-1}). After 90 minutes of incubation under agitation, the cleavage solution was concentrated by nitrogen flow, dropwisely precipitated into 40 mL of MTBE and n-hexane (1:1, v/v) which had been pre-cooled at – 80 °C. After precipitation, the tube was shaken vigorously, centrifuged (10 minutes, 4000 rpm, Megafuge 1.0R, Heraeus, Hanau, Germany) and the supernatant removed. The obtained pellets were dried under nitrogen flow, dissolved in 30% acetonitrile in water (v/v), frozen in liquid nitrogen and freeze-dried (Christ Alpha 2–4 LD plus, Martin Christ Gefriertrocknungsanlagen GmbH, Osterode, Germany). Purity was evaluated by MALDI-TOF and, if necessary, RP18-HPLC. In case of a low purity, synthesized structures were purified by size exclusion chromatography utilizing an Äkta purifier system (GE Healthcare Bio-Sciences AB, Uppsala, Sweden) equipped with a Sephadex G-10 column and 30 % acetonitrile (v/v) in 10 mM hydrochloric acid as the mobile phase.

2.2.5 Particle size and zeta potential

Size and zeta-potential measurements were performed at a backscattering angle of 173° using the Nano Series Nano-ZS Zetasizer equipped with DTS-1070 folded capillary cuvettes (Malvern Instruments, Malvern, Worcestershire, United Kingdom). For size measurements, an equilibration time of 0 s was set and the attenuator was adjusted automatically. Measurements in HEPES-buffered glucose were performed at 25 °C with a solvent refractive index of 1.330 whereas a temperature of 20 °C and a solvent refractive index of 1.3617 were used for EtOH. Each sample was measured three times with at least six subruns each and z-averages, PDIs, and zeta potentials were reported as mean ± standard deviation. Zeta potential measurements were carried out in HEPES-buffered glucose (HBG) as triplicates with 10–15 subruns each and the zeta potential values were then calculated by the Malvern Zetasizer software (version 7.11) based on the Smoluchowski equation.

2.2.6 Synthesis of metal-organic framework nanoparticles

Table 10 MOFs used within this work and the literature describing their synthesis.

MOF	Dispersant	Storage	Reference
MIL-88A	EtOH	Room temperature	[61]
MIL-100(Fe)	EtOH	Room temperature	[62]
MIL-101(Cr)	EtOH	Room temperature	[146]
UiO-66	EtOH	Room temperature	[147]
Zr-*fum*	EtOH	Room temperature	[65]
HKUST-1	EtOH	Room temperature	[148]

Used MOFs were kindly synthesized and provided by Patrick Hirschle (Department of Chemistry, LMU Munich) and Dr. Andreas Zimpel (Department of Chemistry, LMU Munich). Table 10 lists respective storage conditions, dispersants and original publications describing the synthesis.

2.2.7 Evaluation of metal-organic framework peptide tag binding capacities

Directly prior to the experiment, a 10 mg ml^{-1} stock solution of the respective MOF in HBG buffer (20 mM, pH 7.4) was prepared by centrifuging its ethanolic stock solution (10 min,10000 rpm, Eppendorf tabletop centrifuge), carefully removing the supernatant by gently tapping the inverted tube on a paper towel and redispersing the pellet in HBG. In case of residual aggregates, especially prominent for MIL-88A, MOFs in HBG were briefly sonicated. For each MOF and peptide structure, five aliquots of the respective peptide-STOTDA-acridine structure in HBG (1 mM, 130 µL, 130 nmol) were prepared in 1.5 mL microcentrifuge tubes. Individual amounts of HBG buffer (20 mM, pH 7.4) were then added to each tube in such a fashion that the tube volume totaled 1000 µL once the respective amount of MOF in HBG was added. In the next step, the MOF in HBG (25 µg, 50 µg, 100 µg, 250 µg, 500 µg; corresponding to 2.5 µl, 5 µL, 10 µL, 25 µL, 50 µL 10 mg mL^{-1} MOF stock in HBG, respectively) was added, the tubes then briefly vortexed and incubated (Eppendorf tabletop shaker, 25 °C, 600 rpm, 15 min). After incubation, all samples were centrifuged (5 min,14000 rpm, Eppendorf tabletop centrifuge) and 100 µL of supernatant were carefully transferred to a microcuvette and photometrically measured at 360 nm against 20 mM HBG 7.4 as a blank. The concentration of peptide present in the supernatant was then determined using individual calibration curves of the respective peptides in HBG (6 data points between 0 and 150 µM, measured at 360 nm, R^2 of each curve > 0.99). The concentration of peptide bound by the respective MOF amount was then calculated according to the following formula: c(bound peptide) = 130 µM – c(supernatant). As the total sample volumes were set to 1000 µL, the determined bound peptide in µM equals the absolute amount of bound peptide in nmol. For each parameter, two individual samples were measured.

2.2.8 Evaluation of metal-organic framework E_n-MTX binding capacities

En-MTX bindings were determined with the assay setup described in **2.2.7** except for individual calibration curves being used and the photometric detection being carried out at a wavelength of 330 nm instead.

2.2.9 Nanoparticle uptake evaluation by confocal microscopy

Respective experiments were conducted by Miriam Höhn, Department of Pharmacy, LMU Munich. Cells were seeded in eight well-chamber slides (Thermo Fisher Scientific, 20000 cells in 300 µL medium per well) 1 day prior to recording the images and cultured at 37 °C and 5 % CO_2. On the day of the experiment, the medium was exchanged for 240 µL of fresh medium. The NPs were added in 60 µL HBG per well. After 1 h of incubation, the treatment solutions were replaced with fresh medium and the cells were incubated for additional 2 h at 37 °C and 5% CO_2. Cells were then fixated with 4 % paraformaldehyde in PBS (30 min incubation, room temperature). After fixating the cells, each well was washed once more with 400 µL PBS. Nuclei were stained with DAPI (2 µg mL^{-1}) and F-Actin was labeled with phalloidin-rhodamine (1 µg mL^{-1}). After 30 min of light-protected incubation at room temperature, the staining mixture was removed and replaced with 300 µL PBS per well. Images were then recorded on a Leica-TCS-SP8 confocal laser scanning microscope equipped with an HC PL APO 63 × 1.4 objective. DAPI emission was recorded at 460 nm and calcein at 530 nm. All images were processed utilizing the LAS X software from Leica.

2.2.10 Scanning electron microscopy

Measurements were carried out by Dr. Steffen Schmidt, Department of Chemistry, LMU Munich, Germany. The respective NP stock solutions in EtOH were concentrated approximately tenfold (by centrifugation and redispersion in a smaller volume of EtOH) and subsequently spotted onto a hydrophobic SEM sample carrier. After drying overnight in a dust protected environment, the samples were sputtered with carbon (three cycles of carbon vacuum deposition) and their morphology was then characterized using a Dual beam FEI Helios G3 UC SEM operated at 3 kV. Particle sizes were determined by recording high-resolution images, correcting them for contrast and brightness and subsequently measuring 100 particles using the ImageJ software (version 1.50i). The obtained sizes were reported in nanometers as average ± standard deviation. The elemental composition was analyzed during SEM measurements by energy dispersive X-ray spectroscopy (EDX) using an Oxford Instruments X-Max N80 device.

2.2.11 Synthesis of Zr-PMX NPs

A mixture of 416 µL 10 mM $ZrCl_4$ (1 eq,4.16 µmol, freshly dissolved in bi-distilled water), 50 µL 1 M HCl and 48.5 µL formic acid (100 eq.) was prepared in a 50 mL falcon tube and stirred at medium speed using a magnetic stirrer (solution I). In a separate 5 mL tube, 488 µL 15 mg mL^{-1} pemetrexed disodium heptahydrate (3 eq, 12.48 µmol, dissolved in bi-distilled water) was mixed with 3 mL EtOH absolute (solution II). Solution II was then quickly added to solution I while stirring. The mixture was further stirred at medium speed for 45 min. Afterwards, the reaction batch was split into three 1.5 mL polystyrene microcentrifuge tubes and centrifuged (Eppendorf tabletop centrifuge, 14 000 rpm, 1 min, Eppendorf GmbH, Hamburg, Germany). The supernatants were removed and the three pellets unified in 1 mL fresh EtOH absolute. The concentrated NP stock solution was then washed an additional two times with EtOH absolute (1 mL EtOH absolute and 1 min @ 14 000 rpm centrifugation per washing step). The washed NPs were redispersed in 1 mL EtOH absolute by gentle pipetting and subsequently sonicated for 5 min (20 °C, power 9) using a VWR USC THD/HF Ultrasonic Cleaner (VWR International GmbH, Darmstadt, Germany).

2.2.12 Synthesis of Zr-Calcein-PMX NPs

Zr-PMX NPs containing calcein were prepared identically to Zr-PMX NPs with the exception of solution II additionally containing 17.85 µM calcein (12.5 µL 5 mM calcein were added to solution II prior to mixing solutions I and II).

2.2.13 Determination of zirconium content by ICP-AES

A total of 1 mL Zr-PMX NPs in EtOH was transferred to a weighed polystyrene microcentrifuge tube, centrifuged (1 min, 14 000 rpm, Eppendorf tabletop centrifuge) and the supernatant was carefully discarded. The NP pellet was then dried under high vacuum for approximately 24 h followed by approximately 4 h drying at 90 °C. Next, the Eppendorf caps were weighed again and the dried NPs digested in 69% (v/v) HNO_3 for trace analysis (Aristar, VWR) and subsequently diluted with bi-distilled water to 3% (v/v) HNO_3. The samples were then analyzed for their Zirconium content by ICP-AES (CCD simultaneous ICP AES Vista RL by Agilent, suction time 35 s, stabilization time 45 s, power 1.25 kW). The following wavelengths were determined: 257.47, 327.307, 339.198, 343.823, and 349.619. Utilizing this method, three independent samples were prepared and analyzed and the zirconium content was reported as average mass percentage ± standard deviation.

2.2.14 Evaluation of crystallinity by X-ray diffraction

XRD spectra were obtained with a Stadi MP STOE transmission diffractometer system with Cu Kα1 radiation (λ = 1.54060 Å) and a Ge(111) single crystal monochromator. All samples were prepared by fixating the dried samples between two polymer foils. Diffraction patterns were recorded with a DECTRIS solid-state strip detector MYTHEN 1K in a transmission setup derived from Debye–Scherrer geometry using a step size of 4.71° and a counting time of 120 s per step. For data analysis, the WinXPOW RawDat v3.0.2.5 software package was used.

2.2.15 Determination of PMX content by HPLC

Zr-PMX NPs in EtOH were synthesized as described above. A total of 200 µL of the synthesized Zr-PMX NPs in EtOH was then mixed with 1 mL 500 mM EDTA pH 8.2 and 300 µL bi-distilled water. Three independent samples were prepared and incubated for 72 h at 25 °C under constant shaking (500 rpm, Eppendorf tabletop shaker, Eppendorf GmbH, Hamburg, Germany). In order to avoid EDTA precipitation, the lysed NPs were subsequently diluted with an equal volume of 0.1% (v/v) trifluoroacetic acid (TFA) in bi-distilled water and the PMX released from the NPs was then quantified by HPLC (Hitachi Chromaster, YMC RP-18 column, 50 µL injection volume, PMX retention time 10.847 min, monitoring @ 225 nm, solvents bi-distilled water + 0.1% TFA, HPLC-grade acetonitrile (ACN) + 0.1 % TFA (0–2.5 min: 1% ACN + 0.1% TFA, 2.5 – 11 min: increase to 41.4 %, 11–12 min: increase to 100 %, 12–14 min: wash with 100 %). Using a PMX calibration curve (six data points between 0 nmol and 5 nmol, R^2 = 0.9976) and the PMX molecular weight of 427.411 g mol^{-1}, the mass of PMX present in each sample was calculated. To obtain the drug loading of PMX within the NP, the total mass of NP present in each sample was determined by transferring 1 mL Zr-PMX NPs in EtOH to a weighed 1.5 mL polystyrene microcentrifuge tube, centrifuging (1 min, 14 000 rpm, Eppendorf tabletop centrifuge) and removing the supernatant very carefully to avoid loss of material. The NP pellet was then dried under high vacuum for approximately 48 h followed by approximately 4 h drying at 90 °C. The average of three mass determinations was then used to calculate the mass of NP present in each HPLC sample. The fraction of PMX in the NP (w/w) was subsequently calculated according to the following formula: [µg PMX in the HPLC sample/µg NP in the HPLC sample] × 100%.

2.2.16 Thermogravimetric analysis

Thermogravimetric analysis was carried out with a thermomicrobalance (Netzsch, STA 449 C Jupiter) by applying a heating rate of 10 °C min^{-1} up to 900 °C. A total of 7.425 mg of material was heated under synthetic air (N2/O2 mixture) with a flow rate of 25 mL min^{-1}. For data evaluation, the Proteus—Thermal Analysis (v.4.3) software was used.

2.2.17 BET sorption measurements

The nitrogen sorption isotherm was measured at 77 K with a Quantachrome Autosorb-1 iQ. Dried NPs were degassed at 60 °C under high vacuum for 38 h prior to the measurement. Evaluation of the sorption data was carried out using the ASiQwinTM software (Version 3.0, Quantachrome Instruments). BET surface areas were calculated employing the linearized form of the BET equation. With a relative pressure range between 0.15 and 0.27, this resulted in a correlation coefficient >0.999 with a positive C constant. The adsorption isotherm was then used to calculate the pore size distribution by employing the quenched solid density functional theory (QSDFT, N2 at 77 K on carbon, cylindrical pores adsorption branch).

2.2.18 Silica coating of Zr-PMX-NPs

A mixture of 3 µL *N*[1]-(3 trimethoxysilylpropyl)diethylenetriamine (TMSP) and 1 mL EtOH absolute and was prepared in a 50 mL falcon tube and stirred at low to medium speed with a magnetic stirrer. In a separate vial, 400 µL Zr-PMXNPs in EtOH were pre-diluted with 2 mL EtOH absolute and briefly vortexed. The prediluted Zr-PMX NPs were then added dropwise to the diluted TMSP solution within approximately 2 min and stirred for 5 min at low to medium speed. After 5 min, the polymerization process was initiated by addition of 60 µL 5M HCl. The tube was then stirred at low to medium speed for 3 h. Afterward, the reaction batch was split into three 1.5mL polystyrenemicrocentrifuge tubes, centrifuged (1min, 14 000 rpm, Eppendorf tabletop centrifuge) and the three pellets were unified in 1 mL fresh EtOH absolute. The sample was washed two more times with EtOH absolute (1 mL, 1 min@14 000 rpm, Eppendorf tabletop centrifuge). After the final washing step, the pellet was redispersed in 1 mL EtOH absolute and sonicated for 5 min (20 °C, power9) using the VWR USC THD/HF Ultrasonic Cleaner (VWR International GmbH, Darmstadt, Germany). Zr-Calcein-PMX NPs were coated with TMSP using the same protocol.

2.2.19 Serum stability of Zr-PMX@TMSP NPs

For each sample, 1 mL of Zr-Calcein-PMX@TMSP NPs in EtOH was centrifuged (1 min, 14 000 rpm, Eppendorf tabletop centrifuge) and the supernatant was removed carefully to avoid loss ofmaterial. The pellet was then redispersed in 1mL 10% (v/v) fetal bovine serum and subsequently incubated at 37 °C for 30 min. After the incubation, the samples were centrifuged (5 min, 14 000 rpm, Eppendorf tabletop centrifuge) and 100 µL of supernatant was diluted with 100 µL 0.1% (v/v) TFA in bidistilled water. The amount of released PMX present in the supernatant was then quantified by HPLC using a sample volume of 100 µL and the instrumentation described in section “Determination of PMX Content by HPLC.” To obtain 100% release values to normalize to, a triplicate with respective equal amounts of NP was centrifuged (1 min, 14 000 rpm, Eppendorf tabletop centrifuge), the supernatants were carefully discarded and the pellets were redispersed in 1 mL lysis buffer (500 mM EDTA pH 8.2) and incubated approximately 72 h (37 °C, 500 rpm). The set was then quantified by HPLC and the average of the determined PMX content was used as 100% value. The amount of released PMX for the serum-incubated samples was then calculated according to the following formula: [PMX in supernatant/PMX in lysis sample] * 100%. For each time point, a set of independent triplicates was prepared and analyzed and the percentage of released PMX was reported as average ± standard deviation.

2.2.20 Synthesis of pGlu$_{31}$-*b*-pSar$_{160}$-N$_3$

pGlu$_{31}$-*b*-pSar$_{160}$-N$_3$ was kindly synthesized and provided by Tobias Bauer (PhD student at the Institute of Organic Chemistry, Johannes Gutenberg-Universität Mainz, 55099 Mainz, Germany) according to the following method. All monomers were prepared according to the Fuchs–Farthing method with diphosgene as phosgene source and purified by recrystallization (Glu(OtBu)-NCA) or sublimation (SarNCA) as reported previously.[149] The synthetic pathway to azide-modified poly(l-glutamic acid)-block-poly(sarcosine) was adapted and modified from Yoo et al. and Schäfer et al.[150] Briefly, poly(γ-tert-butyl-l-glutamic acid)-*block*-poly(sarcosine) (pGlu (OtBu)-*b*-pSar) was prepared via sequential N-carboxyanhydride (NCA) polymerization initiated by neopentylamine. A total of 407.6 mg (1.78 mmol; 31 eq.) of γ-tert-butyl-l-glutamic acid

(Glu(OtBu))-NCA was weighed into a pre-dried Schlenk-flask, dissolved in mixture of 1:1 THF and DMF (both dried and freshly distilled) at a concentration of 100 g L^{-1}, cooled to 0 °C, and a solution of neopentylamine (5.0 mg; 57.4 µmol; 1.0 eq.) in 0.5 mL of DMF was added. After completed Glu(OtBu)-NCA consumption, as monitored by FT-IR spectroscopy, a solution of sarcosine- NCA (1.06 g; 9.17 mmol; 160 eq.) in 5.0 mL of DMF was added and the polymerization was continued at 10 °C. For azide end-group modification, pentafluorphenyl-4-azidobutanoate (33.9 mg; 0.115 mmol, 2.0 eq.) and N,N-diisopropylethylamine (DIPEA) (53 µL; 0.304 mmol; 5.0 eq.) were added and the solution was stirred at room temperature for 18 h. To react residual-free end groups, acetic anhydride (54 µL; 0.57 mmol; 10 eq.) and DIPEA (195 µL; 1.11 mmol; 20 eq.) were added and the solution was stirred for 1 day. The obtained block copolymer was purified by repetitive (3x) precipitation/centrifugation (4500 rpm, 15 min, 4 °C) into a mixture of n-hexane and diethyl ether (2:1). The product (pGlu $(OtBu)_{31}$-*b*-$pSar_{160}$-N_3) was dried in vacuo and obtained as a white powder (846 mg, 86%).

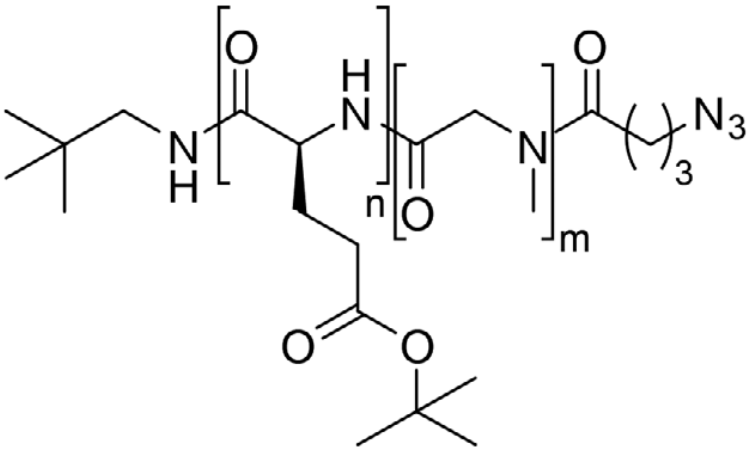

^{1}H NMR: pGlu $(O^tBu)_n$-*b*-$pSar_m$-N_3 (400 MHz, CD_2Cl_2), δ [ppm] = 8.45−8.11 (22 H, br, −**NH**−CO−CH−), 4.40−3.82 (323 H (1n + 2m), br, −CO−**CH**−NH + −CO−**CH_2**−NCH_3−), 3.20−2.80 (454 H (3m), m, −**NCH_3**−CO−), 2.66−1.70 (140 H, m, −**CH_2−CH_2**−), 1.53−1.36 (285 H, s + br, **−O−$C(CH_3)_3$**), 0.94−0.83 (9 H, br CH_2**−$C(CH_3)_3$**). HFIP-GPC: Mn = 39.5 kg mol−1, Mw = 45.4 kg mol−1; Đ = 1.15.

For deprotection, 800 mg of pGlu $(O^tBu)_{31}$-b-$pSar_{160}$-N_3 was dissolved in 16 mL of a mixture of 45:45:5:5 DCM/TFA/TIPS/water over 3 h in a Schlenk-flask with constant stirring. Polymers were precipitated into ether, centrifuged in sealed Falcon tubes and the precipitate was dialyzed against aqueous $NaHCO_3$ and water, followed by lyophilization (yield 80%). Successful deprotection was verified by ^{1}H NMR.

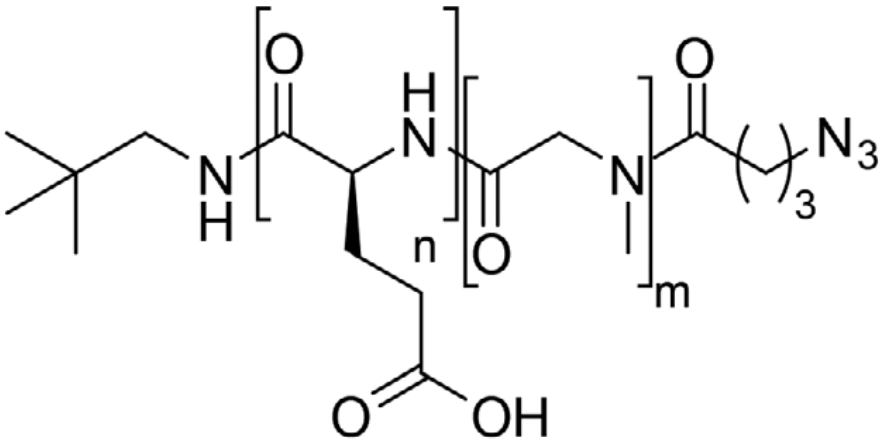

^{1}H NMR: pGlu (COOH)n-*b*-$pSar_m$-N_3 (400 MHz, D_2O), δ[ppm] = 4.50−4.00 (490 H, (1n + 2m), m, HN−**CH_2**−CO + HN−**CH**−CO), 3.30−2.72 (669 H (3m), m **NCH_3**), 2.33−1.70 (195 H (2n), m, **CH_2**−**CH_2**), 0.77-0.71 (9H, s, −**$C(CH_3)_3$**). HFIP-GPC: Mn = 29.4 kg mol−1, Mw = 35.1 kg mol−1; Đ = 1.19.

HFIP-GPC:

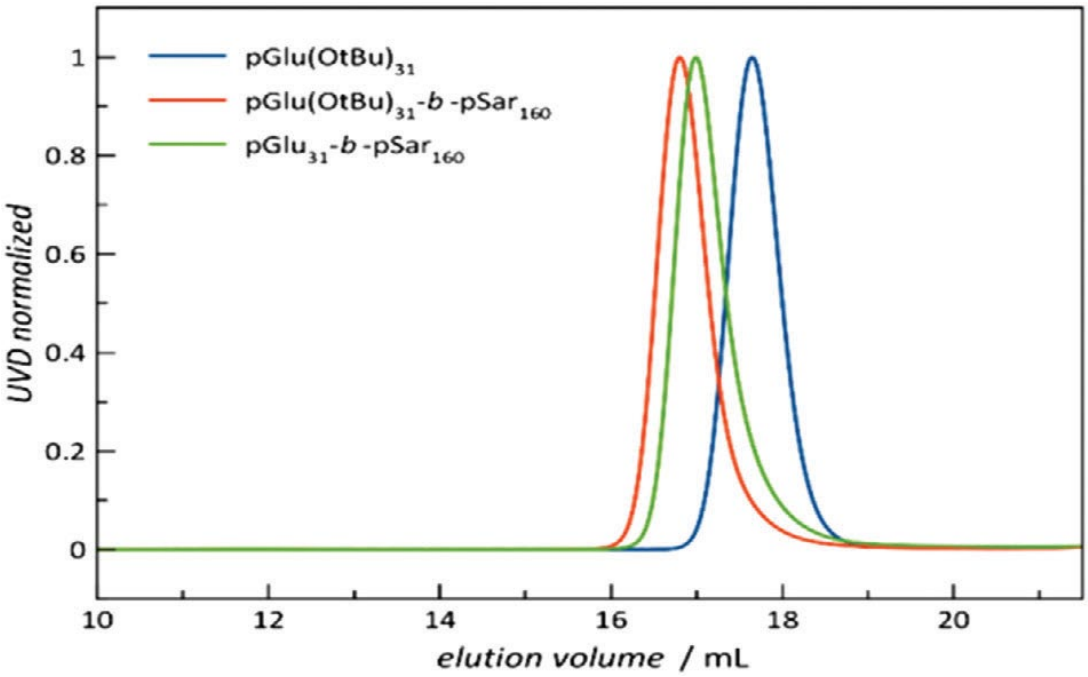

2.2.21 Synthesis and purification of pGlu$_{31}$-*b*-pSar$_{160}$-Folate

Pglu$_{31}$-Psar$_{160}$-FolA was synthesized by reacting pGlu$_{31}$-*b*-pSar$_{160}$-N$_3$ with a DBCO-Folate conjugate, referred to here as DBCO-FolA, (folic acid-lysine-DBCO; gamma-COOH of folic acid coupled to alpha-amine of lysine, epsilon amine of lysine coupled to DBCO-carboxylic acid).[151] A total of 3 mg pGlu$_{31}$-*b*-pSar$_{160}$-N$_3$ (1 eq, 189.9 nmol) was dissolved in 168 µL 1 mg mL^{-1} DBCO-FolA (1 eq, 189.9 nmol) in HBG (20 mM, pH 7.4). The mixture was incubated overnight and dialysed for 2 days at 4 °C against Millipore water. A Spectra/Por prewetted RC tubing dialysis membrane with a molecular weight cutoff of 2 kD was used and the water was changed once after approximately 24 h. The purified compound was snap frozen in liquid nitrogen, freeze-dried (Christ Alpha 2–4 LD plus, Martin Christ, Gefriertrocknungsanlagen GmbH, Osterode, Germany) and dissolved in bi-distilled water at 1 mg mL^{-1}.

2.2.22 Synthesis and purification of pGlu$_{31}$-*b*-pSar$_{160}$-Transferrin

Transferrin from human plasma (50 mg, 1 eq., 0.67 µmol) was dissolved in 1 mL HEPES buffer (20 mM, pH 7.4). DBCO-PEG4-NHS ester was dissolved in DMSO (20 mg mL^{-1}) and 43.5 µL (0.87 mg, 2 eq., 1.3 µmol) was added to the transferrin solution. The reaction mixture was incubated for 3 h at room temperature under gentle shaking (25 °C, 400 rpm). The solution was then purified by size exclusion chromatography using an ÄKTA purifier system (GE Healthcare), a Sephadex G25 super fine-size exclusion column and HEPES buffer (20 mM, pH 7.4) as a mobile phase. The collected fractions containing the DBCO-modified transferrin were pooled and the protein concentration was determined by Bradford assay.[152] By pooling the fractions, 4.75 mL DBCO-PEG4-transferrin with a concentration of 105 µM corresponding to a total yield of approximately 79% was obtained. Next, pGlu$_{31}$-*b*-pSar$_{160}$-N$_3$ (3 mg, 1.1 eq, 189.9 nmol) was dissolved in 1.81 mL of the obtained DBCO-PEG4-transferrin (1 eq, 209 nmol) and the mixture was incubated overnight. The resulting transferrin-modified polymer was diluted with HEPES to a final concentration of 1 mg mL^{-1}, used without further purification and stored at 4 °C.

2.2.23 Synthesis and purification of pGlu$_{31}$-*b*-pSar$_{160}$-AF647

DBCO-AlexaFluor647 (Jena Bioscience GmbH, Jena, Germany) was dissolved in DMSO at 1 mg mL^{-1}. A total of 455 µL of the dissolved DBCOAlexafluor647 (1.2 eq., 403 nmol) was then used to dissolve 5.3 mg pGlu$_{31}$-*b*-pSar$_{160}$-N$_3$ (1 eq, 335 nmol). The obtained mixture was then incubated overnight using an Eppendorf tabletop shaker (25 °C, 400 rpm). On the next morning, the product was dialyzed for about 48 h at 4 °C against bi-distilled water. Prior to adding the reaction batch to the dialysis membrane (Spectra/Por prewetted RC Tubing, MWCO 2 kD), the membrane was rinsed with bi-distilled water to remove the azide antifouling agent. Bi-distilled water was then added to the sample to reduce the DMSO content to approximately 20% v/v as a precaution in order to safeguard membrane integrity. During the dialysis step, the water was changed once after approximately 12 h, minor precipitation of blue product within the dialysis bag was observed. After dialysis, the sample was snap frozen in liquid nitrogen, freeze-dried over 2 days (Christ Alpha 2–4 LD plus, Martin Christ, Gefriertrocknungsanlagen GmbH, Osterode, Germany) and dissolved in bi-distilled water at a final concentration of 1 mg mL^{-1}.

2.2.24 pGlu$_{31}$-*b*-pSar$_{160}$-N$_3$ coating of Zr-PMX@TMSP NPs

pGlu$_{31}$-*b*-pSar$_{160}$-N$_3$ was prepared as an aqueous 1 mg mL^{-1} stock solution. For the dose titration studies, x µL polymer corresponding to x µg polymer was added to a 5 mL polystyrene tube and stirred at medium speed. Next, ethanolic Zr-PMX@TMSP NPs were centrifuged (1 min, 14000 rpm, Eppendorf tabletop centrifuge). The supernatant was carefully removed and the particles were redispersed in an equal volume of HBG (20 mM, pH 7.4). The particles in HBG were then sonicated for 1 min. Next, 500 µL of Zr-PMX@TMSP NPs in HBG were added dropwisely to the stirred polymer solution over approximately 2 min. The solution was stirred for additional 3 min and the obtained polymer-coated Zr-PMX@TMSP NPs were sonicated for 1 min (power 9, 20 °C) using the VWR USC THD/HF Ultrasonic Cleaner (VWR International GmbH, Darmstadt, Germany).

2.2.25 pGlu$_{31}$-*b*-pSar$_{160}$-FolA coating of Zr-PMX@TMSP NPs

To obtain folate-targeted Zr-PMX@TMSP NPs, a mixture of 1 mg mL^{-1} Pglu$_{31}$- Psar$_{160}$-N_3 and 1 mg mL^{-1} pGlu$_{31}$-*b*-pSar$_{160}$-FolA was prepared in a 5 mL Eppendorf tube stirred at medium speed. A total of 500 µL of Zr- PMX@TMSP NPs in HBG was added dropwisely to the stirred polymer solution over approximately 2 min. The solution was stirred for an additional 3 min and the obtained polymer-coated Zr-PMX@TMSP NPs were sonicated for 1 min (power 9, 20 °C) using the VWR USC THD/HF Ultrasonic Cleaner (VWR International GmbH, Darmstadt, Germany). For the polymer dose titration experiments, a total of 25 µL polymer containing various percentages pGlu$_{31}$-*b*-pSar$_{160}$-FolA was used. For the uptake experiments by confocal microscopy and MTT assays, 500 µL of Zr-PMX@TMSP NPs in HBG was coated with a fixed amount of 25 µg polymer containing 25% folate-modified polymer (6.25 µL 1 mg mL^{-1} pGlu$_{31}$-b-pSar$_{160}$-FolA + 18.75 µL pGlu$_{31}$-*b*-pSar$_{160}$-N_3) as described above.

2.2.26 pGlu$_{31}$-*b*-pSar$_{160}$-Transferrin coating of Zr-PMX@TMSP NPs

To obtain transferrin-targeted Zr-PMX@TMSP NPs x µL 1 mg mL^{-1} pGlu$_{31}$-*b*-pSar$_{160}$-transferrin (nomalized to polymer content) was prepared in a 5 mL polystyrene microcentrifuge tube stirred atmedium speed. A total of 500 µL of Zr PMX@TMSP NPs in HBG was added dropwisely to the stirred polymer solution over approximately 2 min. The solution was stirred for another 3 min and the obtained polymer-coated Zr-PMX@TMSP NPs were sonicated for 1 min (power 9, 20 °C) using the VWR USC THD/HF Ultrasonic Cleaner (VWR International GmbH, Darmstadt, Germany). For the dose titration experiment, various amounts (0– 50 µL) pGlu$_{31}$-*b*-pSar$_{160}$-transferrin were used. For the uptake experiments by confocal microscopy, 500 µL of Zr-PMX@TMSP NPs in HBG was coated with a fixed amount of 25 µg pGlu$_{31}$-*b*-pSar$_{160}$-transferrin as described above.

2.2.27 Colloidal stability studies of Zr-PMX@TMSP-NPs ± pGlu$_{31}$-*b*-pSar$_{160}$-N$_3$

For the HBG stability experiment, 500 µL Zr-PMX@TMSP NPs in HBG were coated with 25 µg pGlu$_{31}$-*b*-pSar$_{160}$-N$_3$ as described above and incubated using an Eppendorf tabletop shaker (37 °C, 400 rpm). Every 24 h, 75 µL sample was drawn, diluted with 645 µL HBG and size, PDI and zeta potential were determined by DLS. For the PBS stability experiment, Zr-PMX@TMSP-NPs were coated with 25 µg pGlu$_{31}$-*b*-pSar$_{160}$-N3 and incubated as described above. Then, 200 µL of the coated NPs in HBG were added to 800 µL PBS (20 mM, pH 7.4). Every 24 h, 180 µL sample was withdrawn, diluted with 540 µL PBS and then the size, PDI, and zeta potential were determined as described earlier.

2.2.28 Serum stability of pGlu$_{31}$-*b*-pSar$_{160}$-N$_3$@Zr-PMX@TMSP NPs

In a 5 mL polystyrene microcentrifuge tube, 25 µL pGlu$_{31}$-*b*-pSar$_{160}$-AF647 was stirred at medium speed. A total of 500 µL Zr-PMX@TMSP NPs in HBG was added dropwisely to the stirred polymer solution over approximately 2 min. The solution was stirred for another 3 min and the obtained polymer-coated Zr-PMX@TMSP NPs were sonicated for 1 min (power 9, 20 °C) using the VWR USC THD/HF Ultrasonic Cleaner (VWR International GmbH, Darmstadt, Germany). One day prior to recording the images, KB cells were seeded in eight well-chamber slides (Thermo Fisher Scientific, 20 000 cells in 300 µL medium per well) and cultured at 37 °C and 5% CO_2. On the day of the experiment, the medium was removed, replaced with 240 µL fresh medium and 60 µL NPs dispersed in HBG were added. After 2 h of incubation at 37 °C and 5% CO_2, each well was emptied by aspiration, supplemented with fresh medium, and incubated for another 2 h. The cells were then fixated with 4% paraformaldehyde in PBS (30 min incubation, room temperature). After fixating the cells, each well was washed once more with 400 µL PBS. Cell nuclei were then stained with DAPI (2 µg mL^{-1}) and F-Actin was labeled with phalloidin-rhodamine (1 µg mL^{-1}). After 30 min of incubation (room temperature, light protection), the staining mixture was removed and replaced with 300 µL PBS per well. Images were generated on a Leica-TCS-SP8 confocal laser scanning microscope equipped with an HC PL APO 63 × 1.4 objective. DAPI emission was recorded at 460 nm, calcein at 530 nm, rhodamine at 580 nm, and Alexafluor647 at 667 nm. All images were processed with the LAS X software from Leica.

2.2.29 MALDI mass spectrometry

For MALDI measurements, one µL of matrix solution composed of a saturated solution of Super-DHB (2-hydroxy-5-methoxybenzoic acid and 2,5-dihydroxybenzoic acid) in water/acetonitrile (1:1, v/v) containing 0.1 % (v/v) TFA was spotted on an MTP AnchorChip (Bruker Daltonics, Bremen, Germany). After crystallization of the Super-DHB matrix, one µL of sample solution to be analyzed, typically dissolved in water, was added on top of the crystallized matrix droplet and allowed to dry in a dust-protected environment. The samples were then analyzed utilizing an Autoflex II mass spectrometer (Bruker Daltonics, Bremen, Germany). Depending on the sample structure, data was recorded either in positive or negative mode. The actual measurement was carried out by Dr. Sören Reinhardt, LMU Munich, Germany.

2.2.30 Evaluation of toxicity by MTT-assay (adherent cell lines)

Experiments were conducted by Miriam Höhn, Department of Pharmacy, LMU Munich. A total of 5000 cells/well were seeded in 96-well plates (Corning® Costar, Sigma–Aldrich, Germany) 1 day prior to the experiment. The respective amount of formulation to be tested was prepared in HBG pH 7.4 at a five-fold concentration. For each well, 100 µL of treatment solution was prepared by mixing 20 µL formulation in HBG with 80 µL medium. 24 h after seeding the cells, the medium was aspirated and replaced with 100 µL treatment solution. For each formulation and concentration, an independent quintuplicate of five wells was treated. After addition of the treatment, the cells were incubated for the indicated duration at 37 °C and 5% CO_2. Afterwards, the wells were aspirated and replaced with fresh medium. 72 h after addition of the sample solutions, 10 µL 5 mg mL^{-1} MTT (3-(4,5-dimethylthiazol-2-yl)-2,5-diphenyltetrazolium bromide) resulting in a final concentration of 0.5 mg mL^{-1} was added to each well. The plates were then incubated for 2 h at 37 °C under mild shaking. Unreacted dye and medium were subsequently aspirated and the 96-well plates frozen at −80 °C for approximately 2 h. In order to fully dissolve the purple formazan product, 100 µL of DMSO were added to each well. The plates were then incubated under agitation for another 30 min. By measuring the absorbance at 590 nm taken together with a background correction at 630 nm using a microplate reader (TecanSpectrafluor Plus, Tecan, Switzerland), the absorption of each well was quantified. The relative cell viability (%) related to control wells treated with 20 µL HBG (pH 7.4) was then calculated as ([A] test/[A] control) × 100%.

2.2.31 Evaluation of toxicity by MTT-assay (suspension cell lines)

Experiments were conducted by Miriam Höhn, Department of Pharmacy, LMU Munich. L1210 cells were withdrawn from their culture flask, centrifuged (1500 rpm, 5 min), washed, resuspended in folate-free medium and cultured for 24 h at 37 °C and 5% CO_2. Afterward, the cell density was determined and adjusted to 125000 cells mL^{-1}. Treatment solutions in HBG buffer were prepared at fivefold their intended final concentration. A total of 480 µL cell suspension (125000 cells mL^{-1}) was then mixed with 120 µL respective treatment solution prepared at fivefold concentration. The obtained 600 µL cell suspension now containing the treatment at the final one-fold concentration was then transferred to five adjacent wells of a 96-well plate (100 µL corresponding to 10000 L1210 cells were added to each well). The cells were then cultured for the indicated duration, typically 72 h, at 37 °C and 5 % CO_2. For the 1 + 71 h incubation, cells were washed after 1 h by centrifuging (1500 rpm, 5 min) and replacing 50 µL of supernatant with fresh folate-free medium. This step was performed twice. After 72 h addition of the sample solutions, 100 µL of lysis buffer (10 mM HCl, 10% w/v sodiumdodecylsulfate) was added to each well. The plates were then incubated for 2 h (37 °C, 5% CO_2). Absorption values were then determined at 590 nm taken together with a background correction at 630 nm using a microplate reader (TecanSpectrafluor Plus, Tecan, Switzerland). The relative cell viability (%) related to control wells treated with 20 µL HBG (pH 7.4) was then calculated as ([A] test/[A] control) × 100%. The used washing protocol was developed by Dr. Ines Truebenbach, Department of Pharmacy, LMU Munich.

2.2.32 Calculation of EC_{50} values

EC_{50} values were determined using GraphPad PRISM version 6.01. To do so, respective dose-dependent viabilities determined in quintuplicate by MTT assay were plotted against their concentration (XY plot, 5 replicate values in side-by-side subcolumns). Then, X data (respective concentrations) was logarithmized. Respective EC_{50} values were then determined by nonlinear regression [curve fit, log(Inhibitor vs. response, variable slope, 4 parameters) fitting method least squares fit]. The best-fit EC_{50} values were reported in combination with the respective R^2 as an indication of fit quality.

2.2.33 Nanoparticle uptake experiments by flow cytometry

Experiments were conducted by Miriam Höhn, Department of Pharmacy, LMU Munich. One day before performing the experiment, KB cells were seeded in a 24-well plate. Each well contained 60 000 cells dispersed in 1 mL medium. On the next day, the medium was removed and replaced with 400 µL fresh medium. Next, 100 µL functionalized NPs in HBG were added to each well. After 1 h, the medium was removed by aspiration and each well was washed with 1 mL of PBS followed by trypsinization (5 min, 37 °C) with 200 µL of trypsin/EDTA. A total of 400 µL medium was added to each well and the cells were centrifuged (5 min, 1500 rpm, room temperature). In order to have enough cells for analysis, two independent wells per condition were pooled. The supernatant was removed and the cells were resuspended in 700 µL FACS buffer (10% FBS in PBS) and stored on ice. Directly prior to analysis, 2 µL DAPI (1 mg mL^{-1}) was added to each vial. Data were recorded utilizing the LSR Fortessa flow cytometer (BD Biosciences, Eysins, Switzerland). Gating and data analysis were performed with the FlowJo 7.6.5 flow cytometry analysis software. Initially, cells were gated by forward/sideward scatter and pulse width in order to exclude cell aggregates. Dead cells were subsequently excluded using DAPI and only isolated viable cells were evaluated. Approximately 10 000 gated cells per sample were collected. The threshold level for NP binding was determined based on the fluorescence of HBG-treated control wells.

2.2.34 Statistical analysis

If not stated otherwise, data are presented as mean ± standard deviation. Triplicates were analyzed for DLS measurements, ICP–AES, and PMX content by HPLC. For SEM, the as-obtained images were normalized to the scale bar and the size of 100 particles was subsequently analyzed. In flow cytometry experiments, a minimum of 10 000 gated cells were evaluated per condition. For the PMX content determination by HPLC, a PMX calibration curve (six data points between 0 nmol and 5 nmol) was recorded (R^2 = 0.9976). MTT experiments were performed in quintuplicates and the data were analyzed by two-way ANOVA utilizing GraphPad Prism version 6.01. Testing was performed with α = 0.05 and n = 5. After performing the analysis, stars were assigned according to the p-values: *for $p \leq 0.05$, **for $p \leq 0.01$, *** for $p \leq 0.001$, and **** for $p \leq 0.0001$.

3 Results

3.1 Delivery of chemotherapeutics by metal-organic frameworks

3.1.1 Screening of a peptide tag library designed for metal-organic framework cargo attachment

Background. *This chapter describes the screening of a peptide tag library in order to identify short peptide sequences that are able to mediate MOF cargo attachment. To obtain a deeper understanding of the binding process, the synthesized library incorporated different tag lengths and was evaluated on multiple selected MOFs with different properties.*

The ability to understand and control MOF surface chemistry is of paramount importance in a biomedical setting as it allows to modify and tune MOF characteristics such as colloidal stability,[153] on-demand cargo release,[154] co-delivery of multiple cargos,[96] enhanced endosomal escape[155] and immune recognition.[155]

Nevertheless, compared to bulk functionalization approaches, research aimed selectively at outer surface modification of MOF NPs has received less attention.[156] So far, examples of reported covalent outer surface modification strategies include introduction of orthogonal functional groups by post-synthetic linker exchange,[95] polymer attachment by radical polymerization[157] or EDC/NHS chemistry,[158] coating with coil-forming peptides to allow for on-demand superstructure assembly[159] and core-shell structures realized by silica coating[160] or silica matrix inclusion.[161]

However, the harsh reaction conditions typically required impair the biomedical applicability with regard to labile cargos and recent reports of milder, non-covalent modification strategies such as polymer coatings,[162] liposome fusion,[163] exosome coating[155] and cargo attachment by short[96] or long[164] peptide sequences may point towards more compatible alternatives.

For the last mentioned approach, the relevant publication determined binding sequences by phage display which has the advantage of identifying high-affinity binding peptides, but provides little information about the structure-activity relationships governing the binding process.

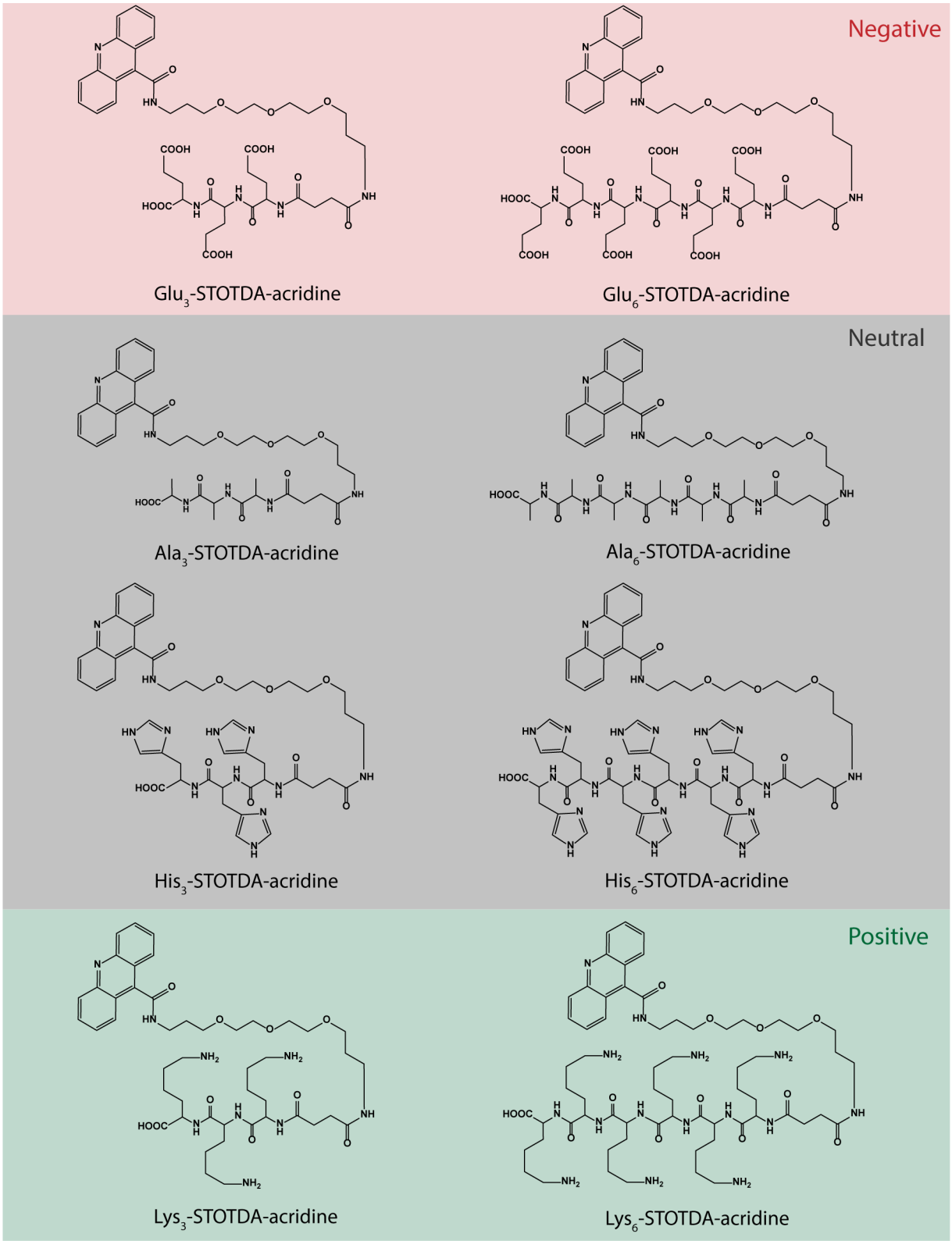

Figure 2 Overview of the synthesized peptide tags grouped by net charge at neutral pH. Each tag is composed of an acridine moiety to allow for photometric detection, a short PEG spacing unit (STOTDA) and the respective amino acids denoted in one letter code. The left column shows screened tripeptide tags whereas the respective hexapeptide analogues are depicted on the right. From top to bottom: glutamate-, alanine-, histidine- and lysine tags.

Therefore, in order to shed light on how peptide properties influence binding characteristics, a peptide tag library consisting of 8 structures (**Figure 2**) was designed and screened on a panel of MOFs.

Each peptide tag incorporates an aromatic acridine moiety to allow for selective photometric detection at a wavelength free of interference by MOF components, a short polyethyleneglycol-based spacing unit (STOTDA) and the actual peptidic binding sequence. Here, used amino acids were chosen based on their charge at neutral pH and included glutamate (negative), alanine (neutral), histidine (neutral to slightly charged) and lysine (positive).

Of each tag, both tripeptide- and hexapeptide versions were generated and evaluated in order to try to understand the influence of tag length and charge density on the overall binding capacities.

Investigated MOFs were chosen based on two main reasons: biomedical relevance and structural diversity. Zr-*fum*,[165] UiO-66,[166] MIL-88A,[80] MIL-100(Fe)[47d, 80] all fit the former requirement as illustrated by the selected studies and are also generally regarded as promising in a biomedical setting.

In contrast, HKUST-1 and MIL-101(Cr) seem initially limited by toxicity concerns due to the incorporated copper or chromium. Nevertheless, both MOFs were included based on their material properties, HKUST-1 due to its potential for certain biosensory applications,[167] MIL-101(Cr) due to the presence of coordinatively unsaturated open metal sites on the particle surface and its high porosity with pores reaching sizes of 29 Å and 34 Å.[146]

In order to detect possible saturation processes, the actual screening was performed by varying the amount of MOF while keeping the amount of offered peptide tag constant at 130 nmol.

Screening of Zr-fum

Evaluating the microporous (5 – 7 Å) Zr-*fum*[65] with regard to its binding capacity for peptide tags (**Figure 3**) identified the Glu_3 tag as most promising. 500 µg of Zr-*fum* were able to bind approximately 31,6 ± 4,9 nmol of Glu_3 which decreased to 14,7 ± 1,2 nmol for the Glu_6. Histidine was the second most prominent binder with obtained values of 6,9 ± 1,3 nmol (His_3) and 12,4 ± 1,8 nmol (His_6) per 500 µg of MOF.

The bindings were also evaluated by plotting the photometrically determined average amount of bound peptide tag against the amount of MOF used to obtain the respective binding value (**Figure 4**). This was done in order to investigate if the offered amount of MOF and the respective amount of tag bound by it follow a linear relationship. Additionally, such a plot may hint at saturation processes.

Here, linear relationships were only observed for Glu_3, Glu_6, His_3 and His_6. Here, respective R^2 values of 0.9992, 0.9547, 0.9754 and 0.7944 were calculated and confirm the linearity between the amount of bound peptide and the amount of offered MOF. As no dose-dependent increase in binding capacity, and thus no linear relationship, was observed for Ala_3, Ala_6, Lys_3 and Lys_6, it may be assumed that those tags either do not bind to Zr-*fum*. The binding capacity might also be so low that even scaling the amount of offered Zr-*fum* by a factor of 20 (25 µg vs. 500 µg) only has a very minor effect on the overall amount of bound peptide.

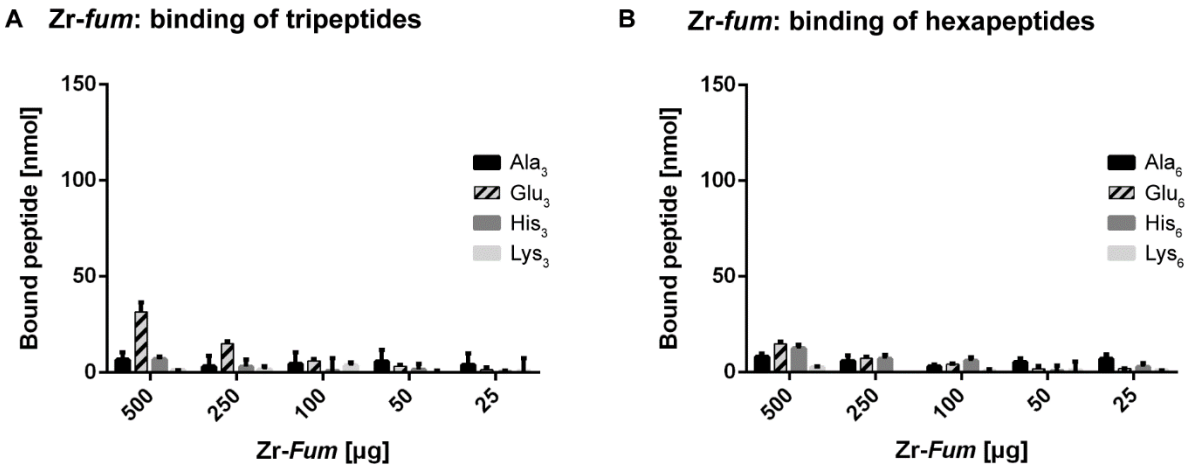

Figure 3 Tag screening for *Zr-fum.* **A**) binding of tripeptides, **B**) binding of hexapeptides. 130 nmol of the respective tag were added to various amounts of Zr-*fum*, composed of fumaric acid and Zr^{4+}, and incubated for 15 minutes. After incubation, samples were centrifuged and the amount of bound tag determined by photometric differential quantification.

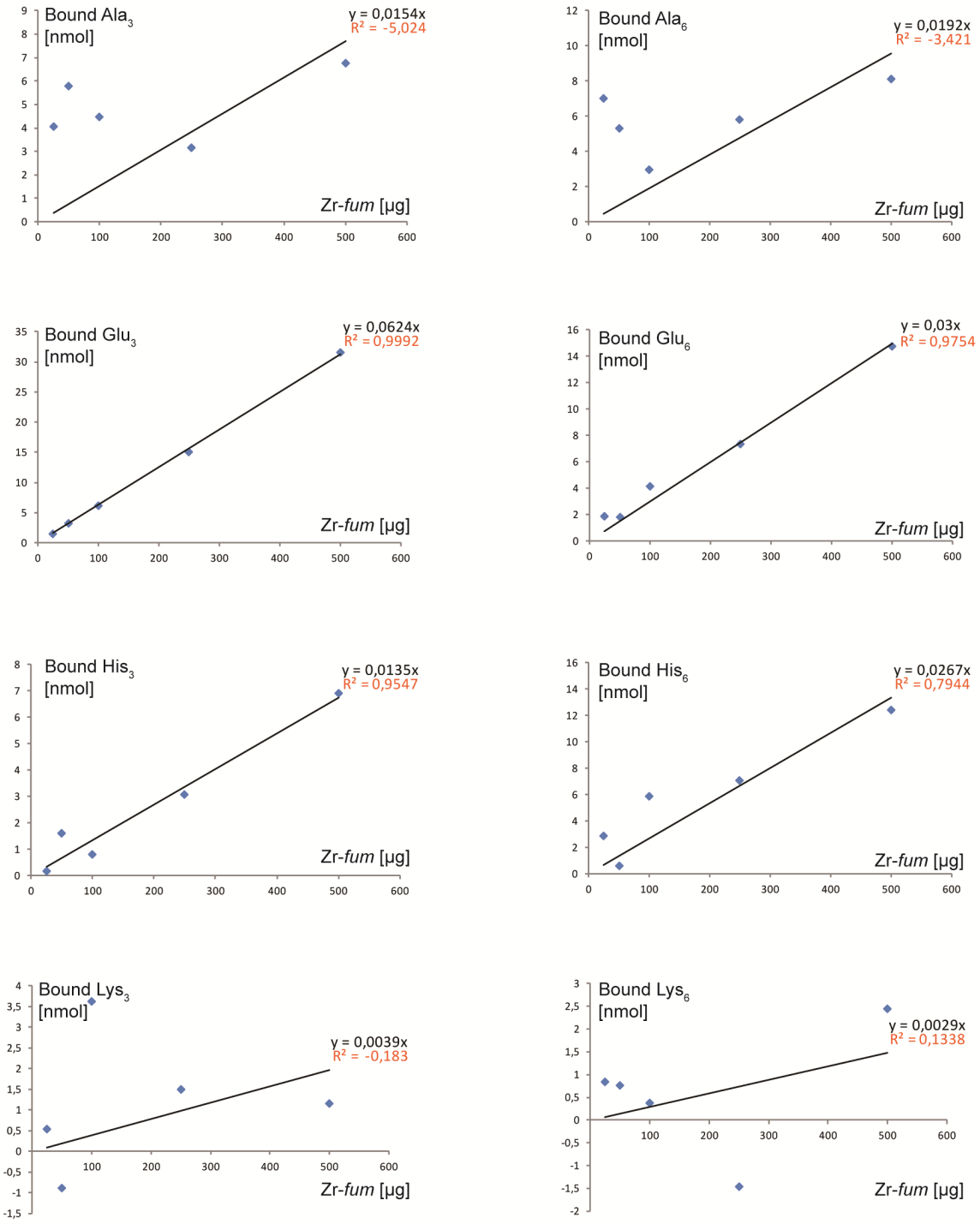

Figure 4 Evaluation of linearity between the amount of offered Zr-*fum* in micrograms (X axis) and average bound respective peptide tag in nmol (Y axis). The left column represents tripeptide tags whereas the hexapeptide tags are denoted in the right column. Rows from top to bottom: Ala-, Glu-, His- and Lys-tags. For the Glu_3, Glu_6, His_3 and His_6 tags, the amount of bound peptide increases linearly with the amount of offered MOF as reflected by the R^2 values.

Screening of UiO-66

For UiO-66, His_3 was identified as the best binding motif (**Figure 5**). Here, a binding of 115,9 ± 2,6 nmol per 500 µg UiO-66 was observed. Lys_3 showed the second highest binding with a value of 76.5 ± 2.1 nmol per 500 µg UiO-66. Here, the tag length had a decisive influence on the binding capacity, increasing the number of amino acids within the tag to six repetitions reduced the overall bindings to 47.7 ± 2.1 nmol (His_6) and 24.5 ± 4.3 nmol (Lys_6). No major difference in binding was observed between Ala_3 and Glu_3 hinting at electrostatic interactions not being a major force. Ala binding might be a consequence of π-stacking between the aromatic moieties of acridine and the H_2BDC linker. For hexapeptide tags, additional negative charge impaired the binding process – which was expected due to the slightly negative zeta potential of UiO-66[168] – and, compared to Glu_3, the overall peptide binding was reduced for Glu_6. In contrast, extending the Ala tag to six repetitions had no effect on overall binding. Linearity between the amount of offered MOF and amount of bound peptide was observed for all tags (**Figure 6**) suggesting that all tags do indeed interact with UiO-66. Observed R^2 values varied between 0.7094 (Lys_6) and 0.9982 (Lys_3). With the exception of Ala_6, better linearities were observed for the tripeptide tags. Interestingly, compared to His_3, the observed binding capacity approximately halved for His_6 which might be due to the increased number of coordinatively active imidazole functions. If one tag molecule has a twofold number of coordinative groups, it might interact with twice as many coordinatively unsaturated metal sites (CUS) on the MOF surface. As CUS are limited in number, the result might be the lower binding observed for the His_6-tag.

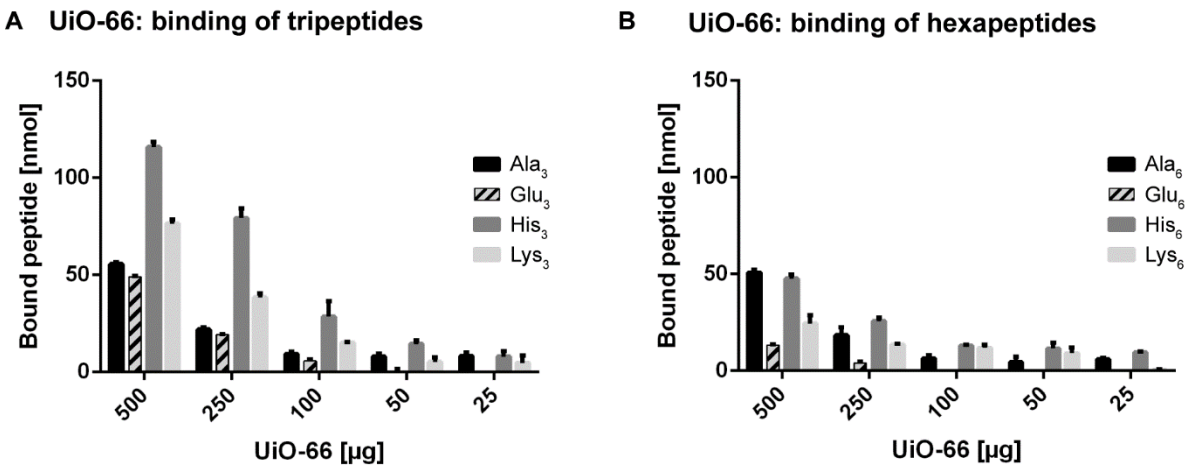

Figure 5 Tag screening for UiO-66. **A**) binding of tripeptides, **B**) binding of hexapeptides. 130 nmol of the respective tag were added to various amounts of UiO-66, composed of H_2BDC and Zr^{4+}, and incubated for 15 minutes. After incubation, samples were centrifuged and the amount of bound tag determined by photometric differential quantification. H_2BDC, benzenedicarboxylic acid.

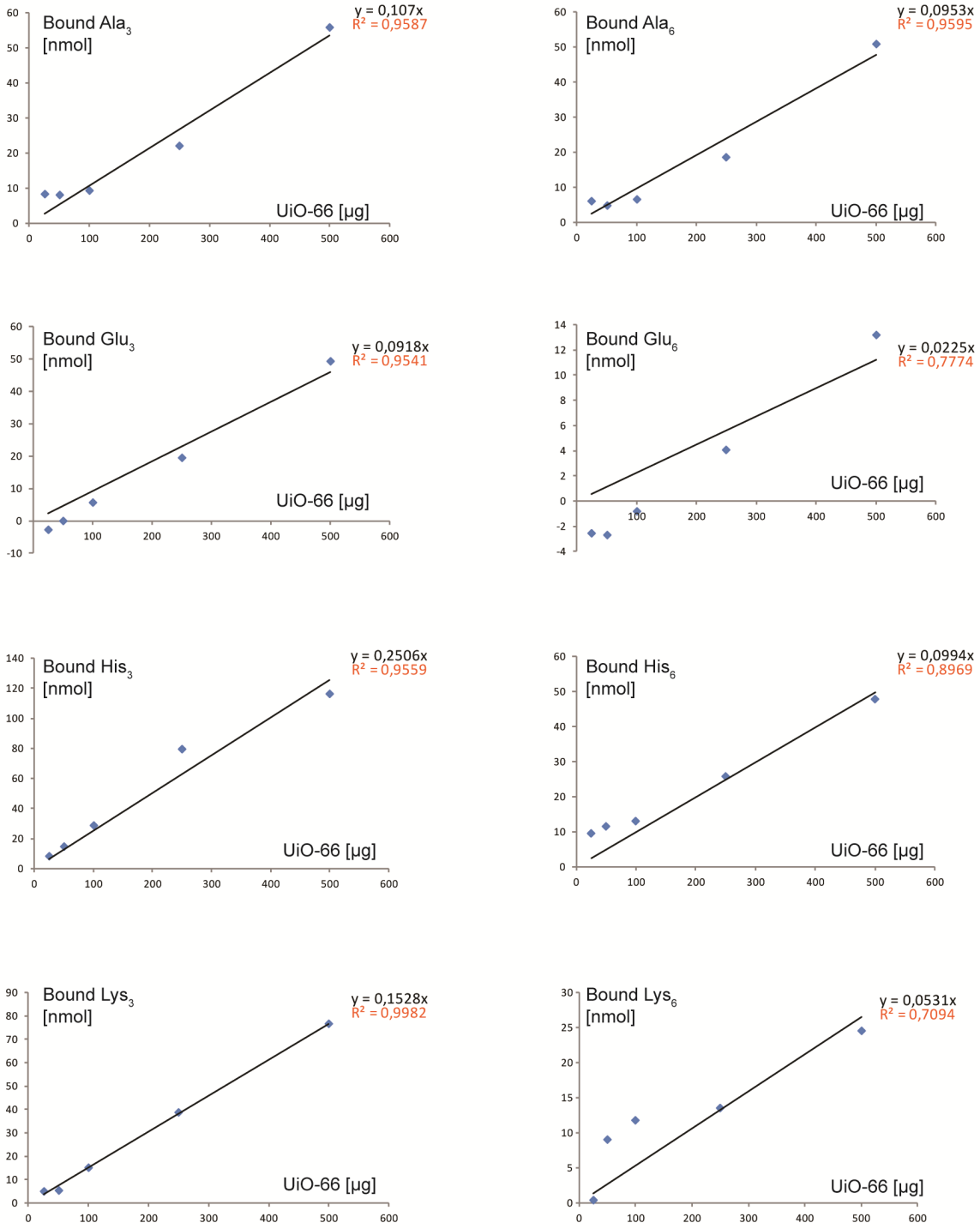

Figure 6 Evaluation of linearity between amount of offered UiO-66 in micrograms (X achsis) and average bound respective peptide tag in nmol (Y achsis). The left column represents tripeptide tags whereas the hexapeptide tags are denoted in the right column. Rows from top to bottom: Ala-, Glu-, His- and Lys-tags. For all evaluated peptides, the amount of bound peptide increases linearly with the amount of offered MOF as reflected by R^2 values. The best fit was observed for Lys_3.

Screening of MIL-88A

Tag binding evaluation for the iron fumarate MOF MIL-88A (**Figure 7**) which features a low porosity and some flexibility [61] identified Glu_3 as the most prominent binder. Here, a binding of 128.4 ± 0.25 nmol per 500 µg was observed. The second highest overall binding was observed for His_3 with a binding of 40.3 ± 5.4 nmol per 500 µg MIL-88A. Low binding values of 5.7 ± 4.3 nmol and 0.8 ± 0.4 nmol were determined for Ala_3 and Lys_3. This hints at the positive charge of Lys_3 neither impairing, nor promoting tag attachment as the overall binding was similarly low to that observed for neutral Ala_3.

Looking at the hexahistidine tags reveals that increasing the tag length from Glu_3 to Glu_6 reduces the overall binding to 98.5 ± 10.2 nmol. In contrast, by elongating His_3 to His_6, binding notably increases to 95.8 ±1.2 nmol. With regard to Lys_6 and Ala_6, no obvious difference in binding capacities was observed by comparing the hexapeptide tags to the respective tripeptide tags.

Figure 8 illustrates the linearity between the offered amount of MIL-88A in micrograms and the respective bound amount of peptide tag in nmol. Here, Glu_3, Glu_6, His_3 and His_6 displayed R^2 values higher than 0.95 showing a linear relationship. Notably, no such linear correlation was observed for Ala_3, Ala_6, Lys_3 and Lys_6. It was therefore concluded that the Ala_3, Ala_6, Lys_3 an Lys_6 tags only interact with MIL-88A to an insignificant degree too low for sensible quantification using a photometric setup.

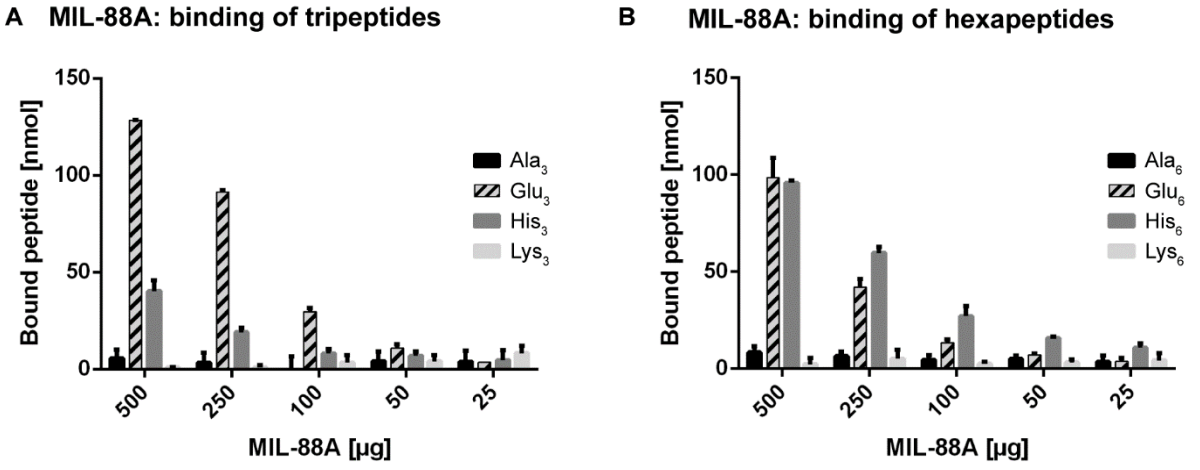

Figure 7 Tag screening for MIL-88A. **A**) binding of tripeptides, **B**) binding of hexapeptides. 130 nmol of the respective tag were added to various amounts of MIL-88A, composed of fumaric acid and Fe^{3+}, and incubated for 15 minutes. After incubation, samples were centrifuged and the amount of bound tag determined by photometric differential quantification.

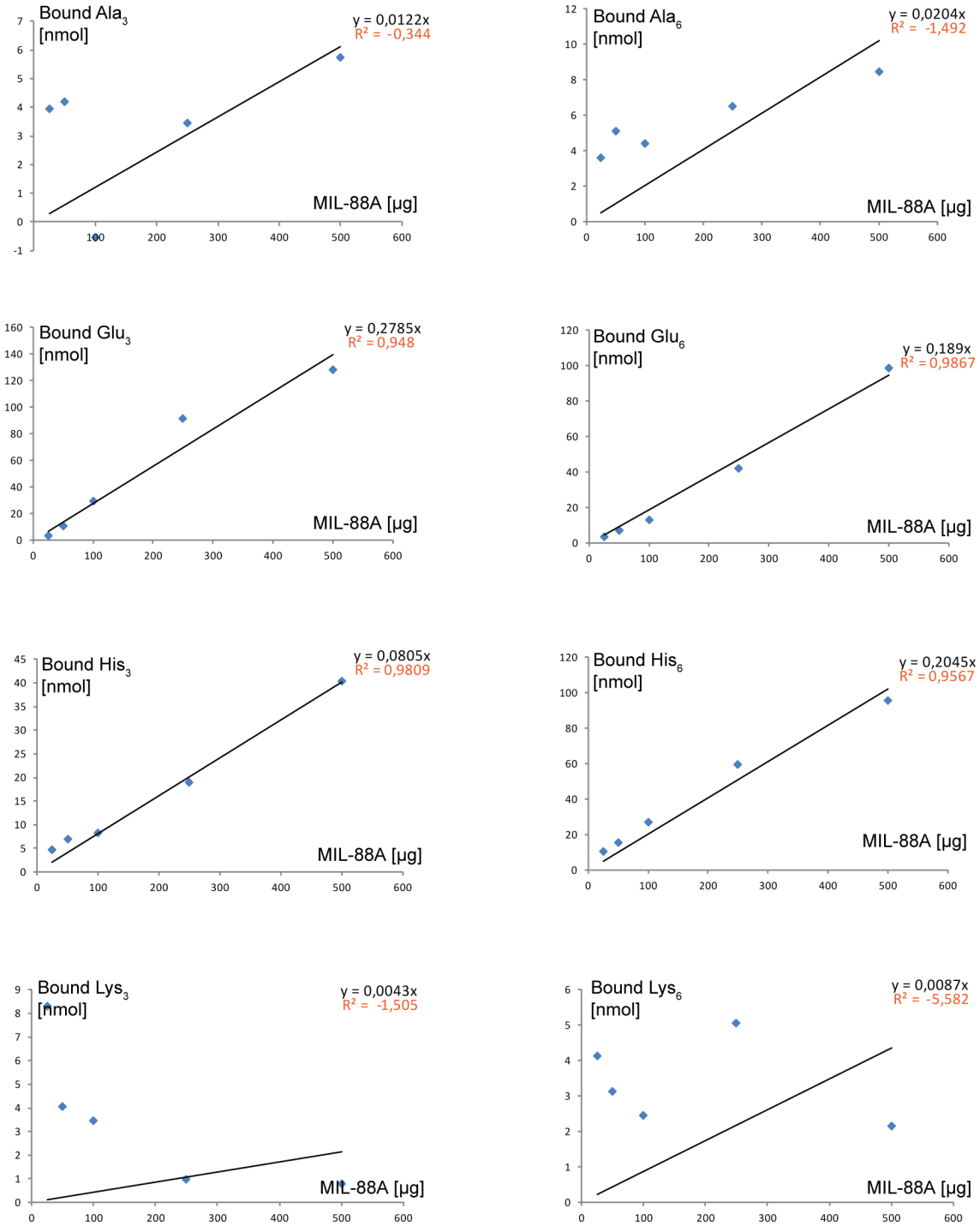

Figure 8 Evaluation of linearity between amount of offered MIL-88A in micrograms (X axis) and average bound respective peptide tag in nmol (Y axis). The left column represents tripeptide tags whereas the hexapeptide tags are denoted in the right column. Rows from top to bottom: Ala-, Glu-, His- and Lys-tags. For Glu_3, Glu_6, His_3 and His_6, meaningful tag bindings and linear relationships resulting in R^2 values above 0.95 were observed.

Screening of MIL-100(Fe)

For the highly porous MIL-100(Fe),[62] similarly high tag bindings were observed for His_3 (122.9 ± 8.8 nmol per 500 µg MOF) and Lys_3 (119.5 ± 6.5 nmol per 500 µg MOF). Strikingly, also Glu_3 (100.5 ± 1.7 nmol per 500 µg MOF) and Ala_3 (110 ± 0.1 nmol per 500 µg MOF) tags resulted in very high bindings. Looking at the hexapeptides, for all tags except Ala_6 which remained unchanged at 110.3 ± 0.6 nmol per 500 µg MOF, a reduction in binding capacity was determined. For His_6, overall binding decreased to 114.5 ± 0.1 nmol per 500 µg MOF whereas for Glu_6, a pronounced reduction to 15.8 ± 6.5 nmol per 500 µg MOF was observed. Compared to Lys_3, tag elongation to Lys_6 resulted in a slightly reduced binding value of 103 ± 4 nmol per 500 µg MOF. Evaluating the linearity (**Figure 10**) found linear relationships for all screened tags and resulted in R^2 values in a range between 0.6545 (Ala_3) and 0.9985 (His_6). At the neutral assay pH, MIL-100 (Fe) displays a negative zeta potential of approximately – 20 mV[169] which may account for the high bindings observed for positively charged Lys_n tags due to electrostatic attraction. The Glu_n tags however seem to experience electrostatic repulsion indicated by the strongly reduced binding observed for Glu_6 which has a higher negative charge density than Glu_3. Additionally, Glu_3 showed a slightly reduced binding compared to the neutral Ala_3. Observed good His_n tag bindings are likely attributable to a combination of pore diffusion and the presence of coordinatively unsaturated metal sites (CUS) on the MOF surface[170] whereas binding of the Ala tags might be related to passive pore diffusion .

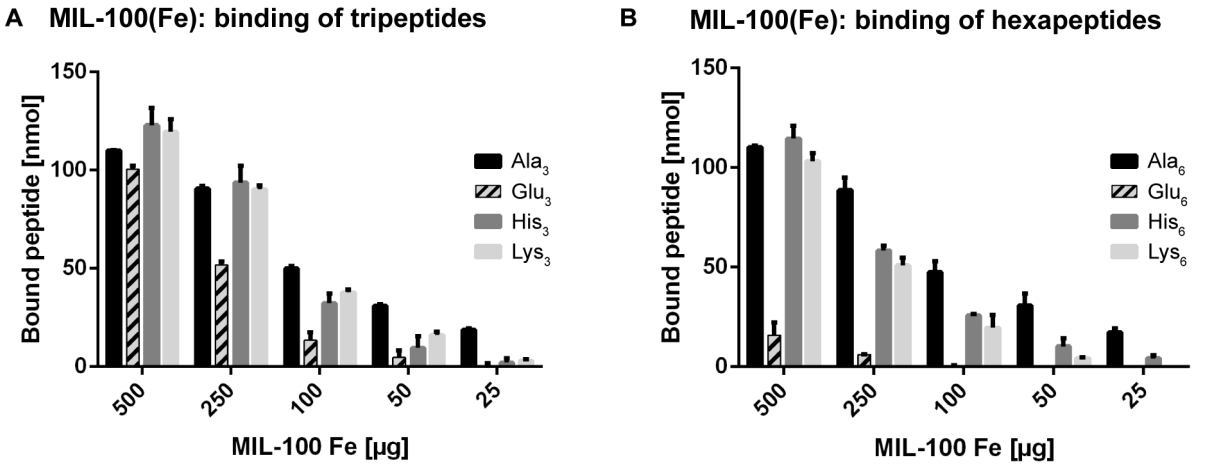

Figure 9 Tag screening for MIL-100(Fe). **A**) binding of tripeptides, **B**) binding of hexapeptides. 130 nmol of the respective tag were added to various amounts of MIL-100(Fe), composed of H_3BTC and Fe^{3+}, and incubated for 15 minutes. After incubation, samples were centrifuged and the amount of bound tag determined by photometric differential quantification. H_3BTC, benzenetricarboxylic acid.

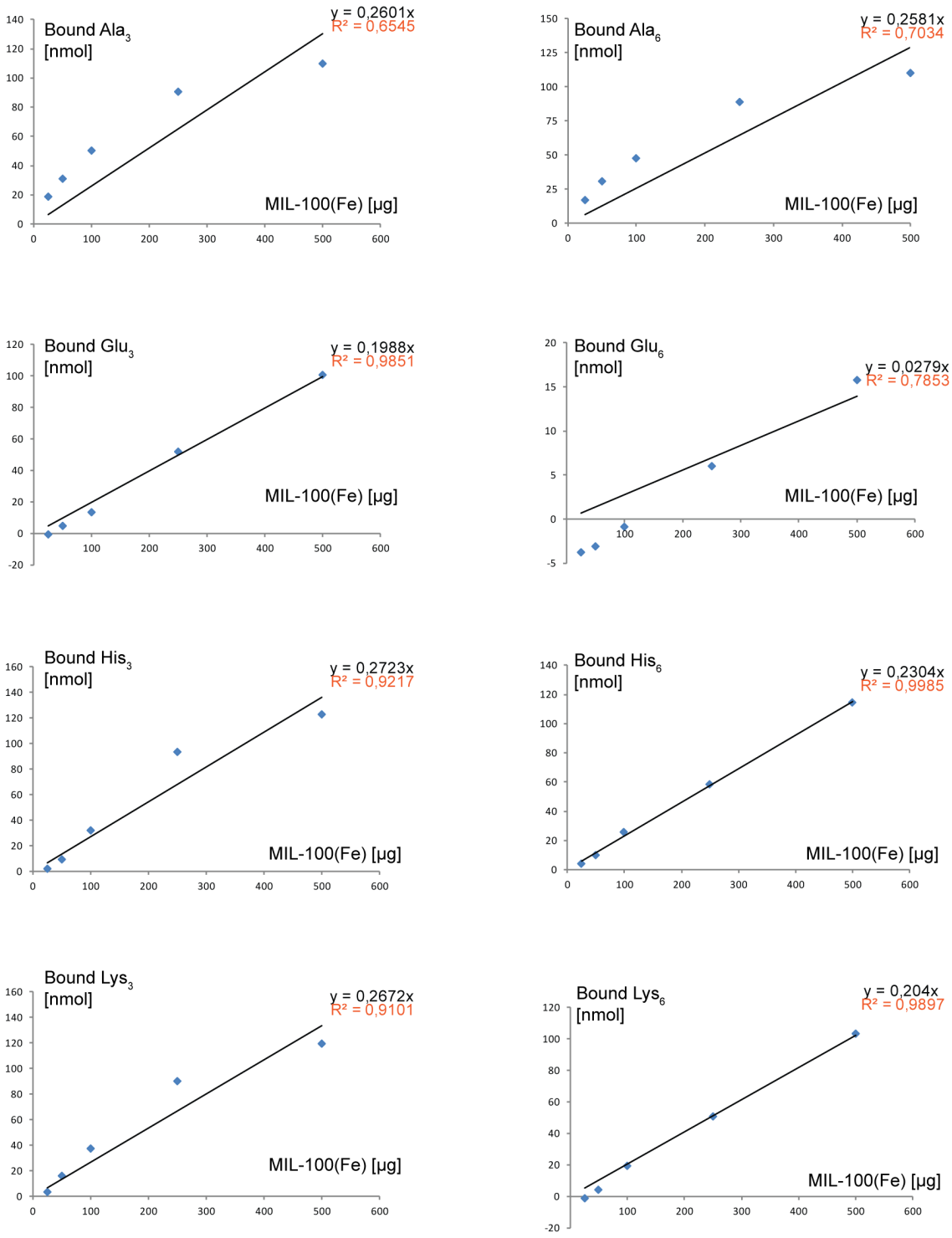

Figure 10 Evaluation of linearity between amount of offered MIL-100 (Fe) in micrograms (X axis) and average bound respective peptide tag in nmol (Y axis). The left column represents tripeptide tags whereas the hexapeptide tags are denoted in the right column. Rows from top to bottom: Ala-, Glu-, His- and Lys-tags. For all screened tags, the amount of bound tag correlates to a varying extent with the amount of used MIL-100(Fe) and R^2 values between 0.6545 (Ala_3) and 0.9985 (His_6) were observed.

Screening of MIL-101 (Cr)

The highly porous MIL-101(Cr)[146] displayed the highest overall tag bindings. For the tripeptides, with the exception of Lys_3 that showed a rather low binding of 12.6 ± 1.3 nmol per 500 µg MOF, tag binding capacities of 500 µg MOF exceeded the respective 130 nmol offered tag. For the hexapeptides, the same holds true for Ala_6 and His_6. For the remaining hexapeptide tags, extending the tag length resulted in lower binding values. For Glu_6, binding decreased to 83.4 ± 3.6 nmol per 500 µg whereas a reduction to 7.2 ± 0.2 nmol per 500 µg MOF was determined for Lys_6. Looking at the linearity plot (**Figure 12**) confirms those observations. Here, for Ala_3, Ala_6, His_3 and His_6, saturation can be observed as further elevating the amount of MOF beyond 250 µg does not increase the amount of bound tag accordingly since all offered tag molecules are already bound by 250 µg MOF which is also reflected by the lowered R^2 values. In contrast, good linearity was observed for Glu_3 (0.9617) and Glu_6 (0.9778) further indicating that the binding capacity of 500 µg MOF for those peptides lies below, or - in case of Glu_3 - close to the offered 130 nmol tag. The low R^2 values calculated for Lys_3 (0.4983) and Lys_6 (0.3915) hint at a minor influence of the tag length and only weak interactions between the Lys tags and the MOF. At assay pH, MIL-101(Cr) displays a positive zeta potential of approximately +45 mV[171] which likely accounts for the weak positively charged Lys_n and strong negatively charged Glu_n tag bindings due to electrostatic interactions. The strong Ala_n bindings may be attributed to the pronounced porosity of MIL-101(Cr) allowing for passive pore diffusion.

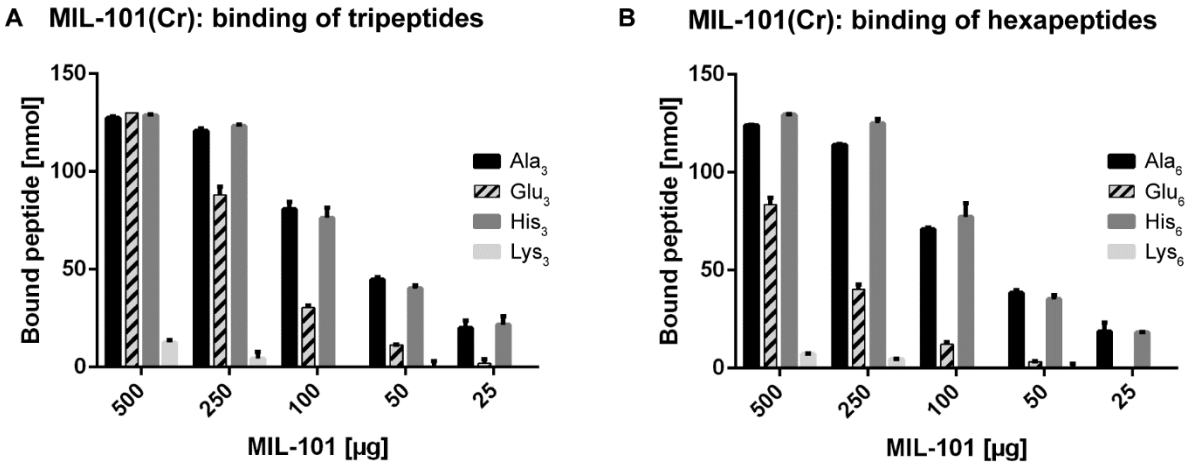

Figure 11 Tag screening for MIL-101(Cr). **A**) binding of tripeptides, **B**) binding of hexapeptides. 130 nmol of the respective tag were added to various amounts of MIL-101(Cr), composed of H_2BDC and Cr^{3+}, and incubated for 15 minutes. After incubation, samples were centrifuged and the amount of bound tag determined by photometric differential quantification. H_2BDC, benzenedicarboxylic acid.

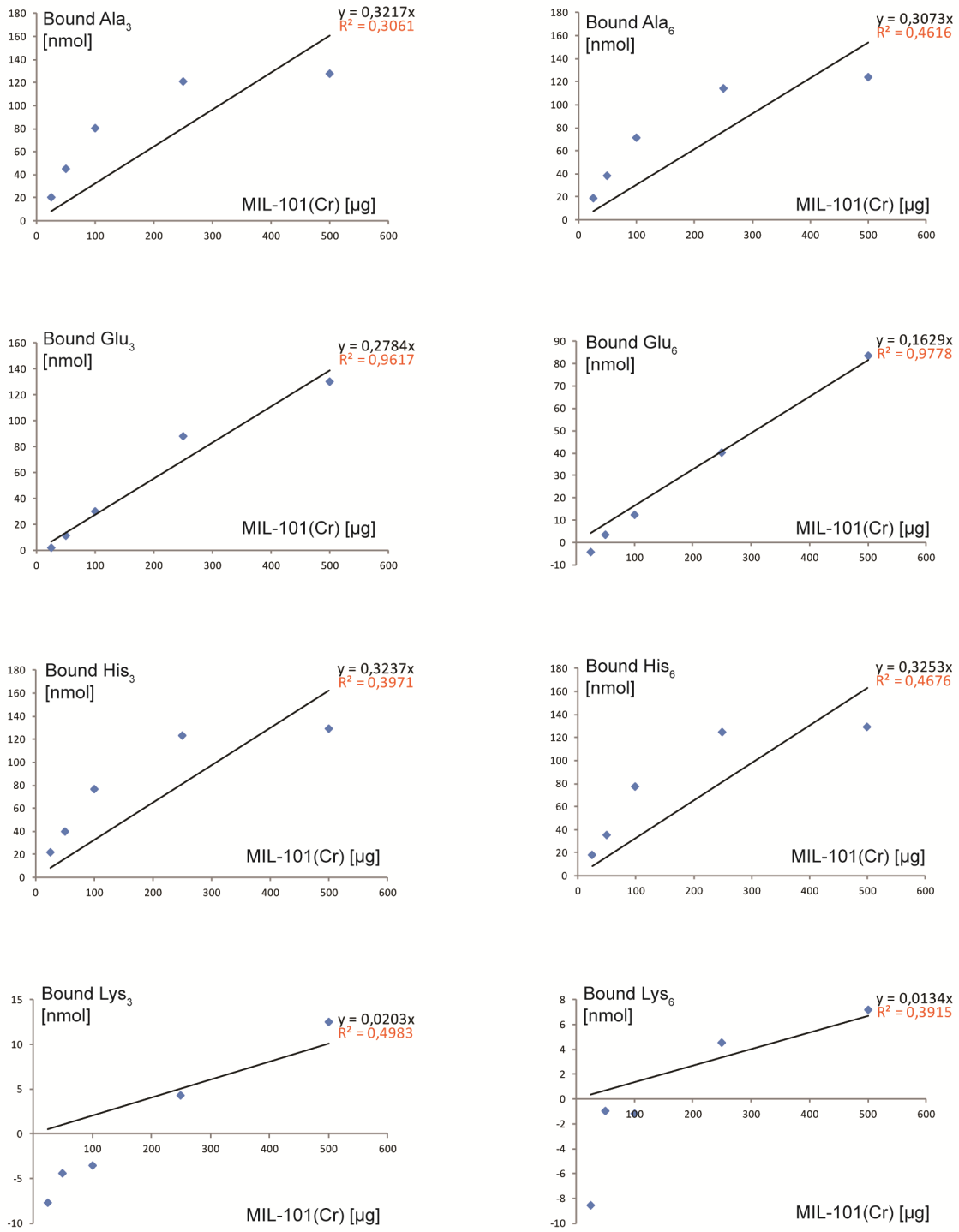

Figure 12 Evaluation of linearity between amount of offered MIL-101(Cr) in micrograms (X axis) and average bound respective peptide tag in nmol (Y axis). The left column represents tripeptide tags whereas the hexapeptide tags are denoted in the right column. Rows from top to bottom: Ala-, Glu-, His- and Lys-tags. For all tags, a linear relationship was observed. For Ala_3, Ala_6, His_3, His_6, R^2 values are reduced as a consequence of the offered respective amount of peptide tag being already fully bound by 250 µg MOF.

Screening of HKUST-1

For the microporous HKUST-1,[148] the highest binding was witnessed for His_6. Here, 500 µg of MOF bound 103.8 ± 12.5 nmol. Lys_6 was the second most prominent binder with a value of 39.6 ± 1.8 nmol per 500 µg MOF. Among the tripeptides, His_3 showed the highest binding (19.2 ± 5 nmol per 500 µg MOF), in contrast, comparably low bindings were observed for Ala_3 and Lys_3 (11.9 ± 2.8 nmol and 12.9 ± 0.8 nmol per 500 µg MOF) hinting at little to no influence of the positive charge of Lys_3. Looking at the hexapeptides, Lys_6 displayed a higher binding compared to Lys_3 and the amount of bound tag increased to 39.6 ± 1.8 nmol per 500 µg MOF. The negative zeta potential of approximately -12 mV reported for HKUST-1[172] explains the better binding observed for Lys_6 which incorporates a higher positive charge density compared to Lys_3 and is thus likely subjected to stronger electrostatic attraction whereas the lack of binding observed for negatively charged Glu_n tags may be attributed to electrostatic repulsion. An explanation for the pronounced His_6 binding capacity lies within the HKUST-1 metal component copper being able to undergo strong interactions with the hexahistidine tag,[173] a known mechanism also applied routinely for certain versions of immobilized metal affinity chromatography (IMAC). The linearity plot (**Figure 14**) only shows linear relationships between the amount of offered HKUST-1 and the respective amount of tag bound by it for His_6, Lys_3 and Lys_6 with values of R^2 = 0.9561, 0.9537 and 0.9853, respectively. As no linearities were observed for Ala_3, Ala_6, His_3, Glu_3 and Glu_6, it may be concluded that those tags only bind to HKUST-1 to a very minor extent.

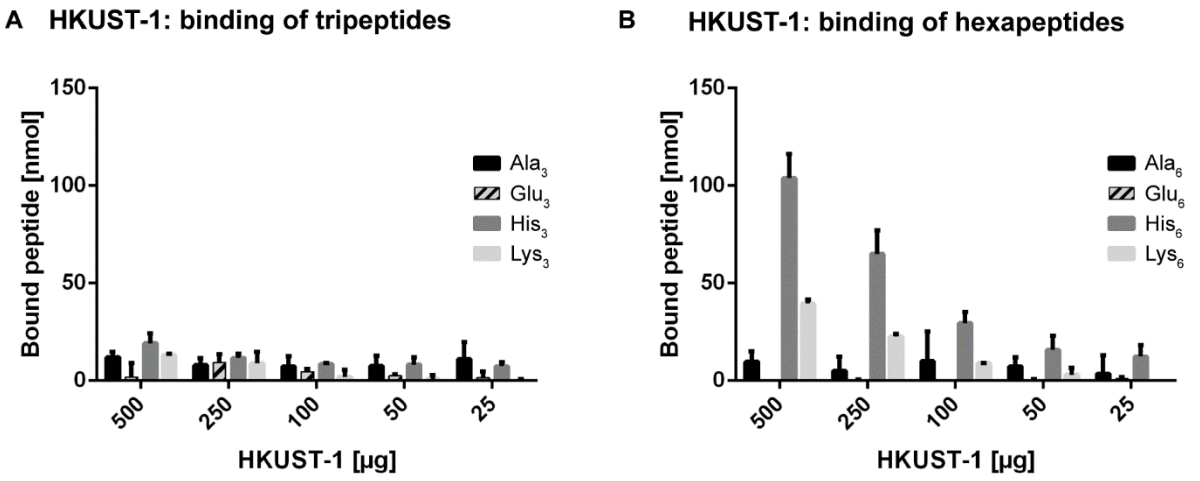

Figure 13 Tag screening for HKUST-1. **A**) binding of tripeptides, **B**) binding of hexapeptides. 130 nmol of the respective tag were added to various amounts of HKUST-1, composed of H_3BTC and Cu^{2+}, and incubated for 15 minutes. After incubation, samples were centrifuged and the amount of bound tag determined by photometric differential quantification. H_3BTC, benzenetricarboxylic acid.

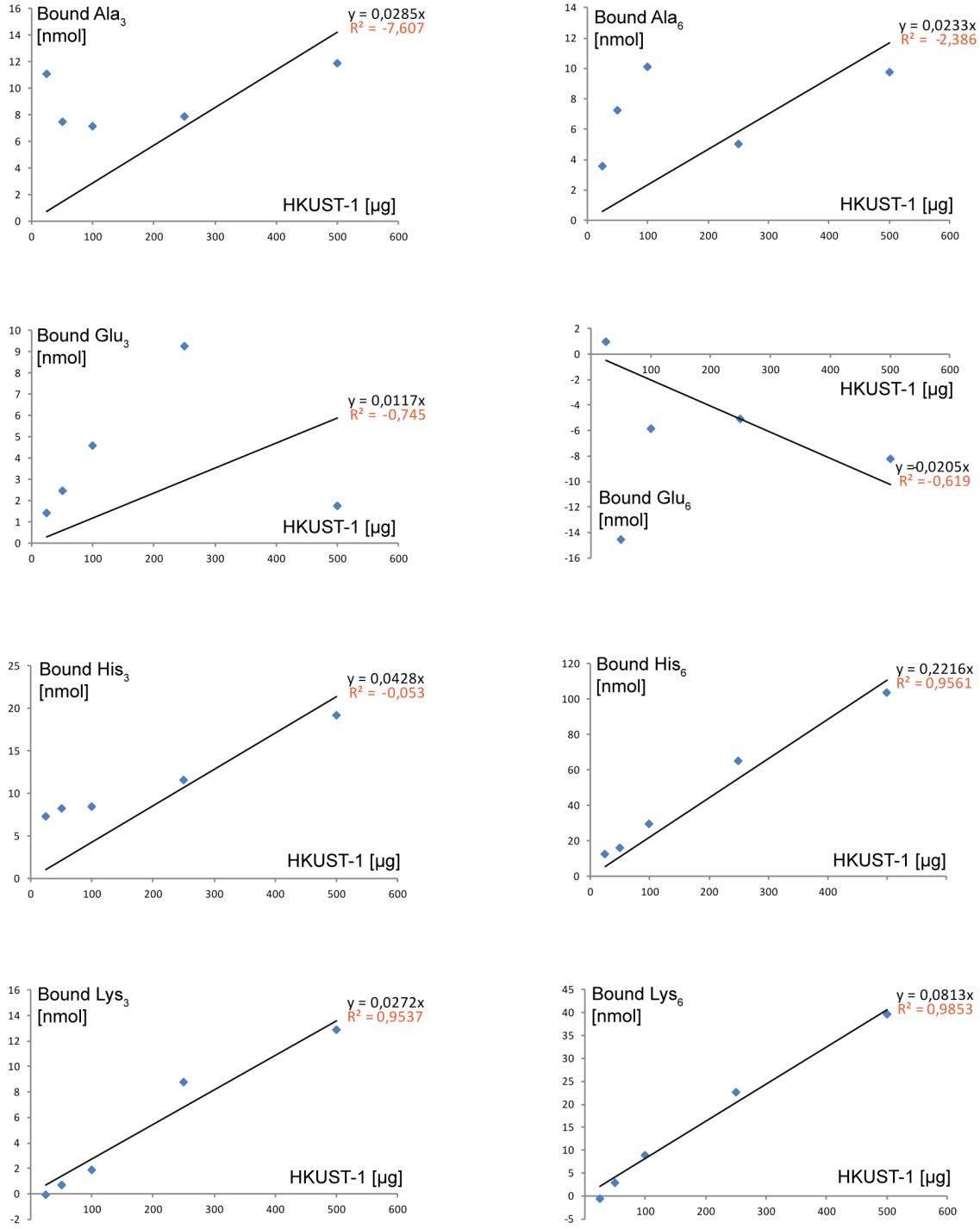

Figure 14 Evaluation of linearity between amount of offered HKUST-1 in micrograms (X axis) and average bound respective peptide tag in nmol (Y axis). The left column represents tripeptide tags whereas the hexapeptide tags are denoted in the right column. Rows from top to bottom: Ala-, Glu-, His- and Lys-tags.

3.1.2 Delivery of polyglutamylated methotrexate derivatives by attachment to selected metal-organic frameworks

***Background**. In the previous chapter, Glu_3 and Glu_6, also referred to as E_3 and E_6 in amino acid one letter code, were among the structures identified as potentially suitable MOF anchoring motifs. This chapter proceeds to explore their utilization for a chemotherapeutic drug delivery application. Here, modification with the identified E_n motifs was utilized to create and deliver polyglutamylated MTX derivatives by attachment to MOF NPs. Due to their biocompatibility, Zr-fum and MIL-88A were chosen as potentially suitable MOFs. After physicochemical characterization, the potential of the E_n-MTX delivery system was then evaluated in vitro utilizing rather resistant adherent KB (cervix carcinoma) and sensitive suspension L1210 (mouse lymphocytic leukemia) cell lines.*

As outlined in the introduction, cytosolic polyglutamylation of selected antifolate chemotherapeutics affects their pharmacological activities as it enhances target enzyme affinities[128] and allows for cytosolic drug accumulation by reducing immediate drug efflux.

Therefore, nanoparticular delivery of pre-polyglutamylated MTX is an interesting avenue to explore as it may circumvent one of the known antifolate resistance mechanisms based on impaired polyglutamylation. Additionally, it opens the door towards cellular uptake mechanisms such as endocytosis[174] which are not feasible for small molecule drugs.

Among other motifs, the previous chapter identified glutamate tri- and hexapeptides as structures conferring pronounced MOF binding capacities to a desired cargo. Therefore, polyglutamylated MTX derivatives, namely E_2-MTX and E_5-MTX, corresponding to the binding substructure of the E_3 and E_6 tag since one glutamate is already part of the MTX structure, were synthesized and subsequently delivered by MOF. Initially, E_2-Folate (E_2-FolA) and E_5-Folate (E_5-FolA) were also included as control structures.

Zr-*fum* and MIL-88A were chosen as the MOF component due to their biocompatibilities[79-80, 165] and the suitable E_n-tag binding capacities observed in the previous chapter.

In a first step, overall binding capacities for E_n-MTX and respective E_n-FolA controls were determined (**Figure 15**) by applying the photometric assay already established for the tag screening presented in chapter **3.1.1**.

For Zr-*fum*, respective tripeptide binding values (Figure 15A) per 500 µg MOF of 31.11 ± 2.92 nmol (E_2-MTX) and 44.65 ± 1.04 nmol (E_2-FolA) were observed and agree well with the previously determined E_3-tag binding of 31,6 ± 4,9 nmol per 500 µg MOF.

For MIL-88A, tripeptide binding capacities (Figure 15B) of 111.05 ± 1.80 nmol (E_2-MTX) and 94.96 ± 1.70 nmol (E_2-FolA) per 500 µg MOF were recorded. Previously, a slightly higher E_3 acridine tag binding of 128.4 ± 0.25 nmol per 500 µg MOF was determined.

Screening the hexapeptides on Zr-*fum* (Figure 15C) revealed binding capacities of 16.6 ± 0.71 nmol (E_5-MTX) and 10.57 ± 4.03 nmol (E_5-FolA) per 500 µg MOF. During the tag screening, an E_6-tag binding of 14,7 ± 1,2 nmol per 500 µg MOF was observed.

For MIL-88A, examination of the hexapeptide bindings (Figure 15D) revealed binding values of 76.7 ± 4.07 nmol (E_5-MTX) and 68.68 ± 1.54 nmol (E_5-FolA) per 500 µg MOF which is below the binding capacity of 98.5 ± 10.2 nmol E_6-tag per 500 µg MOF determined during the tag screening.

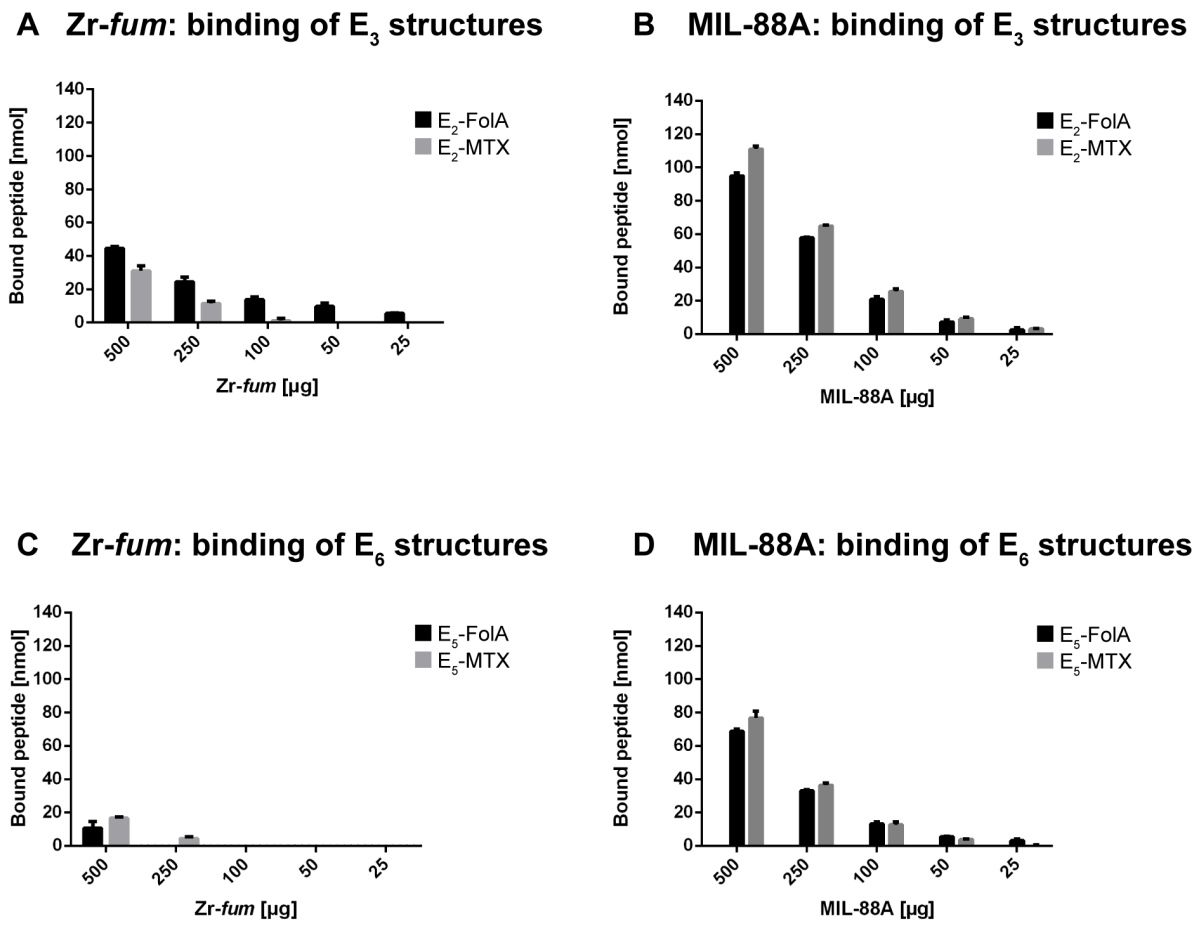

Figure 15 Binding capacity evaluation for E_n-MTX and comparison with E_n-tag bindings. A defined quantity of binding structure was incubated with varying amounts of MOF and subsequently centrifuged. Binding capacities were calculated by photometrically quantifying unbound binder remaining in the supernatant and substraction from the initially offered amount. The top row shows binding capacities for E_3-modified structures determined on **A**) Zr-*fum* or **B**) MIL-88A whereas the bottom row displays binding capacities for E_6-modified structures on **C**) Zr-*fum* or **D**) MIL-88A.

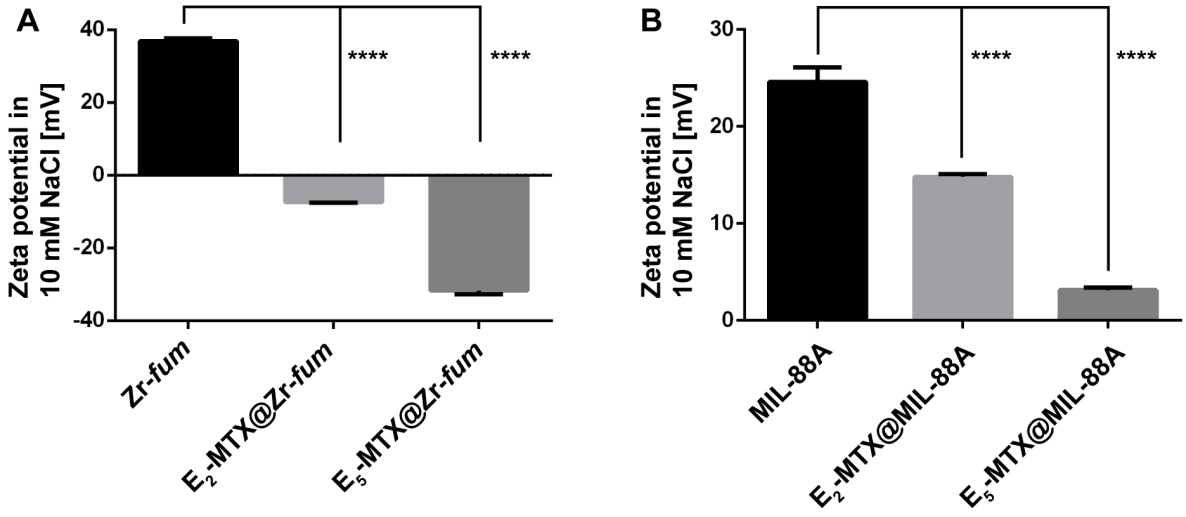

Figure 16 Influence of E_n-MTX binding on zeta potentials for **A**) Zr-*fum* or **B**) MIL-88A. After E_n-MTX binding, MOFs were centrifuged, washed and dispersed in 10 mM NaCl. Statistical analysis was performed by two-way ANOVA, α = 0.05, n = 3.

After it was now confirmed that polyglutamylated MTX derivatives do indeed bind to the selected MOFs to the approximate extent expected, the influence of binding on MOF zeta potentials was examined and a significant reduction depending on the number of glutamates within the cargo was observed (**Figure 16**).

At neutral assay pH, unmodified Zr-*fum* displayed a zeta potential of 36.8 ± 0.9 mV in 10 mM NaCl (Figure 16A). The observed value decreased to - 7.35 ± 0.15 mV (E_2-MTX@Zr-*fum*) and - 31.7 ± 1.0 mV (E_5-MTX@Zr-*fum*), respectively.

For MIL-88A, a similar trend was noted (Figure 16B). Here, the experiment revealed zeta potentials of 24.6 ± 1.5 mV (MIL-88A), 14.8 ± 0.3 mV (E_2-MTX@MIL-88A) and 3.14 ± 0.25 mV (E_5-MTX@MIL-88A).

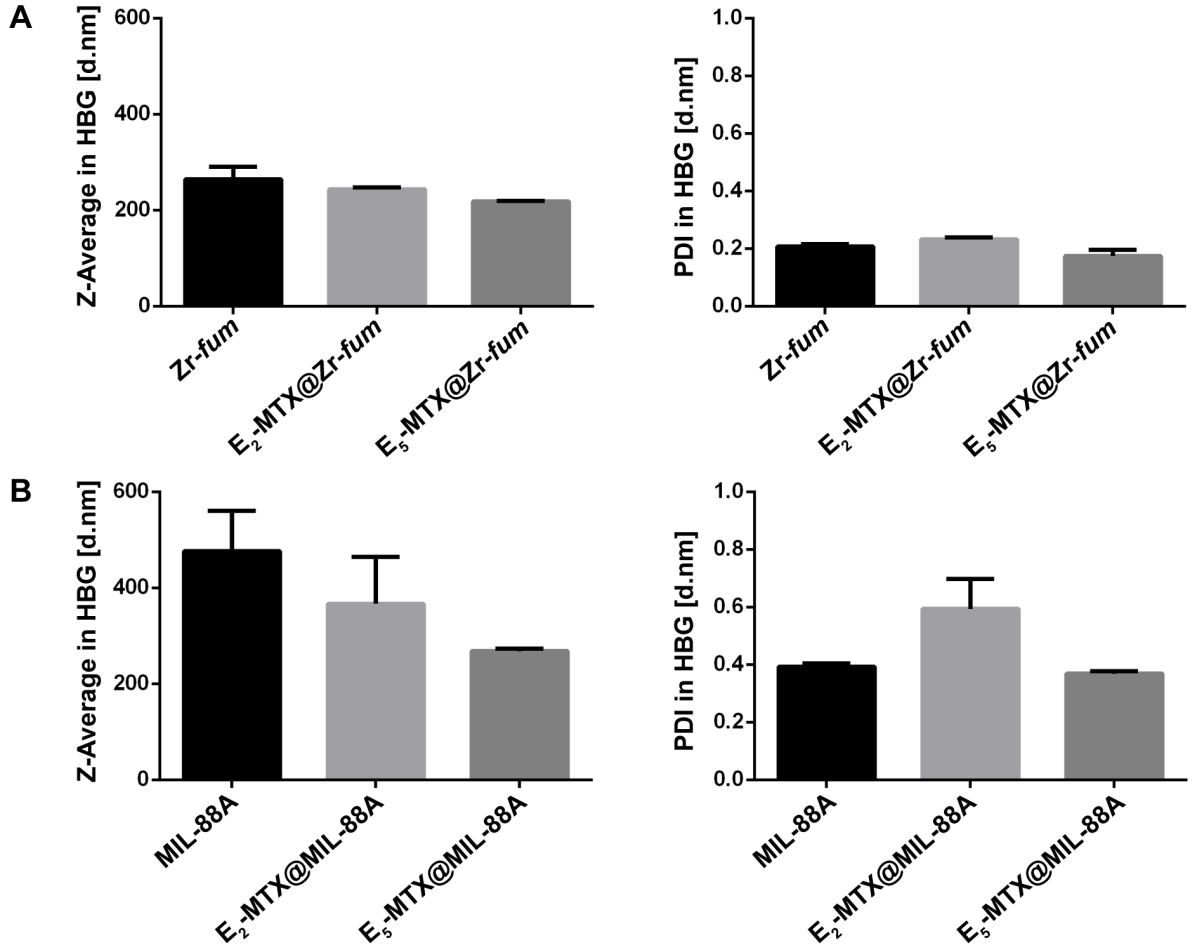

Figure 17 Influence of E_n-MTX binding on z-Average (left column) and PDI (right column) determined at neutral pH in HBG for **A**) Zr-*fum* or **B**) MIL-88A. For both Zr-*fum* and MIL-88A, functionalizing the MOF with E_n-MTX resulted in a decrease in observed size and PDI which was more pronounced for E_5-MTX.

Then, the effects of E_n-MTX attachment on MOF sizes in HBG were investigated by DLS (**Figure 17**). Here, for both Zr-*fum* (Figure 17A) and MIL-88A (Figure 17B), E_n-MTX functionalization resulted in beneficial effects. Whereas non-functionalized Zr-*fum* displayed a z-Average of 264 ± 26 nm, sizes decreased to 244 ± 4 nm (E_2-MTX@Zr-*fum*) and 218 ± 1 nm (E_5-MTX@Zr-*fum*), respectively. With regard to PDIs, values of 0.207 ± 0.009 (Zr-*fum*), 0.233 ± 0.007 (E_2-MTX@Zr-*fum*) and 0.175 ± 0.021 (E_5-MTX@Zr-*fum*) were determined. Interestingly, functionalizing MIL-88A led to similar results. Here, evaluation by DLS revealed sizes of 476 ± 84 nm (MIL-88A), 367 ± 97 nm (E_2-MTX@ MIL-88A) and 268 ± 5 nm (E_5-MTX@ MIL-88A). Recorded PDIs followed a complementary trend with recorded values of 0.393 ± 0.011 (MIL-88A), 0.594 ± 0.104 (E_2-MTX@ MIL-88A) and 0.369 ± 0.008 (E_5-MTX@ MIL-88A).

Then, the formulations were evaluated *in vitro* by MTT assay on adherent human cervix carcinoma KB (Figure 18) and suspension mouse lymphocytic leukemia cells (Figure 19).

Initially, both cell lines were treated with 10 µg of Zr-*fum* or MIL-88A which is more than the subsequently used MOF amount. Here, no MOF-related reduction in cell viabilities was observed (data not shown).

For KB cells (**Figure 18**), testing MTX in a concentration range between 0.1 nM and 10 nM followed by curve-fit based on nonlinear regression determined an EC_{50} of 4.237 nM. At 4.438 nM (E_2-MTX) and 9.883 nM (E_5-MTX), the pre-polyglutamylated MTX compounds on their own were less potent. By attachment to Zr-*fum,* reduced EC_{50} values of 1.451 nM (E_2-MTX@Zr-*fum*) and 3.757 nM (E_5-MTX@Zr-*fum*) were achieved. Importantly, those two calculated values are below both the EC_{50} of MTX and its respective polyglutamylated forms and highlight the potential benefits of MOF-based E_n-MTX delivery. Within the evaluated set, delivery by attachment to MIL-88A was less promising. Here, E_2-MTX@MIL-88A displayed a calculated EC_{50} of 4.890 nM which is marginally above the 4.438 nM observed for free E_2-MTX. However, due to the two values being that similar, it is difficult to arrive at a final conclusion. For E_5-MTX@MIL-88A, MOF-based delivery slightly reduced the EC_{50} to 9.755 nM which is almost identical to the EC_{50} observed for free E_5-MTX (9.883 nM) and still above free MTX (4.237 nM).

Screening highly sensitive L1210 cells (**Figure 19**) revealed a reduced effect of E_n-MTX delivery by MOF. Respective EC_{50} values of 0.568 nM (MTX) and 2.120 (E_2-MTX) were observed. Delivering E_2-MTX by Zr-*fum* or MIL-88A increased EC_{50} values to 4.411 nM and 3.639 nM, respectively. For both E_5-MTX and its MOF-bound forms, no EC_{50} values could be determined since no dose response was observed within the screened concentration range.

In sum, beneficial effects of MOF-based E_n-MTX delivery as reflected in lowered EC_{50} values compared to the free drugs were achieved on KB cells. Here, the best results were obtained utilizing Zr-*fum*. Notably, both E_2-MTX@Zr-*fum* and E_5-MTX@Zr-*fum* were found to be more potent than free MTX or the respective free E_n-MTX species with the effect being more pronounced for E_2-MTX delivery.

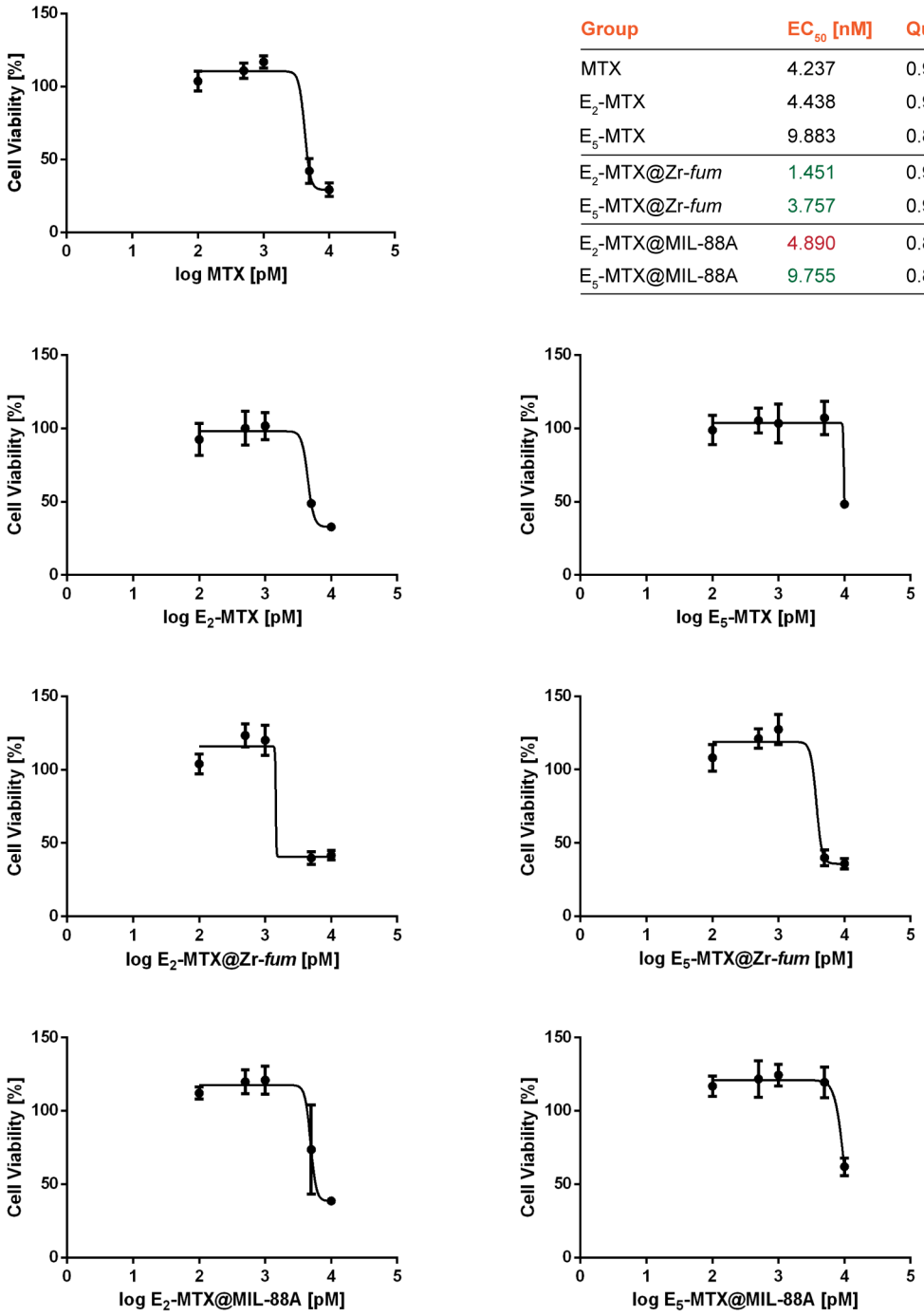

Group	EC_{50} [nM]	Quality [R^2]
MTX	4.237	0.9664
E_2-MTX	4.438	0.9264
E_5-MTX	9.883	0.8535
E_2-MTX@Zr-*fum*	1.451	0.9428
E_5-MTX@Zr-*fum*	3.757	0.9500
E_2-MTX@MIL-88A	4.890	0.8471
E_5-MTX@MIL-88A	9.755	0.8860

MTT assay, KB cells, 72h treatment, n = 5

Figure 18 *In vitro* evaluation of E_n-MTX@MOF on KB human cervix carcinoma cells. After 72 h of treatment with the indicated compound, cell viabilities were determined by MTT assay. EC_{50} values (top right) were calculated by nonlinear regression [curve fit, log(Inhibitor vs. response, variable slope) fitting method least squares fit]. The best-fit EC_{50} values are shown in combination with the respective R^2 as an indication of fit quality. Cellular testing was performed by Miriam Höhn, Department of Pharmacy, LMU Munich.

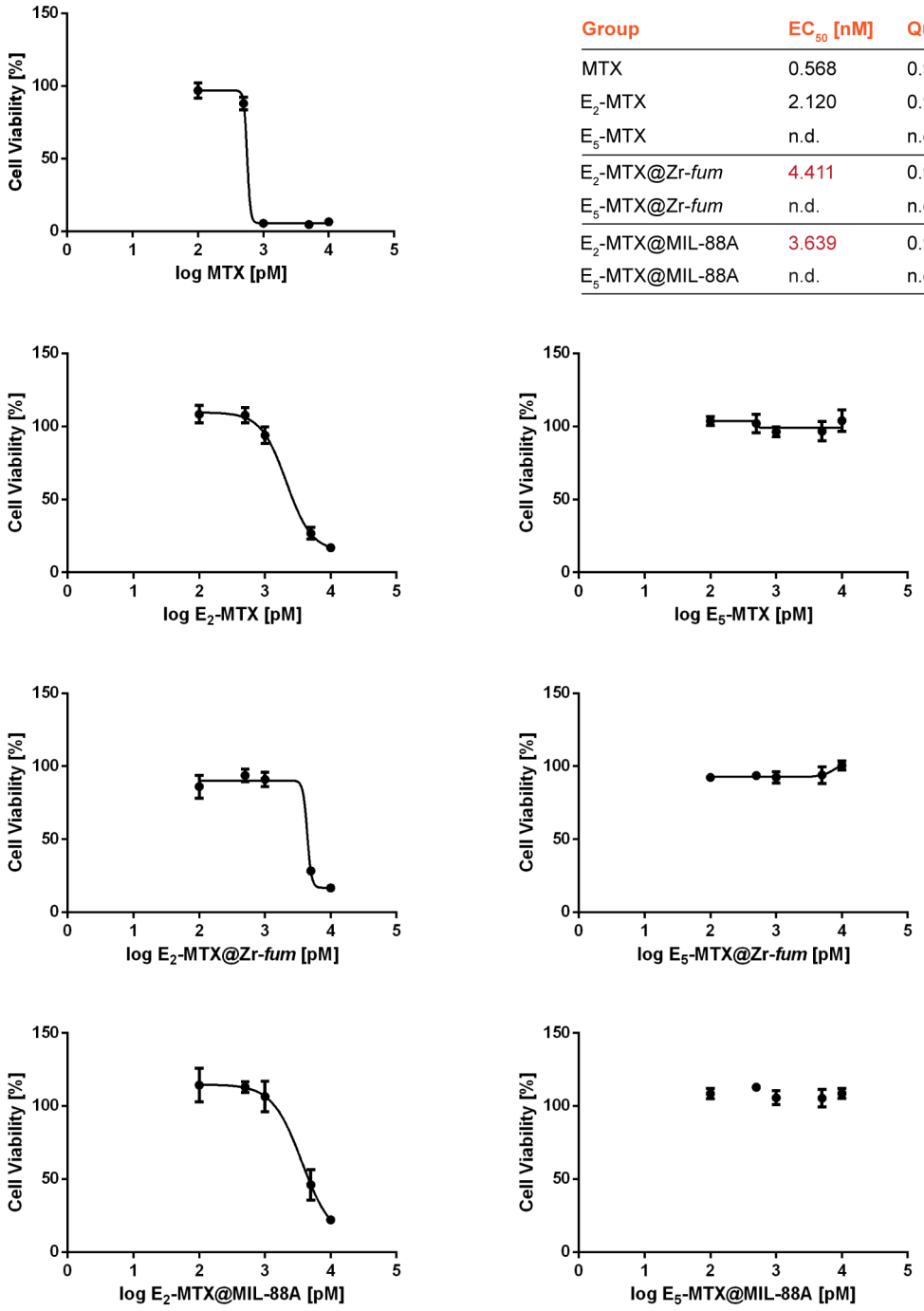

Group	EC_{50} [nM]	Quality [R^2]
MTX	0.568	0.9957
E_2-MTX	2.120	0.9885
E_5-MTX	n.d.	n.d.
E_2-MTX@Zr-*fum*	4.411	0.9792
E_5-MTX@Zr-*fum*	n.d.	n.d.
E_2-MTX@MIL-88A	3.639	0.9622
E_5-MTX@MIL-88A	n.d.	n.d.

MTT assay, L1210 cells, 72h treatment, n = 5

Figure 19 *In vitro* evaluation of E_n-MTX@MOF on L1210 mouse lymphocytic leukemia cells. After 72 h of treatment with the indicated compound, cell viabilities were determined by MTT assay. EC_{50} values (top right) were calculated by nonlinear regression [curve fit, log(Inhibitor vs. response, variable slope) fitting method least squares fit]. The best-fit EC_{50} values are shown in combination with the respective R^2 as an indication of fit quality. For E_5-MTX and E_5-MTX@MOF, no meaningful EC_{50} values could be calculated since no dose response was observed within the tested concentration range. Cellular testing was performed by Miriam Höhn, Department of Pharmacy, LMU Munich.

3.2 Core-shell functionalized zirconium-pemetrexed coordination nanoparticles as carriers with a high drug content

This chapter was adapted from:

B. Steinborn, P. Hirschle, M. Höhn, T. Bauer, M. Barz, S. Wuttke, E. Wagner, U. Lächelt. *Core-Shell Functionalized Zirconium-Pemetrexed Coordination Nanoparticles as Carriers with a High Drug Content*. Advanced Therapeutics **2019**, 2, 1900120.

Background. *This chapter describes the formulation development, surface functionalization and subsequent in vitro screening of a novel type of NCP based on pemetrexed, an antifolate drug mainly used to treat non-small cell lung cancer, and zirconium (IV) ions. The presented strategy for the assembly of a multifunctional nanopharmaceutical with a very high drug content is considered to be a versatile platform translatable to other drug molecules with functional groups capable of coordinative interaction with metal ions.*

3.2.1 Synthesis and characterization of zirconium-pemetrexed NP cores

Scheme 7 provides an overview of the sequential assembly of multifunctional Zr-PMX NPs. The drug-containing NP core was generated in EtOH using the synthetic parameters described in Scheme 7A. Scheme 7B depicts the addition of a silica layer to enhance the NP core stability. The external silica surface is finally coated with a polyglutamate-block-polysarcosine block copolymer for simultaneous colloidal stabilization, sterical shielding, and attachment of targeting ligands as illustrated in Scheme 7C.

Zirconium(IV) was chosen as the metal component for the assembly of the drug containing NP core due to its ability to form stable metal-organic complexes with suitable biological tolerability as observed before with other Zr-based MOFs and drug delivery systems.[175] The particles were formed at room temperature within 45 min in an ethanol-water mixture containing HCl and 100 equivalents of formic acid as additives for control of particle growth.

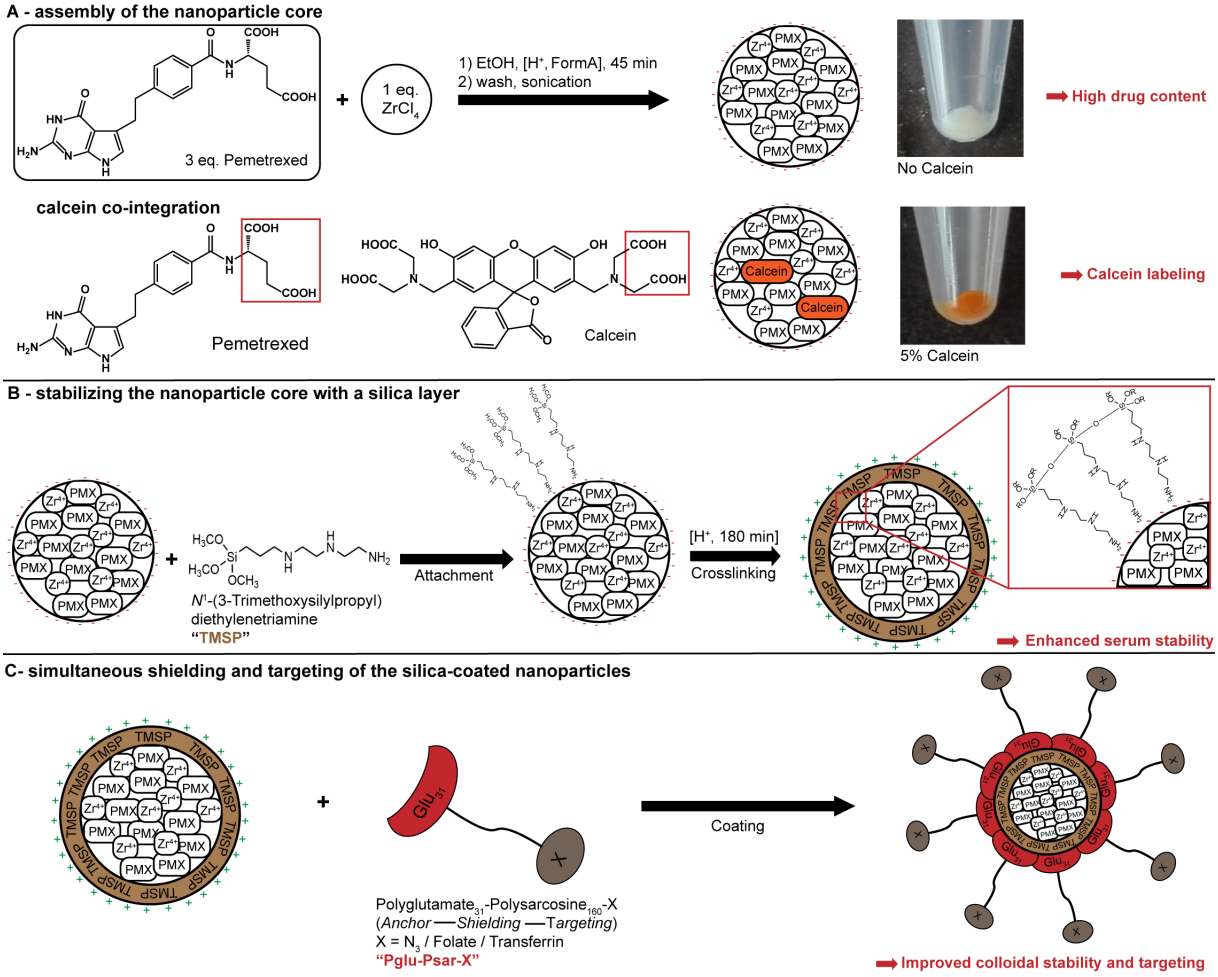

Scheme 7 Overview of the utilized core-shell nanoparticle (NP) assembly approach. **A**) Synthesis of the drug-containing NP core and labeling by coordinative integration of fluorescent calcein dye; **B**) stabilization of the NP core by a polymerized silica shell; and **C**) simultaneous shielding and targeting by coating with polyglutamate-polysarcosine block copolymers.

The optimal linker:metal ratio varies upon different Zr-based metal-organic nanomaterials, such as 1:1[176] or 3:1,[65, 177] therefore a range of PMX to Zr stoichiometries was initially screened in this study. A molar excess of PMX is favorable in terms of lower polydispersity indices (PDIs), as observed for 3:1 and 3:2 ratios compared to equimolar 3:3 (**Figure 20**) with z-averages between 130 and 220 nm. In case of excessive Zr at a 3:6 ratio, only minor particle formation could be observed within the 45 min reaction time. A possible explanation lies within a higher number of initially formed crystal nuclei which results in the NP growth being distributed over more individual particles leading to slower growth of single particles as described by Wang *et al.*[178] Satisfactory PDI and particle yield were achieved at a 3:1 PMX to Zr ratio and these conditions were used for subsequent studies.

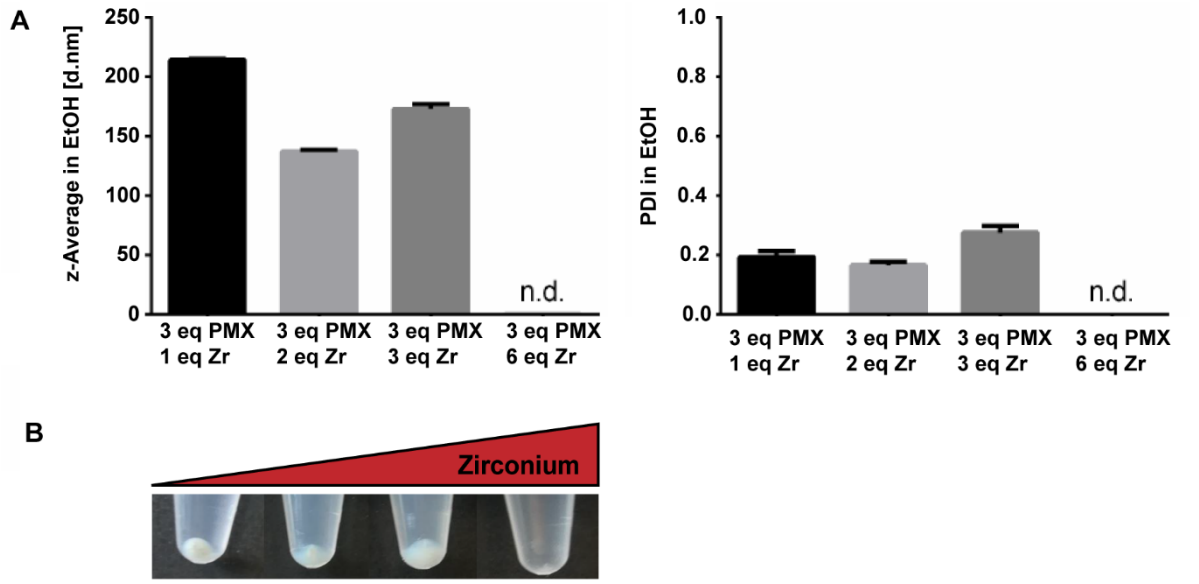

Figure 20 Screening of different metal to linker stoichiometries. Particle sizes were determined in EtOH by dynamic light scattering. At the 3:6 ratio, no measurable particle formation was observed. **A**) left: z-averages in EtOH, right: PDIs in EtOH. **B**) Corresponding sample pellets obtained after 45 minutes of synthesis and subsequent centrifugation. Here, smaller observed pellets indicate that increasing the equivalents of zirconium offered during the synthesis beyond 3:3 strongly reduces the amount of obtained nanomaterial.

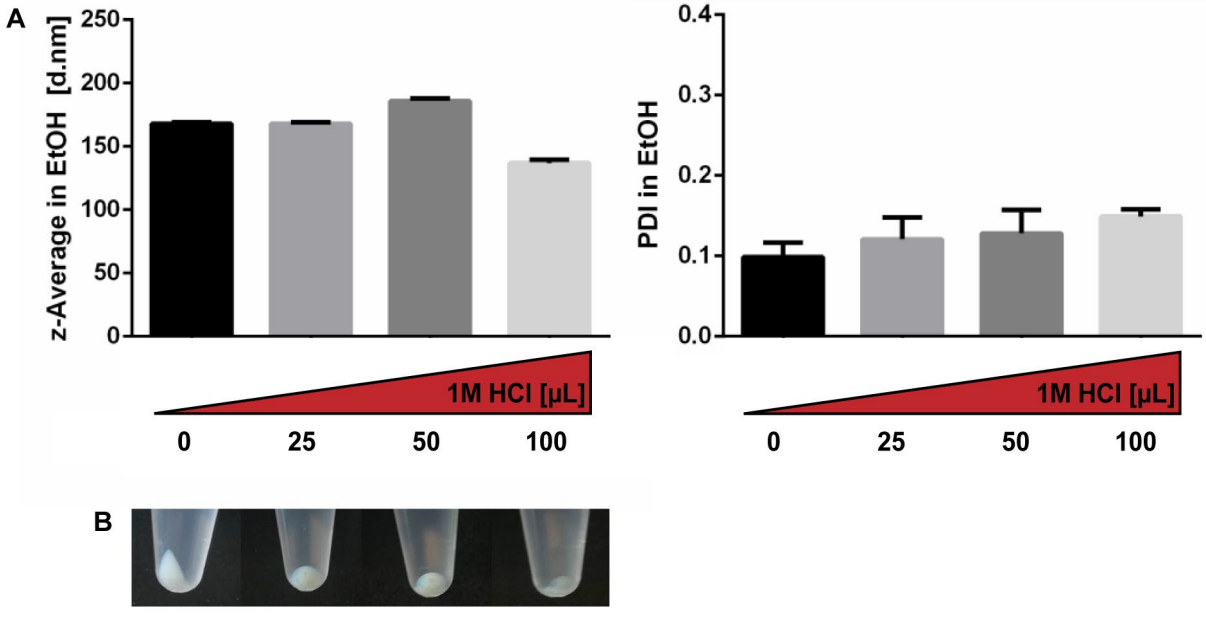

Figure 21 Screening of various amounts of added HCl with regard to size, PDI and the amount of obtained nanoparticle. All samples contain 100 eq. formic acid (46.5 µL) + x µL 1M HCl. Each sample is composed of 3 eq. PMX, 1 eq. Zr and was incubated for 45 minutes. **A**) Characterization by DLS, **B**) corresponding obtained pellet sizes after 45 minutes of particle assembly.

In order to generate particles within the nanometer size range suitable for biological applications,[179] acid was added to the reaction mixture (**Figure 21**). For samples without any acidification, rapid clouding and formation of particles in the micrometer range was observed. By adding 100 equivalents formic acid, a monodentate modulator also used for MOF synthesis,[180] this immediate aggregation was prevented and the particle formation occurred more slowly. Additional HCl only had a minor influence on size and PDI, but reduced the amount of obtained nanoparticle.

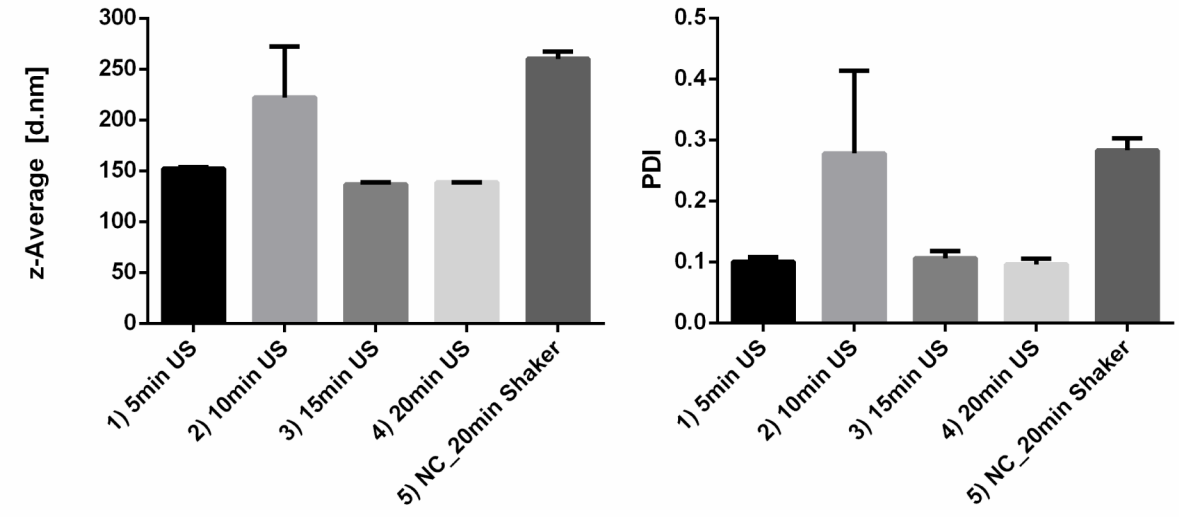

Figure 22 Influence of ultrasound (US) duration on obtained nanoparticle sizes as determined by DLS. After synthesis and wash, Zr-PMX-NPs were subjected to various durations of sonication whereas incubation on a tabletop shaker served as control. Left: z-averages in EtOH, right: PDIs in EtOH.

Sonication of the obtained NPs mediated favorable effects on the particle size by disaggregating agglomerates formed during the centrifugation and washing steps (**Figure 22**). The overall effect of sonication was about 100 nm of size decrease as determined by comparison with the negative control and 5 min of sonication were found to be sufficient, longer durations did not mediate a further improvement.

It was found that the fluorescent dye calcein, which contains several Lewis base functions and forms chelates with metal ions, can be co-assembled into the NP core. Notably, the addition of 5% calcein only had a minor influence on z-average and PDI (**Figure 23**) and enables direct fluorescence-based detection by confocal microscopy or flow cytometry studies without the requirement for additional labeling.

Importantly, this illustrates the flexibility of the presented particle assembly concept and the possibility to encapsulate different cargos.

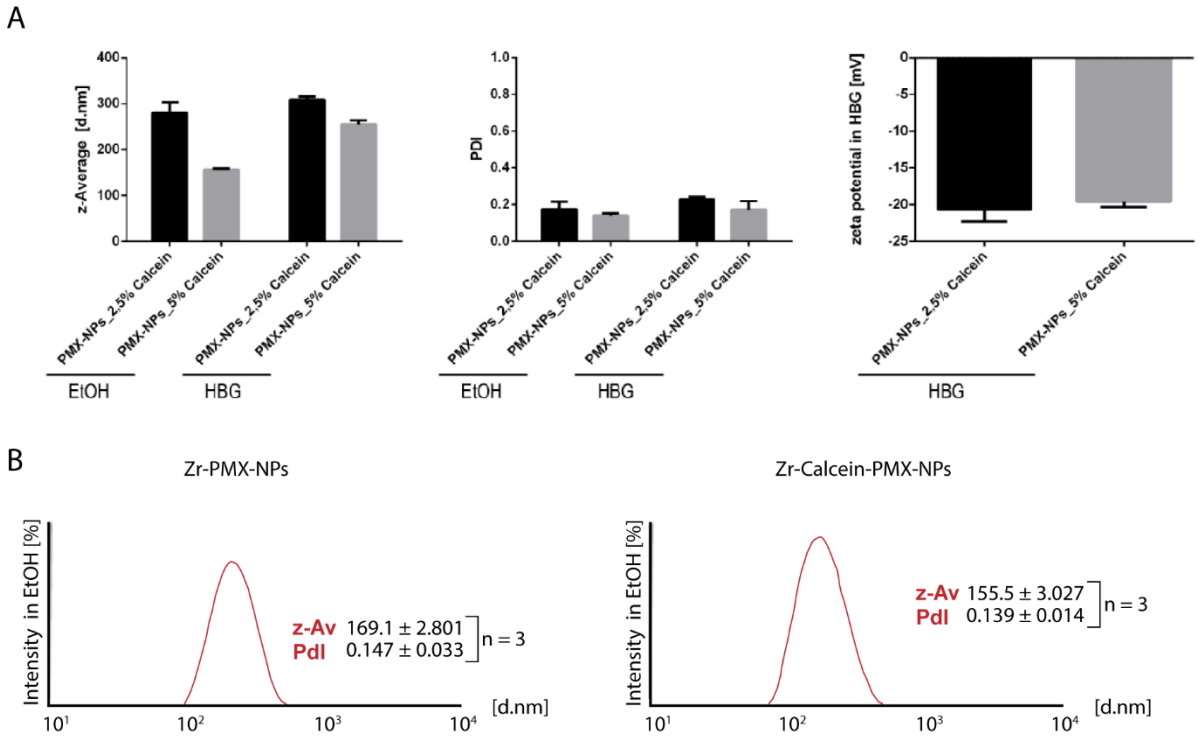

Figure 23 Formulation development and characterization of calcein-labeled Zr-PMX-NPs. **A**) Screening of different calcein amounts and solvents with regard to z-Average, PDI and zeta potential by DLS, **B**) representative intensity size distributions comparing Zr-PMX-NPs (left) and Zr-PMX-NPs assembled with 5% calcein (right).

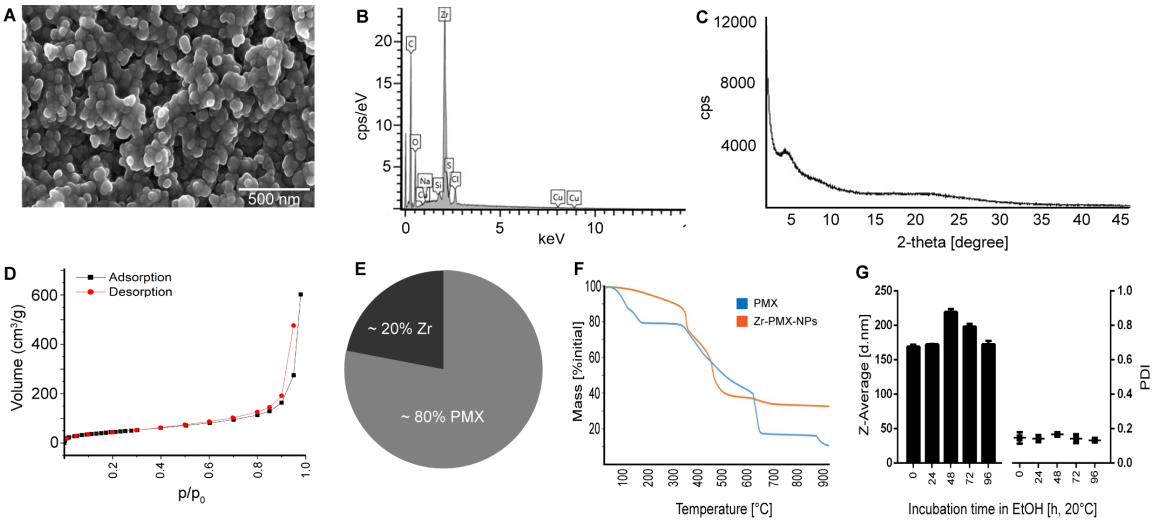

Figure 24. Physiochemical characterization of the NP core containing the drug payload. **A**) Imaging by scanning-electron microscopy; **B**) qualitative elemental composition determined by energy dispersive X-ray spectroscopy; **C**) analysis of crystallinity by X-ray diffraction; **D**) measurement of porosity by nitrogen sorption analysis; **E**) particle composition by ICP–AES and HPLC (mean, n = 3); **F**) thermogravimetric analysis; and G) particle size, polydispersity and stability in ethanol by dynamic light scattering (mean ± SD, n = 3). SEM imaging and EDX were performed by Dr. Steffen Schmidt, XRD by Patrick Hirschle, BET and TGA by Tina Reuther (Department of Chemistry, LMU Munich). ICP-AES was conducted by Jaroslava Obel (Central Analytics, LMU Munich).

The NP core (Scheme 7A) was then further investigated with regard to its physicochemical properties (**Figure 24**).

Here, additional analysis by scanning-electron microscopy (SEM, Figure 24A) revealed a particle diameter of 64.26 ± 10.09 nm (n = 100). The difference in size compared to the previously presented DLS data can be attributed to the individual techniques, SEM-imaging measures particles in dry form whereas DLS determines their hydrodynamic diameter in solution.[181]

Energy dispersive X-ray spectroscopy (Figure 24B) confirmed the presence of key elements, oxygen and carbon as part of the PMX structure and zirconium as well as chloride due to the used metal compound and the added HCl. The carbon signal can also be partially attributed to the conductive carbon layer added during SEM sample preparation.

X-ray diffraction (XRD) (Figure 24C) did not show crystallinity, which is why an amorphous structure was assumed for Zr-PMX NPs.

The porosity and surface area of the dried NPs were investigated using nitrogen sorption (Figure 24D). Evaluating the sorption isotherms with the BET method[182] resulted in a surface area of 170 $m^2\ g^{-1}$, suggesting porosity in the sample. Both the nitrogen sorption isotherm and the corresponding pore size distribution indicate this porosity stems mainly from mesopores starting at 40 Å.

Next, the PMX to Zr mass ratio present in the NP core was determined (Figure 24E) by inductively coupled plasma atom emission spectrometry (ICP-AES) and high-performance liquid chromatography (HPLC). ICP-AES revealed a Zr content of 20.03 ± 0.96% (m/m, n = 3). NP lysis followed by PMX quantification by HPLC showed a PMX content of 78.23 ± 1.83% (m/m, n = 3).

Similarly high drug contents have been observed by Heck *et al.* for other zirconium-based drug formulations.[117c, 183] Considering the Zr(IV) coordination number of six and two coordinatively active carboxy functions per PMX molecule, the obtained result is close to the hypothetical PMX to Zr ratio of 3 and also corresponds to the feed ratio during NP synthesis.

For Zr-PMX NPs, thermogravimetric analysis indicated a residual particle mass of 33.85% (Figure 24F). As the NP sample was heated in a mixed N_2/O_2 atmosphere, which led to the formation of ZrO_2, the actual metal content is lower. By excluding the oxide formation (MW ZrO_2 = 123.22 g mol^{-1}, MW Zr = 91.22 g mol^{-1}, factor: 1.35), the amount of non-oxidized Zr present in the NP can be estimated as 33.85 % divided by 1.35 = 25.05 %, which differs only slightly from the result determined by ICP–AES and also agrees very well with the hypothetical particle composition.

Next, the long-term stability of as-synthesized NPs (Figure 24G) was evaluated in ethanol (EtOH) at room temperature by performing DLS measurements every 24 h. After 48 h, a minor increase in z-average was observed whereas the PDI remained unchanged over 96 h. As a precaution, the freshly prepared NPs were thus stored for a maximum of 24 h for all experiments.

The reproducibility of Zr-PMX-NP core synthesis with- or without calcein was then additionally investigated by SEM (**Figure 25**). Here, no changes in particle morphology were observed between three independently prepared batches indicating a robust synthetic protocol. Additionally, the morphology of particles containing calcein did not notably differ from the formulation generated without calcein.

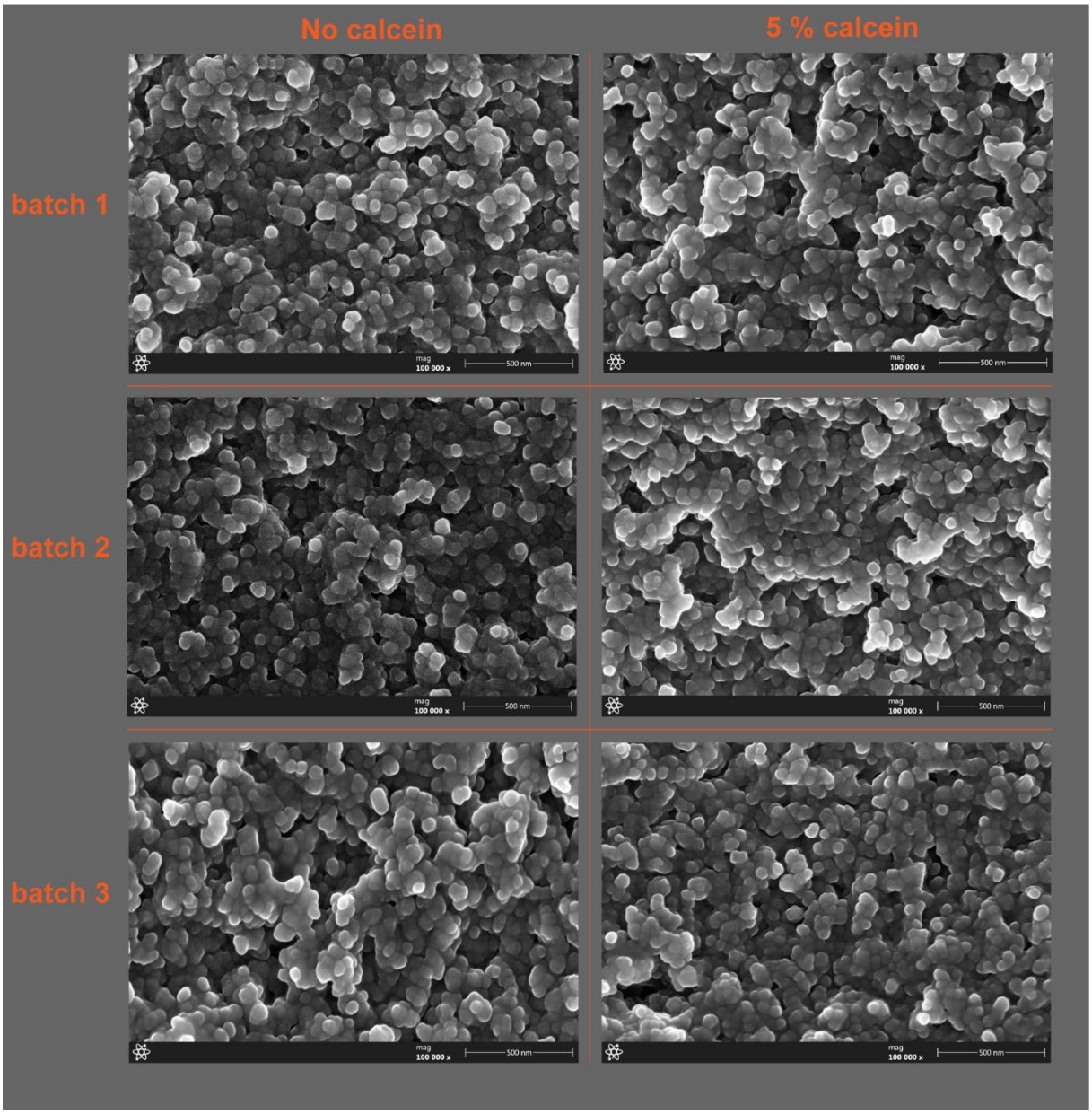

Figure 25 Both the synthesis of Zr-PMX-NPs with (right column) or without calcein (left column) leads to particles with highly reproducible morphologies. Of both formulations, 3 individual batches were prepared and imaged by scanning electron microscopy at 100.000x magnification, scale bars represent 500 nanometers. The images were recorded by Dr. Steffen Schmidt (Department of Chemistry, LMU Munich).

3.2.2 Silica coating of zirconium-pemetrexed nanoparticle cores enhances their serum stability and uptake into cancer cells

Background. *Initial exploratory serum stability studies of the as-synthesized Zr-PMX NP core (data not shown) revealed a high PMX release within 30 min of serum incubation. In order to increase and control the stability, a silica coating strategy was therefore developed and applied to the nanosystem.*

Although tetraethylorthosilicate (TEOS) is commonly used for silica coatings,[184] this study utilized *N*[1]-(3-trimethoxysilylpropyl)diethylenetriamine (TMSP) instead, which has, to the best of my knowledge, only been previously employed as a silica coating agent in a physicochemical setting[185] but not for a biological or drug delivery application.

Coating NPs with a silica shell based on TEOS by applying the Stöber method[186] typically requires an interfacing step by attaching a polymer, such as poly-(vinylpyrrolidone) (PVP), to the NP surface in order to maintain colloidal NP stability under the conditions of the Stöber process.[184b, 187] However, such a step introduces additional complexity to the system and the used type of PVP determines the final particle characteristics.[187]

Liz-Marzán *et al.* directly coated gold NPs using (3-aminopropyl)trimethoxysilane as the interfacing agent before applying the Stöber method to deposit an additional TEOS layer.[188] This inspired the use of TMSP which was perceived as even more suitable compared to (3-aminopropyl)trimethoxysilane due to its diethylenetriamine motif providing additional interaction sites for coordinative and/or electrostatic attachment to the surface of Zr-PMX NPs (Scheme 7B).

As shown in **Figure 26**, the influence of the used TMSP amount and coating duration was initially screened by DLS (Figure 26A), then, the obtained Zr-PMX@TMSP NPs were further characterized by scanning electron microscopy (SEM), energy dispersive x-ray spectroscopy (EDX), and X-ray diffraction (XRD).

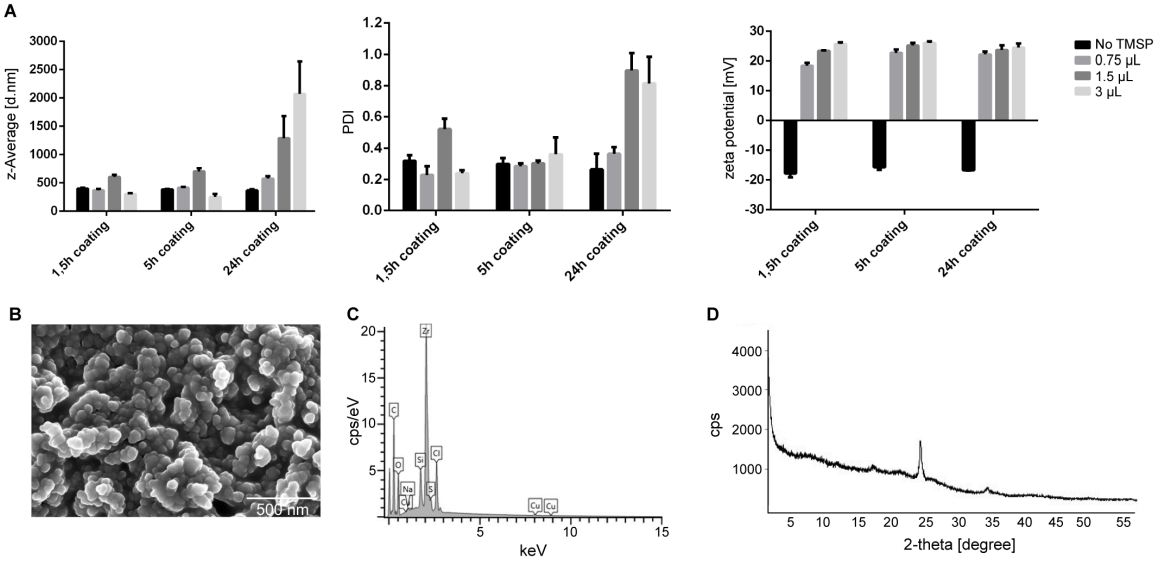

Figure 26 Characterization of the silica coating. **A**) Effects of TMSP amount and coating duration on particle size determined by dynamic light scattering (mean ± SD, n = 3); **B**) imaging of the silica-coated NPs by scanning-electron microscopy; **C**) qualitative elemental analysis by energy dispersive X-ray spectroscopy and **D**) evaluation of crystallinity by X-ray diffraction. SEM and EDX were performed by Dr. Steffen Schmidt, Department of Chemistry, LMU Munich. PXRD was recorded by Patrick Hirschle, Department of Chemistry, LMU Munich.

Interestingly, coating times up to 5 h with the highest tested TMSP amount of 3 µL resulted in small NPs and similar PDI values whereas 24 h of coating with TMSP amounts of 1.5 µL or higher resulted in strong particle aggregation and increased polydispersity. Coating mediated a zeta potential inversion from −20.8 ± 0.6 mV to 25.9 ± 1.1 mV or higher, which did not change further after 5 h of coating time.

After performing an aqueous wash to remove silica polymerization by-products (**Figure 27**), SEM imaging (Figure 26B) indicated a silica-coated NP size of 74.57 ± 16.64 nm (n = 100), which implies an increase in diameter of approximately 10 nm compared to the uncoated NP core and, thus, a silica shell thickness of about 5 nm.

Besides the increase in size and the observed zeta potential inversion, EDX analysis (Figure 26C) also confirmed the presence of a silica peak.

X-ray diffraction (XRD) analysis (Figure 26D) revealed an additional peak at a 2-θ of approximately 25° which can be attributed to polymerized TMSP; a control spectrum of polymerized TMSP without NPs (**Figure 28**) revealing the characteristic peak confirms this suggestion.

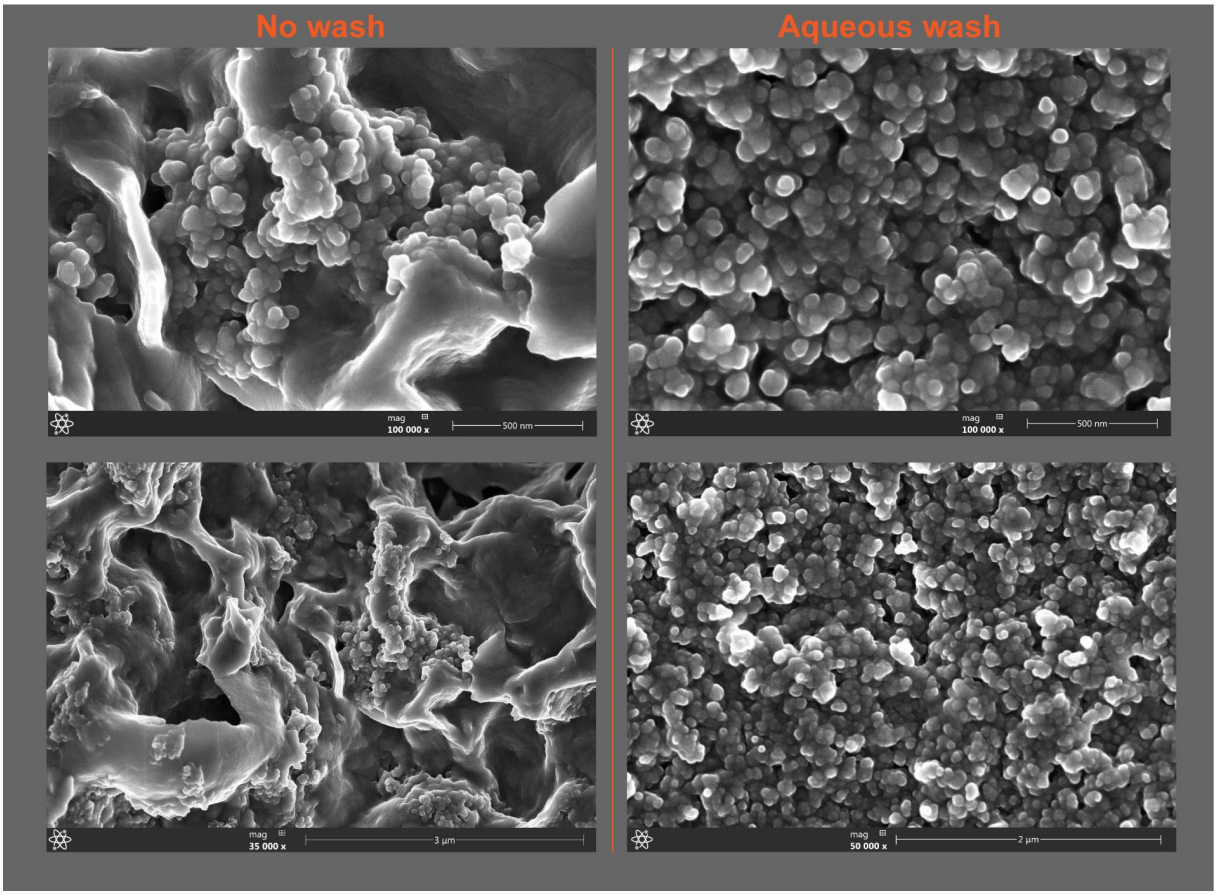

Figure 27 Influence of an aqueous washing step performed after the silica coating determined by SEM imaging at different magnifications; top row: close-up, bottom row: overview. After 3h of TMSP-coating, the obtained Zr-PMX@TMSP NPs were either washed with EtOH only (left column) or subjected to an additional aqueous wash (right column) Here, the absence of TMSP flakes can be observed. Imaging was performed by Dr. Steffen Schmidt, Department of Chemistry, LMU Munich.

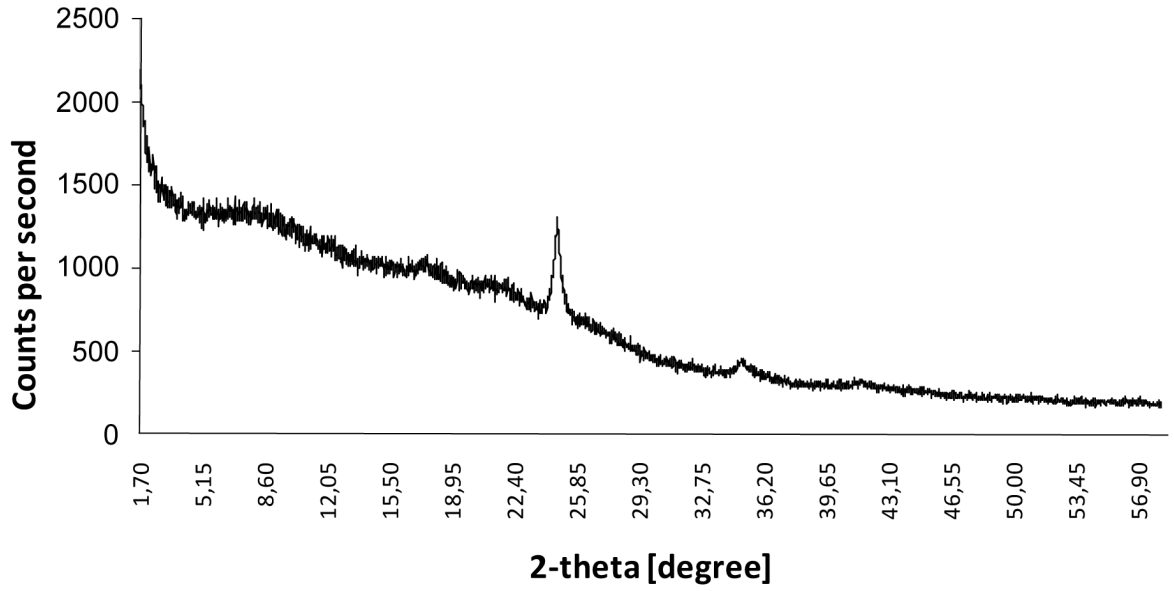

Figure 28 X-ray diffraction spectrum of polymerized TMSP recorded by Patrick Hirschle, Department of Chemistry, LMU Munich.

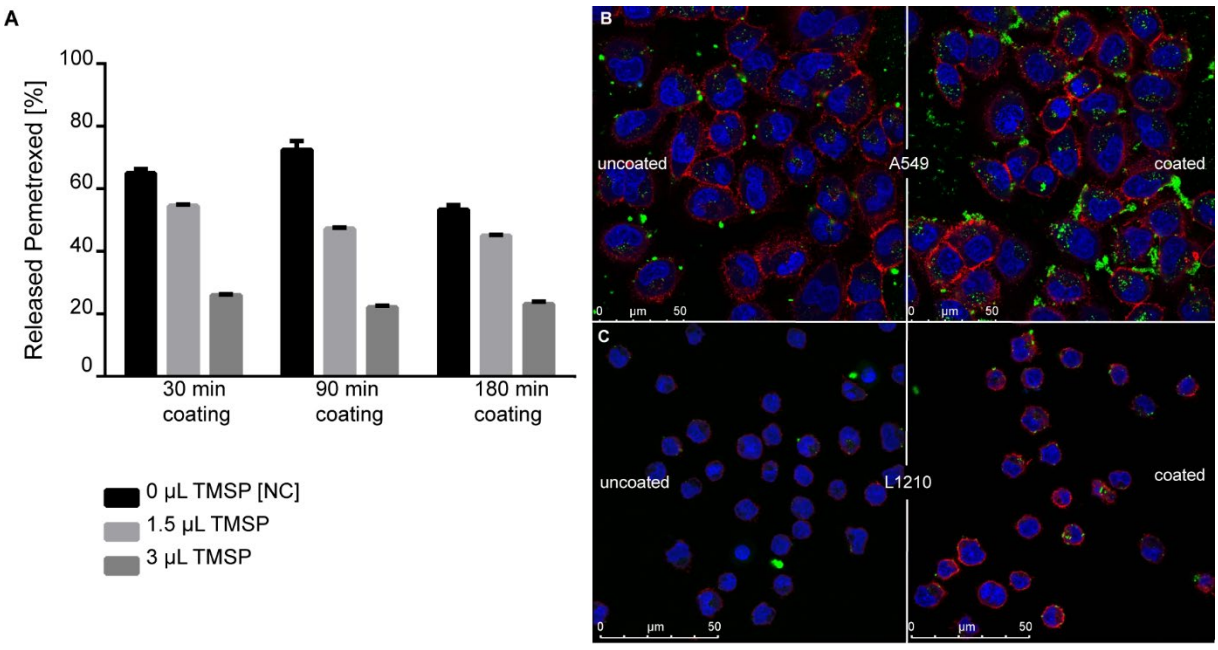

Figure 29 The silica coating enhances the serum stability and promotes NP uptake into cancer cells. **A**) Serum stability of TMSP-coated NPs determined by HPLC (mean ± SD, n = 3); **B**) effects of the coating on NP uptake into adherent A549 lung adenocarcinoma or (**C**) suspension L1210 leukemia cells visualized by CLSM. Green, NP core labeled by coordinative integration of calcein; Red, actin stained with phalloidin-rhodamine; Blue, nuclei stained with DAPI. CLSM images were recorded by Miriam Höhn, Department of Pharmacy, LMU Munich.

Next, the effects of the silica coating on the serum stability were evaluated in a time- and dose-dependent manner (**Figure 29**). Here, a distinct effect of the TMSP amount

on the PMX release in serum (Figure 29A) was observed. After 30 min of incubation in 10% fetal bovine serum (FBS), approximately 70% of the incorporated PMX was released from the uncoated NPs. Coating with 1.5 µL TMSP reduced the release to approximately 50% independent of the coating duration. The stabilizing effect was further increased with 3 µL TMSP. Here, the observed PMX release was reduced to approximately 25 %. In all cases, the coating duration only had a minor effect on the serum stability.

It was hypothesized that the TMSP layer stabilizes the NP core by impairing interactions between PMX and serum protein. PMX is known to exhibit a high degree of protein binding[189] which might compete with the coordinative zirconium interactions that mediate formation of the NP core. Higher amounts of TMSP are likely to further enhance the stability. However, since the drug mediates its activity in a solubilized state and has to be released from the nano-colloids, the achieved TMSP effect was considered to represent a suitable balance between required stability and lability.

Next, the effect of the TMSP-coating on the uptake of calcein-containing Zr-PMX NP cores was evaluated on adherent A549 (human lung adenocarcinoma, Figure 29B) and L1210 (mouse lymphocytic leukemia Figure 29C) suspension cell lines using confocal laser scanning microscopy (CLSM). For both cell lines, the coating increased the overall NP uptake, likely due to the increased serum stability and the zeta inversion resulting in enhanced unspecific electrostatic uptake as described for other nanosystems.[33, 190] This observation was additionally confirmed using human cervix carcinoma KB cells and quantified by flow cytometry (**Figure 30**).

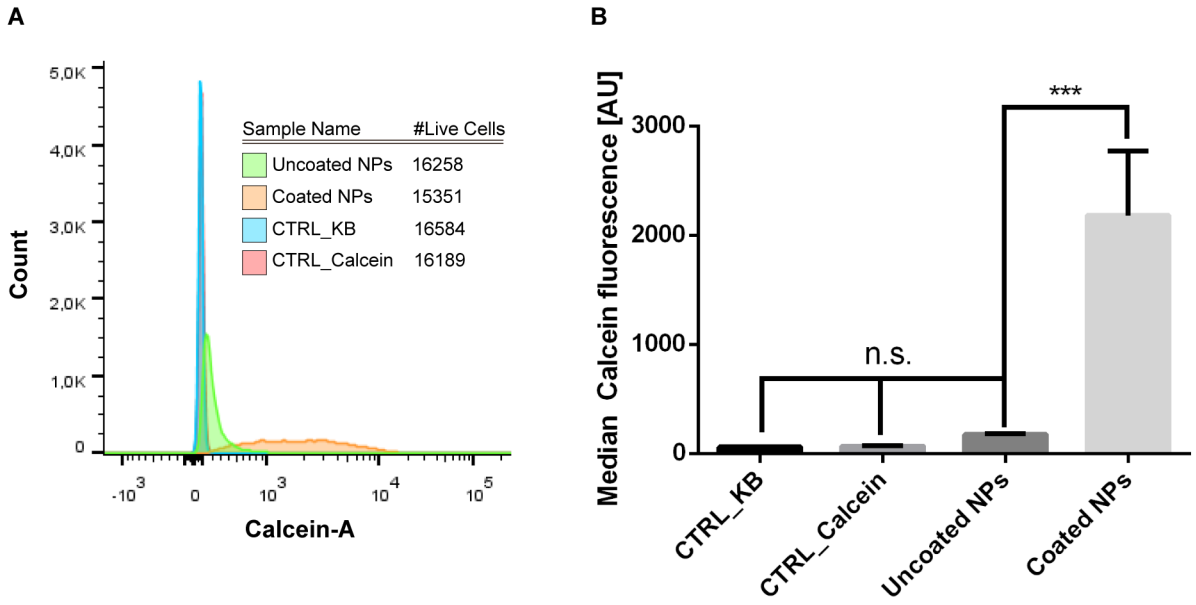

Figure 30 Evaluation of the uptake-enhancing effect of the TMSP shell as determined by flow cytometry. Zr-PMX NPs or Zr-PMX@TMSP NPs were incubated on KB cells for 1 h, afterwards, the medium was replaced, the cells incubated for an additional 2 h. **A)** distribution of calcein intensities. Blue: CTRL_KB cells, red: CTRL_free calcein at an equal concentration as present within the used amount of NP to exclude unspecific uptake of free calcein dye, green: Zr-PMX NPs, orange: Zr-PMX@TMSP NPs. **B**) obtained median calcein fluorescence values (mean ± SD, n = 3). Flow cytometry was performed by Miriam Höhn, Department of Pharmacy, LMU Munich.

Here, TMSP-coated Zr-PMX NPs mediated significantly higher median calcein fluorescence compared to uncoated NPs or free calcein. However, CLSM studies revealed external NP attachment to the cell membrane and extracellular aggregation was observed on multiple cell lines (**Figure 31**) which illustrated the need for further colloidal stabilization in a biological environment. Since increased colloidal stability of Zr-based MOFs has been achieved with a polyglutamate-blockpolysarcosine copolymer before,[153] this strategy was also adapted to Zr-PMX@TMSP NPs.

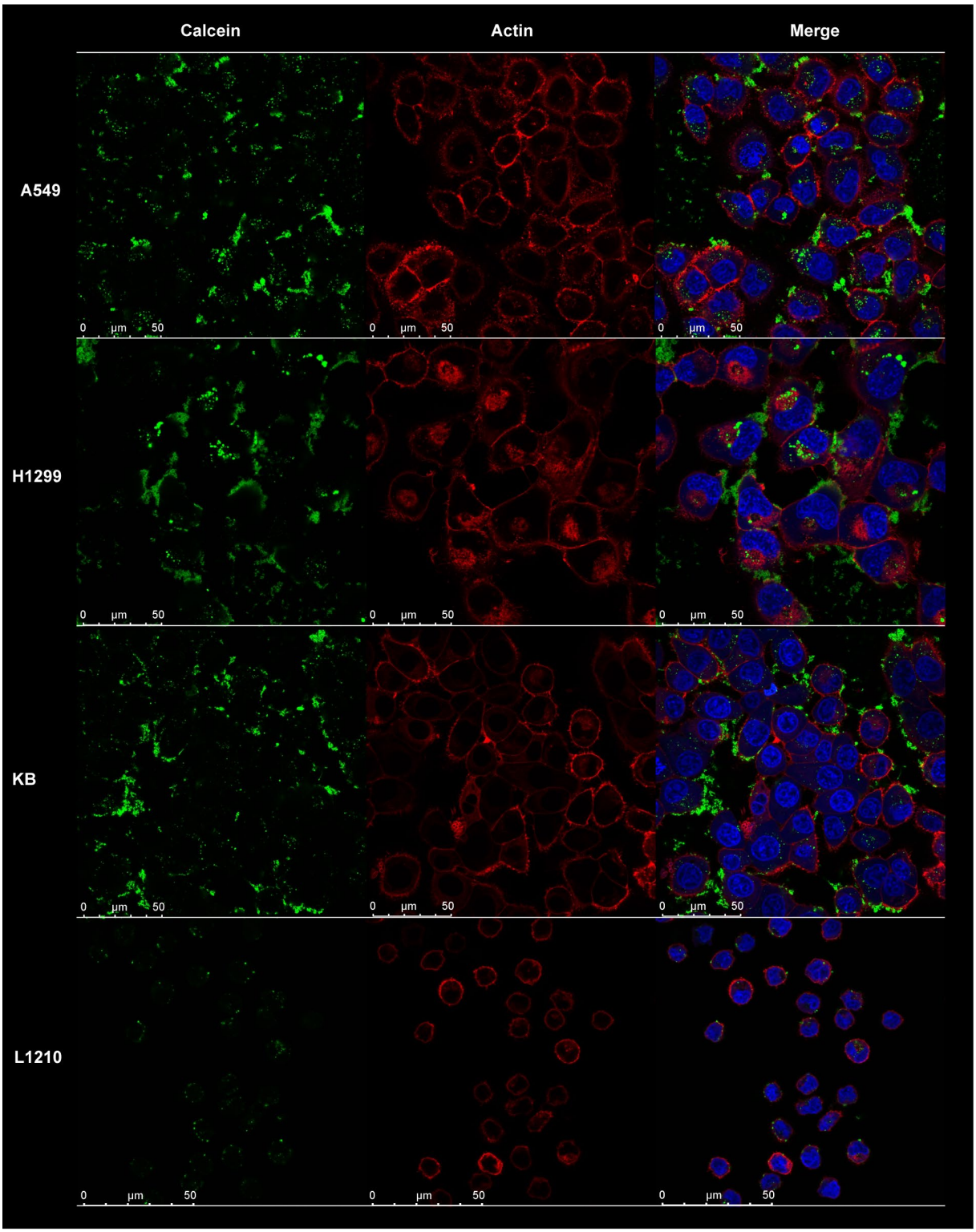

Figure 31 CLSM-imaging of Zr-PMX@TMSP NPs on multiple cell lines. After 1h of NP uptake, cells were washed, incubated an additional 3h, stained, fixated and imaged. Green, NP core labeled by coordinative integration of calcein; Red, actin stained with phalloidin-rhodamine; Blue, nuclei stained with DAPI. Cytosolic uptake, but also extracellular aggregation requiring further colloidal stabilization were observed on all cell lines except L1210. Rows from top to bottom: A549, lung adenocarcinoma; H1299 non-small cell lung carcinoma; KB, human cervix carcinoma; L1210, mouse lymphocytic leukemia. CLSM images were recorded by Miriam Höhn, Department of Pharmacy, LMU Munich.

3.2.3 Coating Zr-PMX@TMSP NPs with pGlu-*b*-pSar strongly improves the colloidal stability and mediates efficient shielding

In order to enhance the colloidal stability of Zr-PMX@TMSP NPs, a sterical shielding was implemented by surface coating with a polyglutamate$_{31}$-polysarcosine$_{160}$-N_3 (pGlu-*b*-pSar) block copolymer.[191]

It has been shown in previous studies with Zr-*fum* NPs that the polyglutamate block serves as the NP binding and surface attachment module while the polysarcosine block mediates efficient shielding, colloidal stabilization, and prevention of protein interactions.[85, 192] Additionally, Finsinger *et al.* reported steric stabilization and reduced complement activation for a cationic nanostructure coated with an anionic PEG-derived copolymer.[193]

In order to stabilize Zr-PMX@TMSP NPs, an initial dose titration experiment was carried out by mixing equal amounts of Zr-PMX@TMSP NPs with different amounts of pGlu-*b*-pSar (**Figure 32**).

Adding 500 µL of NP in HEPES-buffered glucose (HBG) to up to 50 µg of polymer did not notably influence its z-average and PDI but a zeta potential reduction depending on the polymer dose was observed (Figure 32B). Zr-PMX@TMSP NPs without pGlu-*b*-pSar coating exhibited a zeta potential of 28.73 ± 1.55mV, which was reduced to 1.19 ± 0.06 mV by addition of 25 µg pGlu-*b*-pSar.

Further increasing the amount of offered polymer beyond 25 µg did not result in an additional zeta potential reduction, it was therefore concluded that 25 µg pGlu-*b*-pSar was sufficient to induce the observed zeta potential shift toward neutrality, which is known to benefit NPs by reducing unspecific uptake, immune recognition, and prolonging circulation half-lives.[190a, 194]

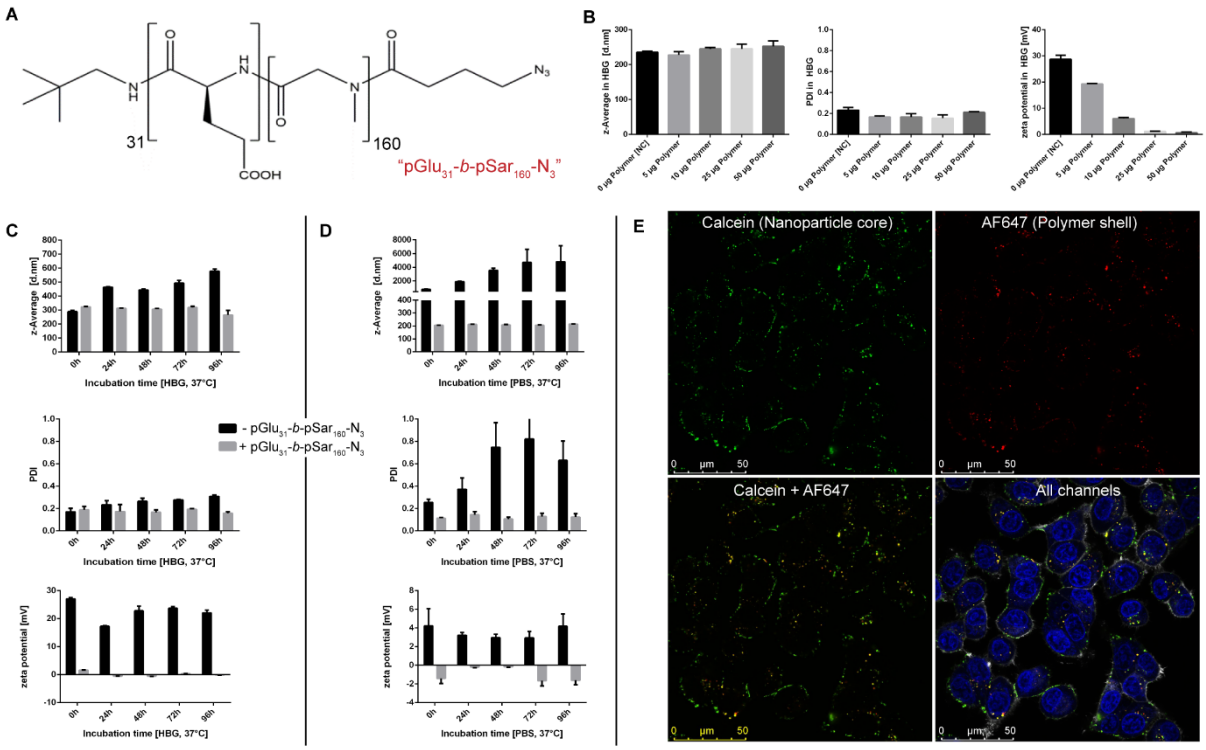

Figure 32 Characterization of the pGlu-pSar coating. A) Structure of $pGlu_{31}$-*b*-$pSar_{160}$-N_3; B) polymer dose titration and the influence on size, PDI, and zeta potential by DLS (mean ± SD, n = 3); C) colloidal long-term stability of Zr-PMX@TMSP NPs (-$pGlu_{31}$-*b*-$pSar_{160}$-N_3) and polymer-coated Zr- PMX@TMSP NPs (+$pGlu_{31}$-*b*-$pSar_{160}$-N_3) in HBG (mean ± SD, n = 3) or (D) PBS (mean ± SD, n = 3) at 37 °C; E) serum stability of the polymer coating visualized by CLSM. Green channel, NP core labeled by coordinative integration of calcein. Red channel, polymer shell labeled with Alexa Fluor 647. Yellow signal in the merged channel indicates co-localization of NP core and polymer shell. "All channels": includes nuclei stained with DAPI (blue) and actin stained with phalloidin-rhodamine (white). CLSM images were recorded by Miriam Höhn (Department of Pharmacy, LMU Munich), $pGlu_{31}$-*b*-pSar-N_3 was synthesized by Tobias Bauer (Institute of Organic Chemistry, Johannes Gutenberg-Universität Mainz).

Next, it was investigated how pGlu-*b*-pSar influenced the colloidal NP stability at 37 °C. Incubating uncoated Zr-PMX@TMSP NPs in HBG (Figure 32C) led to increasing aggregation over time. After 96 h, the z-average almost doubled and a slight increase in PDI was also observed. In contrast, pGlu-*b*-pSar-coated NPs did not increase in size, retained a neutral zeta potential and showed no difference in PDI over 96 h.

The colloidal stability was also evaluated in phosphate-buffered saline (PBS, Figure 32D) which is a relevant biological buffer and challenging due to the strong interaction between phosphate and zirconium ions.[117c, 183, 195] Indeed, the uncoated NPs immediately aggregated to agglomerates in the micrometer range and the sizes further increased over time. In contrast, no increase in size or PDI was observed for the

pGlu-*b*-pSar coated Zr-PMX@TMSP NPs during 96 h of incubation in PBS which illustrated the enormous colloidal stabilization induced by the polymer coating.

It was also investigated if the polymer remained attached to the NP surface under serum-containing cell culture conditions (Figure 26E) since one could expect competition between negatively charged polymer and serum protein for binding to the positively charged silica shell.

The azide-containing pGlu-*b*-pSar block copolymer was therefore labeled with DBCO-Alexafluor647 via strain-promoted alkyne-azide cycloaddition (SPAAC). We then proceeded to incubate calcein-containing Zr-PMX@TMSP NPs coated with pGlu-*b*-pSar-AF647 on KB cells.

After a total of 4 h incubation, confocal microscopy showed yellow signals in the merge channel which indicated co-localization between the calcein integrated into the NP core (green channel) and the AF647-labeled polymer shell (red channel).

Examination of co-localization using the Manders coefficient[196] revealed values of M1 = 0.996 and M2 = 0.684 (channel 1: pGlu-*b*-pSar-AF647, channel 2: calcein). Based on those findings, the polymer seems almost quantitatively colocalized (~99.6%) with the calcein signal (NP core) as illustrated by Manders M1. Manders M2 reveals that approximately 68.4% of the calcein signal are co-localized with the polymer.

It was therefore concluded that the polymer remained attached to the NP surface under serum conditions, especially since almost no isolated red signal representing detached polymer was observed on the merge channel.

3.2.4 Attachment of targeting ligands to the polymer shell enhances the nanoparticle uptake

In order to improve NP uptake and selectivity toward cancer cells, folate targeting, a concept initially developed by Leamon and Low,[197] was introduced to the nanosystem. The folate receptor is known to be overexpressed for many cancer types[198] and the low dissociation constant (Kd approximately 0.1 nM for the α-isoform),[199] makes folate an attractive ligand for selective cancer targeting.[200] A folate-modified block copolymer (pGlu-*b*-pSar-FolA) was synthesized by coupling the azide-containing pGlu-*b*-pSar to a DBCO-folic acid (DBCO-FolA)[151] building block via SPAAC.

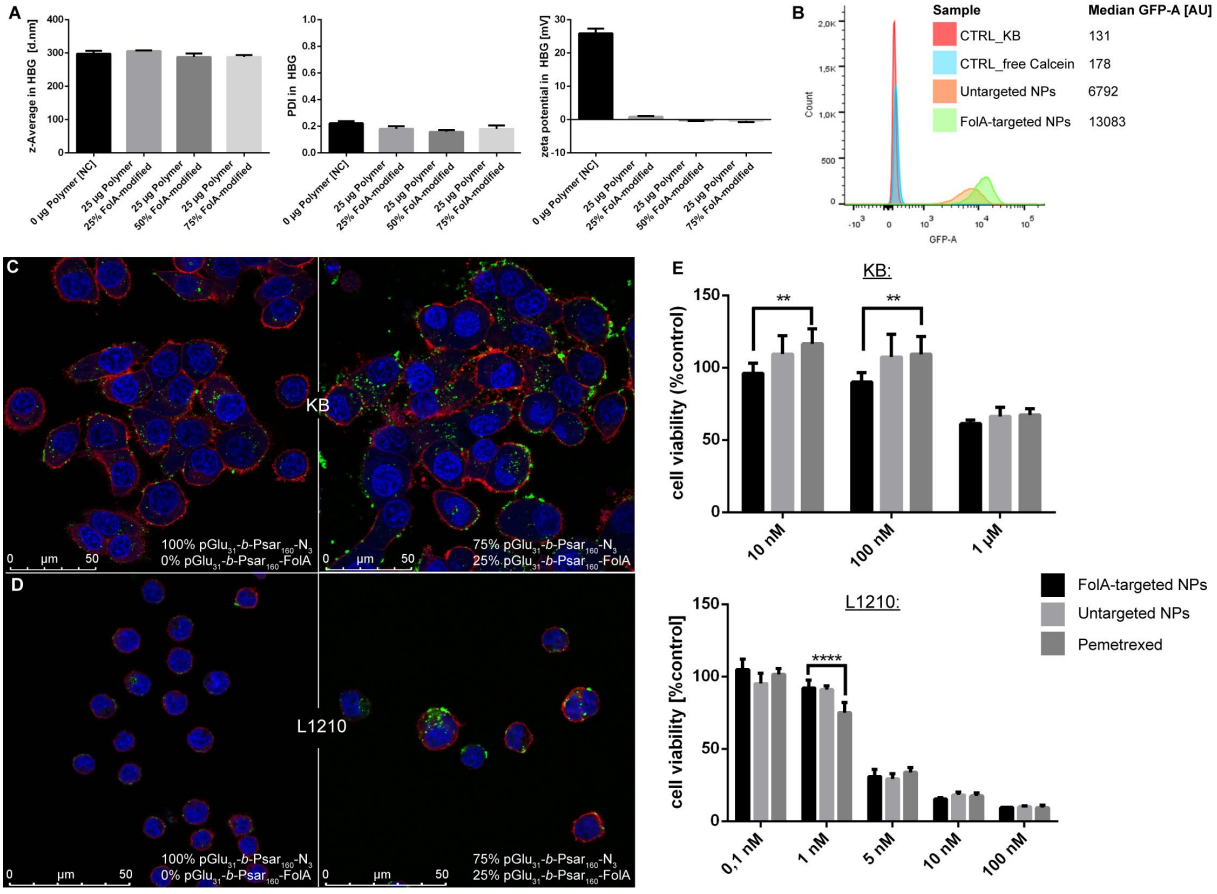

Figure 33 Folate-targeting mediated by coating with pGlu-*b*-pSar-FolA. **A**) Polymer dose titration and influence on size, polydispersity, and zeta potential by DLS (mean ± SD, n = 3); **B**) effects of FolA-targeting on NP uptake by flow cytometry; **C**) evaluation of NP uptake into KB; or (**D**) L1210 cells for FolA-targeted and untargeted NPs by CLSM. Green, NP core labeled by coordinative integration of calcein. Red, actin stained with phalloidin-rhodamine. Blue, nuclei stained with DAPI. **E**) Cell viability studies with KB (top) and L1210 (bottom) by MTT-assay (mean ± SD, n = 5). Cells were treated with NPs or free drug for 1 h, then the medium was changed and the readout took place after 72 h. PMX content of NPs was quantified by HPLC and the dosing adjusted accordingly. Statistical analysis was performed by two-way ANOVA, α = 0.05. CLSM imaging and flow cytometry were conducted by Miriam Höhn, Department of Pharmacy, LMU Munich.

Coating Zr-PMX@TMSP NPs with pGlu-*b*-pSar-FolA as shown in **Figure 33** led to a nanoformulation with folic acid attached to the polysarcosine terminus.

Based on the polymer dose titration experiment shown in Figure 32 which identified 25 µg of polymer as sufficient for surface saturation of the used amount of NPs, it was evaluated by DLS how modifying Zr-PMX@TMSP NPs with 25 µg pGlu-*b*-pSar containing different ratios of pGlu-*b*-pSar-FolA influenced NP size, PDI, and zeta potential (Figure 33A).

Compared to 0% pGlu-*b*-pSar-FolA, a content of up to 75% pGlu-*b*-pSar-FolA did not notably influence any of these parameters. Coating with 100% pGlu-*b*-pSar-FolA led to aggregation, presumably as a result of the high content of hydrophobic ligands and the decreased electrostatic repulsion.[201]

After confirming folate receptor expression by flow cytometry (**Figure 34**), the effect of folate on NP uptake was tested by confocal microscopy using adherent KB (human cervix carcinoma, Figure 33C) and suspension L1210 (mouse lymphocytic leukemia, Figure 33D) cell lines. On both cell lines, an enhanced uptake was observed for the folate-containing nanopharmaceuticals compared to the untargeted formulation.

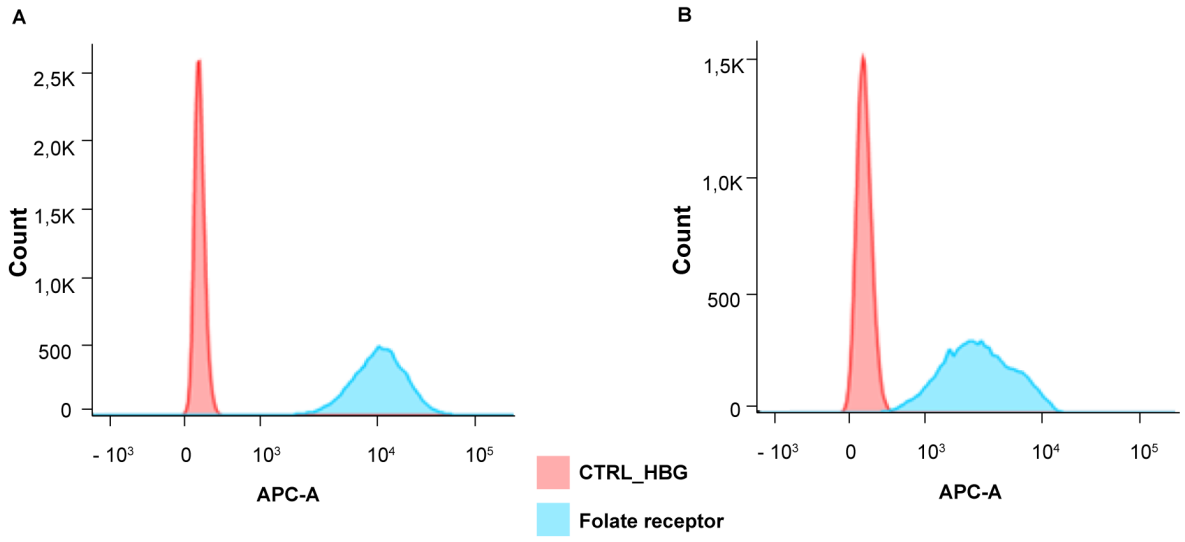

Figure 34 Folate receptor expression levels of **A**) KB and **B**) L1210 cells as determined by flow cytometry. The experiment was performed by Miriam Höhn, Department of Pharmacy, LMU Munich.

Flow cytometry analysis on KB cells (Figure 33B) provided additional confirmation of the increased uptake of folate-targeted NPs compared to an untargeted control formulation coated with pGlu-*b*-pSar only.

A control sample with an equal concentration of free calcein was also analyzed and did not show any uptake. Importantly, this provided additional evidence that the presented coordination NPs can mediate cellular uptake of cargos that do not cross the cell membrane on their own.

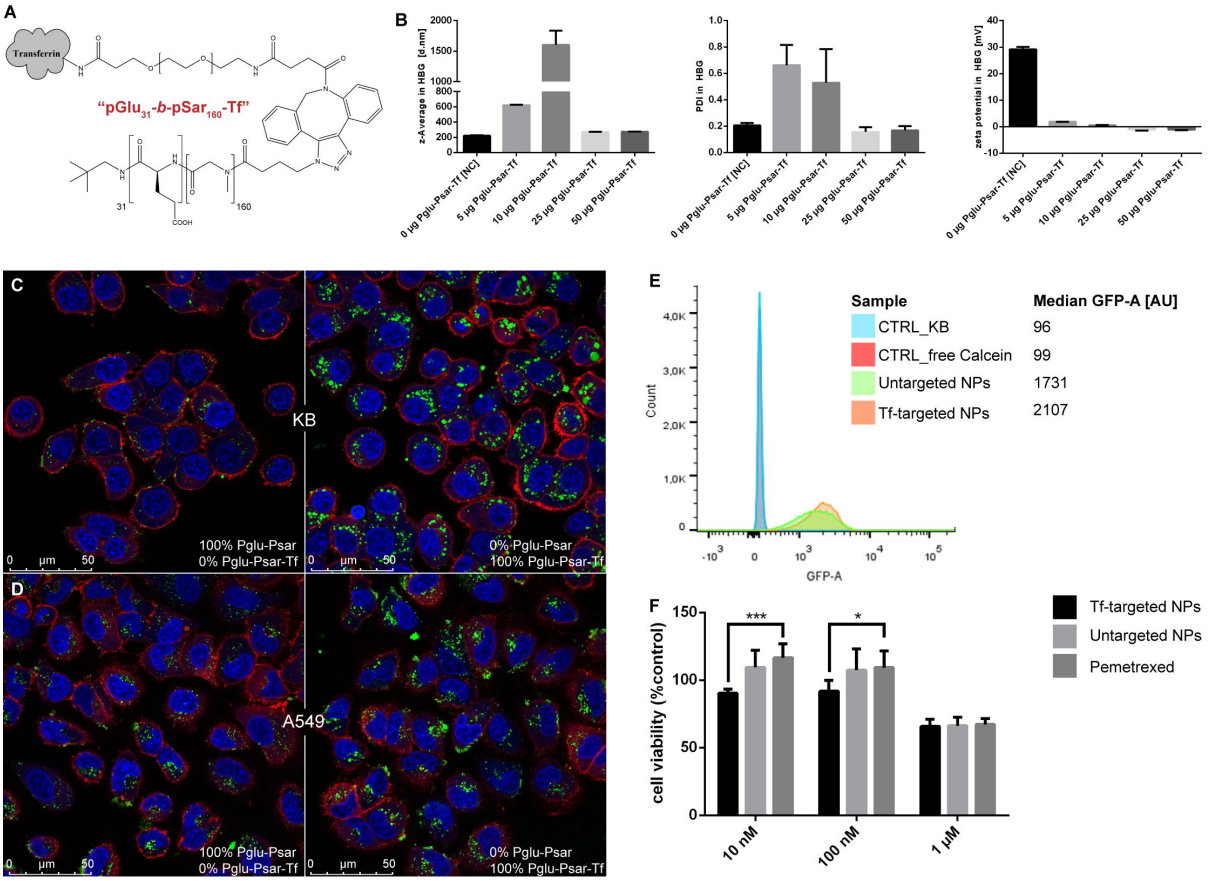

Figure 35 Transferrin targeting mediated by coating with pGlu-*b*-pSar-Tf. **A**) Structure of pGlu-*b*-pSar-Tf; **B**) polymer dose titration and influence on size, polydispersity, and zeta potential by DLS (mean ± SD, n = 3); **C**) evaluation of NP uptake into KB; or (**D**) A549 cells for Tf-targeted and untargeted NPs by CLSM. Green, NP core labeled by coordinative integration of calcein. Red, actin stained with phalloidin rhodamine. Blue, nuclei stained with DAPI. **E**) Effects of Tf-targeting on NP uptake by flow cytometry and **F**) cell viability studies with KB by MTT-assay (mean ± SD, n = 5). Cells were treated with NP or free drug for 1 h, then the medium was changed and the readout took place after 72 h. PMX content of NPs was quantified by HPLC and the dosing adjusted accordingly. Statistical analysis was performed by two-way ANOVA, α = 0.05. CLSM imaging and flow cytometry were performed by Miriam Höhn, Department of Pharmacy, LMU Munich.

A transferrin-functionalized formulation presented in **Figure 35** was also developed since the transferrin receptor is frequently overexpressed by cancer cells and undergoes rapid and efficient internalization upon ligand binding.[202]

Coating Zr-PMX@TMSP NPs with low amounts of 5 µg or 10 µg pGlu-*b*-pSar-Tf (Figure 35A) led to gradual increases in z-average and PDI, but suitable NPs featuring a small z-average, narrow size distribution and neutral zeta potential could be obtained by coating with 25 µg pGlu-*b*-pSar-Tf (Figure 35B).

After confirming transferrin receptor expression levels (**Figure 36**), confocal microscopy uptake experiments with 1 h of incubation revealed a transferrin targeting effect on both KB (Figure 35C) and A549 cells (Figure 35D). For both cell lines, the green calcein signal representing labeled NP cores was more pronounced for Tf-targeted NPs when compared to the untargeted NPs coated with pGlu-*b*-pSar.

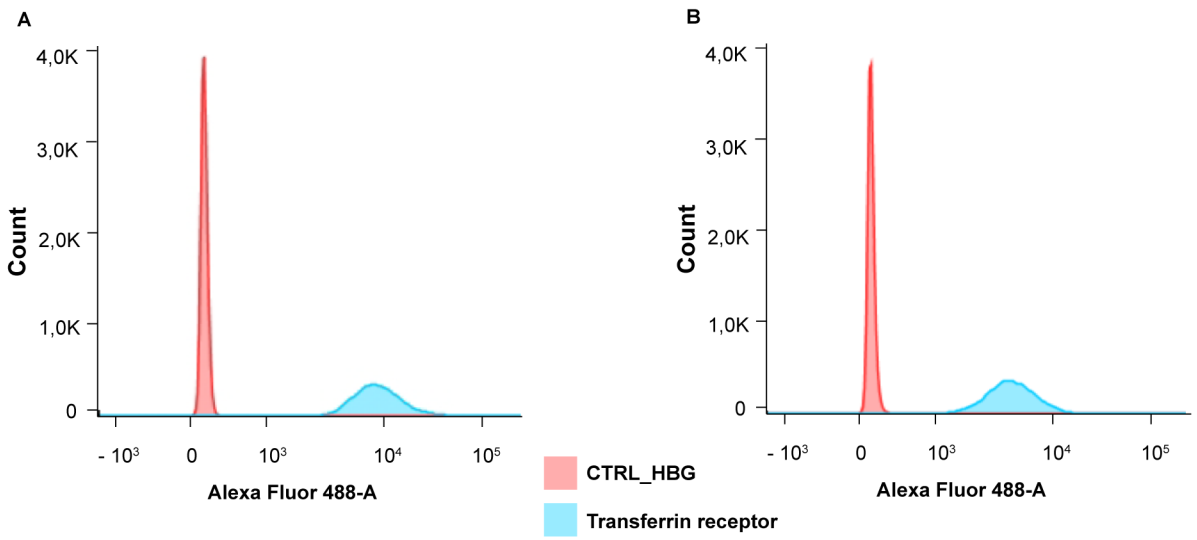

Figure 36 Transferrin receptor expression levels of **A**) KB and **B**) A549 cells by flow cytometry. The experiment was performed by Miriam Höhn, Department of Pharmacy, LMU Munich.

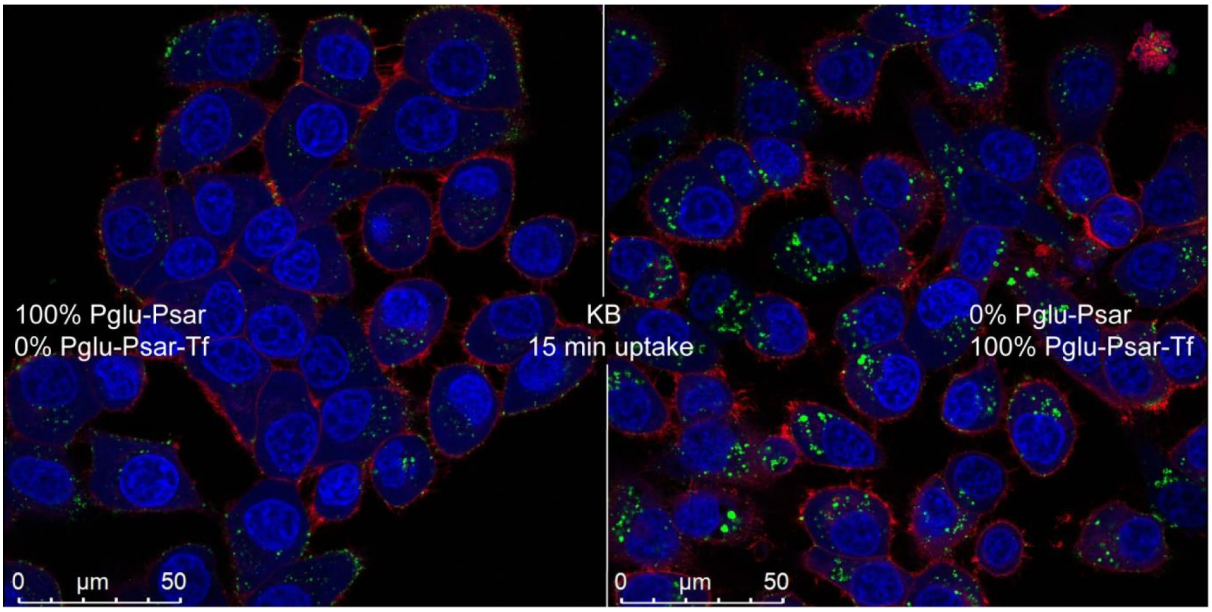

Figure 37 Short-time uptake experiment of untargeted (left) and transferrin-targeted (right) Zr-PMX@TMSP-NPs on KB cells by confocal microscopy. Blue channel: nuclei, red channel: actin cytoskeleton, green channel: calcein integrated into the NP core. After 15 min of NP uptake followed by a wash and an additional 3 h of incubation, enhanced uptake of the Transferrin-targeted NP can be observed. A similar experiment with a longer uptake time of 1 h is depicted in Figure 35. DLS-data of the Tf-targeted formulation is shown in Figure 38B. CLSM imaging was performed by Miriam Höhn, Department of Pharmacy, LMU Munich.

Repeating the confocal microscopy experiment with a reduced incubation time of 15 min in order to elucidate the uptake kinetics (**Figure 37**) led to a similar result although the effect of the transferrin targeting became less prominent due to the shorter NP exposure. Quantitative evaluation by flow cytometry (Figure 35E) also showed a slight shift of the cell population towards higher calcein fluorescence at the early time point.

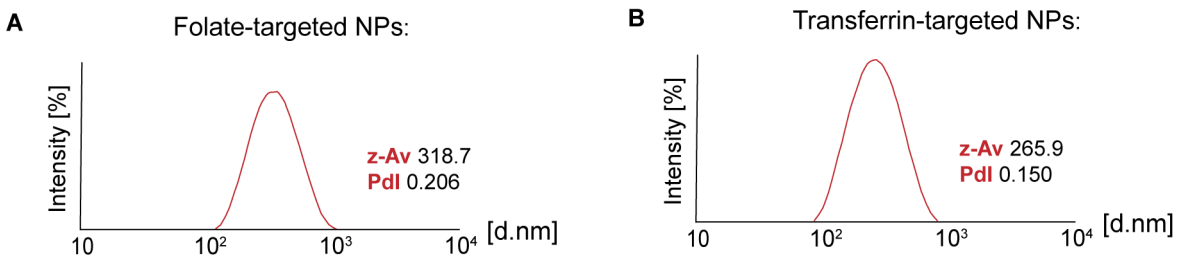

Figure 38 Representative, intensity-based DLS-curves of the formulations used for CLSM, FACS and MTT. **A**) Folate-targeted NPs presented in Figure 33 and **B**) Transferrin-targeted NPs presented in Figures 35 and 37.

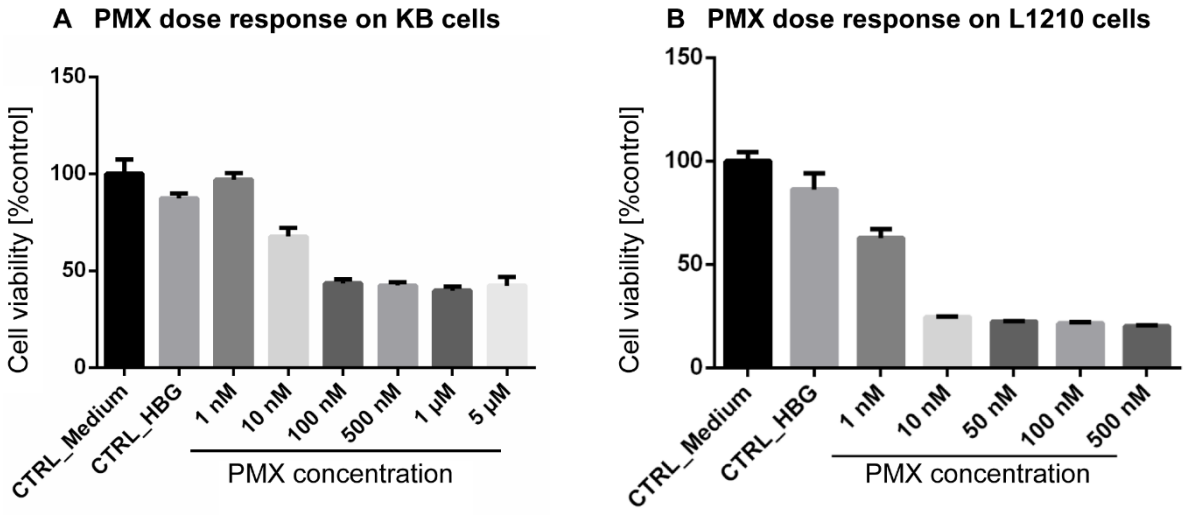

Figure 39 Determination of PMX dose responses using **A**) KB and **B**) L1210 cells. Cells were treated with the indicated PMX concentration and incubated for 72 h. Treatment was performed by Miriam Höhn, Department of Pharmacy, LMU Munich.

The cell killing potential of the targeted NP formulations (folate-targeted: Figure 33, transferrin-targeted: Figure 35, representative DLS data of both formulations: **Figure 38**) was then determined using PMX sensitive L1210 and rather insensitive KB cells. Initially, PMX dose–response (**Figure 39**) and incubation time studies (**Figures 40 and 41**) were performed on both cell lines to define the assay parameters and effective concentration ranges of PMX.

Treatment of KB cells revealed preserved activity of Zr-PMX NPs compared to free PMX and a slight increase in toxicity of folate- and transferrin-targeted formulations after a short exposure time of 1 h (Figures 33E and 35F).

A faster uptake kinetic of the targeted nanoformulations compared to free PMX could be a possible reason for the observation; the absence of different toxicities on KB cells after 72 h of incubation indicates that potential benefits of the targeted nanoformulations can indeed rather be expected at early time points.

Preserved activity of PMX in the nanoformulations was also confirmed for the highly sensitive L1210 cells with 1 h of NP or drug exposure time (Figure 33E). After 72 h, (**Figure 41**) Zr-PMX NPs even mediated an increased toxicity at the low concentration of 1 nM (>60% reduced viability). However, since PMX is a potent cytotoxic drug with high activity on L1210 cells, uptake kinetics do not seem to represent a major limiting factor for this cell line and the advantage of targeted nanoformulations can hardly be assessed under the static cell culture conditions.

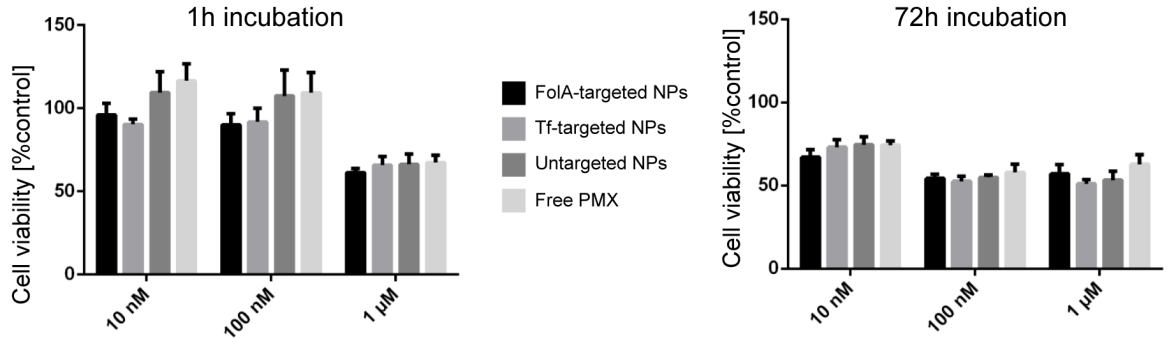

Figure 40 MTT cell viability assay comparing PMX and polymer-coated NP formulations on KB cells. Zr-PMX@TMSP NPs were either coated with pGlu-*b*-pSar-FolA (FolA-targeted), pGlu-*b*-pSar-Tf (Tf-targeted) or pGlu-*b*-pSar-N3 (untargeted) and incubated for 1 h or 72 h. After the indicated incubation time, the medium was changed and the readout was always performed after 72 h. Data from the 1h time point is also shown in Figures 33E and 35E. Treatment was performed by Miriam Höhn, Department of Pharmacy, LMU Munich.

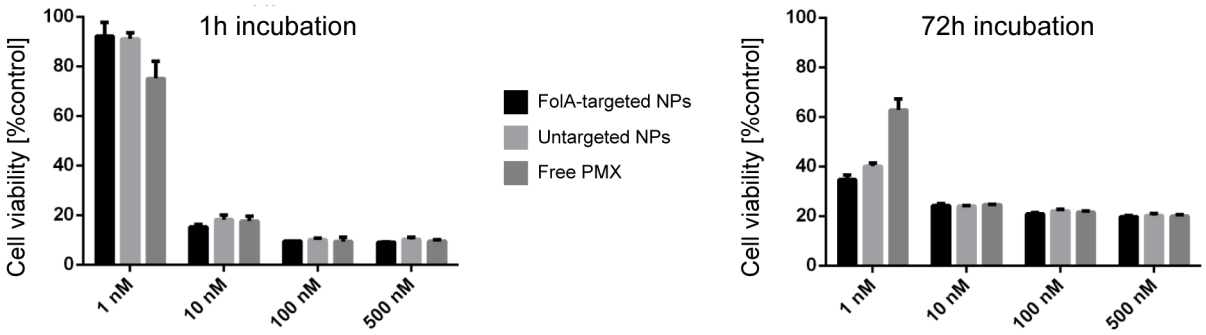

Figure 41 MTT cell viability assay comparing PMX and polymer-coated NP formulations on L1210 cells. Zr-PMX@TMSP NPs were either coated with pGlu-*b*-pSar-FolA (FolA-targeted) or pGlu-*b*-pSar-N_3 (untargeted) and incubated for 1 h or 72 h. After the indicated incubation time, the medium was changed and the readout was always performed after 72 h. A subset of the data from the 1h time point is also shown in Figure 33. Treatment was performed by Miriam Höhn, Department of Pharmacy, LMU Munich.

4 Discussion

4.1 Delivery of chemotherapeutics by metal-organic framework nanoparticles

4.1.1 Screening of a peptide tag library designed for MOF cargo attachment

Evaluation of the tag library identified binding values summarized in **Figure 42**. The following discussion aims at providing an explanation for the observed binding trends. For Zr-*fum*, highest bindings were observed for Glu-based tags. Here, Glu_3 turned out to be the most promising motif; additional negative charge introduced by extending the tag length to Glu_6 seemed to decrease the binding. At pH 7, Zr-*fum* displays a zeta potential of approximately -35 mV[153] in HBG which may account for the reduced Glu_6 binding due to additional electrostatic repulsion. However, it is not clear if the determined approximate halving in binding capacity might be a consequence of the limited number of CUS present on the Zr-*fum* surface. The second highest binding capacity was found for His-based tags. Here, the still low overall binding might result from zirconium, compared to other metals such as copper, only displaying a minor affinity towards coordinative histidine interactions.[203] Additionally, the binding process likely constitutes a balancing act between coordinative and electrostatic interactions. Due to the neutral charge of the His-tag, electrostatic repulsion is not an issue which may provide an explanation why, in contrast to Glu-based tags, binding increased by elongating the His tag. Despite sharing zirconium as the metal component and some structural similarity to Zr-*fum*, UiO-66 displayed a different binding profile. When comparing UiO-66 to Zr-*fum*, Glu_6 behaved almost identically whereas a slightly higher binding capacity was determined for Glu_3.

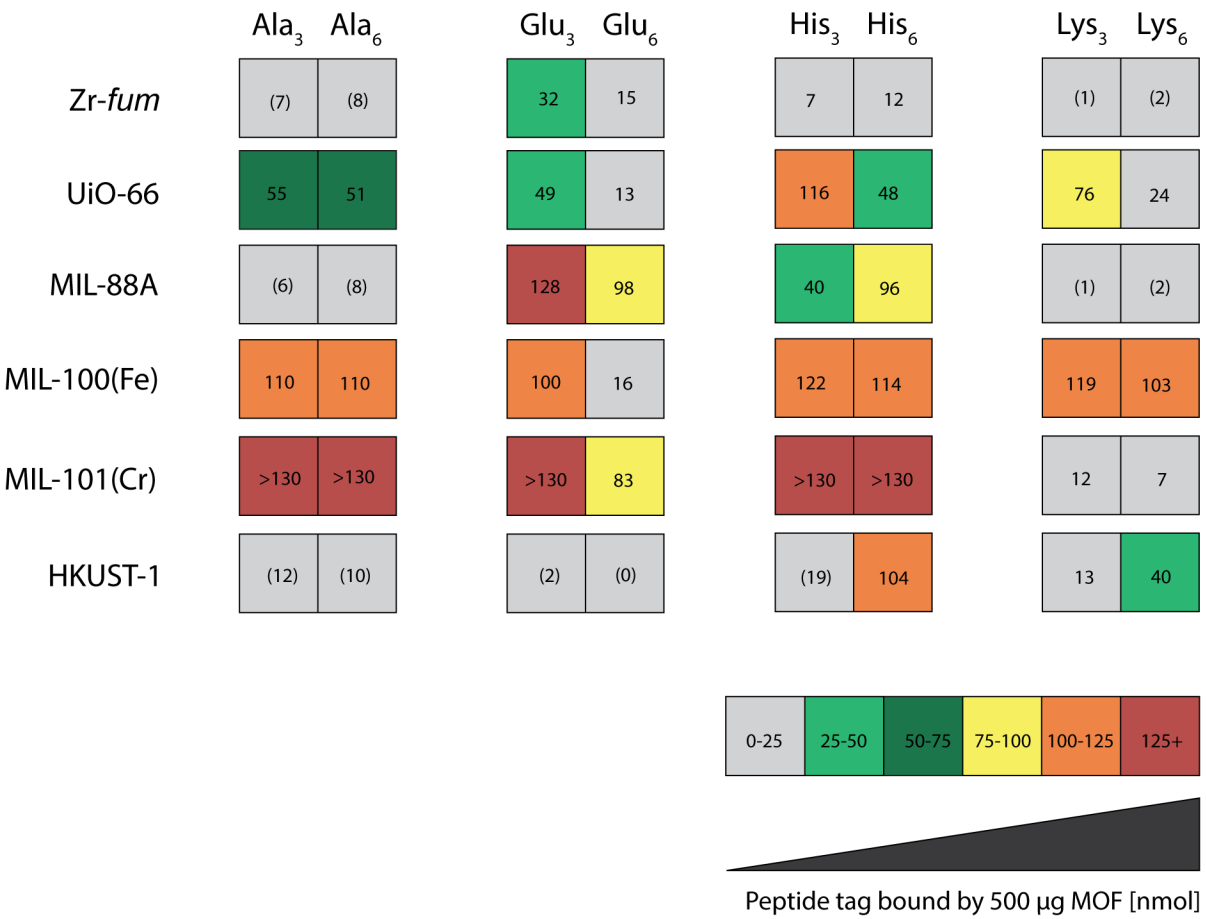

Figure 42 Heat map summary of experimentally determined peptide tag binding capacities. The average binding capacity in nmol observed for 500 µg MOF was rounded to a full number and denoted within the center of each box. A number in brackets indicates the absence of a linear relationship between the amount of offered MOF and the amount of respective peptide tag bound by it as determined by low R^2 values observed for linear regression. Each column represents a tripeptide/hexapeptide tag pair, from left to right: Ala, Glu, His, Lys. Each row depicts one of the screened MOFs, from top to bottom: Zr-based Zr-*fum* and UiO-66, Fe-based MIL-88A and MIL-100(Fe), Cr-based MIL-101(Cr), Cu-based HKUST-1. Boxes were color-coded according to determined tag binding capacities; gray and light green illustrate low (below 50 nmol), dark green and yellow intermediate (50-100 nmol), orange and red high (above 100 nmol) observed binding capacities.

In contrast, pronounced binding of Ala_3 and Ala_6 was only detected for UiO-66. Since UiO-66[204] is more porous compared to Zr-*fum*,[65] the effect might be attributed to passive pore diffusion. Additionally, UiO-66 is synthesized from an aromatic terephthalic acid linker instead of the non-aromatic fumaric acid used to generate Zr-*fum*. Thus, for UiO-66, π-stacking[205] between exposed aromatic linkers situated on the MOF surface and the aromatic acridine moiety which is part of the tag structure might explain the observed binding of neutral Ala tags which do not offer electrostatic interaction potential. However, no Ala_n binding was observed for HKUST-1 which includes aromatic trimesic acid linkers. The higher binding observed for both His_3 and His_6 may point towards a higher number of accessible CUS present on the surface of

UiO-66, although, to the best of my knowledge, no study directly comparing Zr-*fum* and UiO-66 in this regard was conducted so far. At the neutral assay pH, UiO-66 displays a zeta potential of approximately - 25 mV[206] which is about 10 mV lower than that of Zr-*fum* and thus provides a possible explanation for the observed enhanced Lys tag bindings due to elevated electrostatic attractions. For MIL-88A, Glu_3 once again turned out to be the most potent binder. Extending the tag length to Glu_6 entailed a reduction in binding capacity. MIL-88A features a zeta potential of approximately +10 mV.[207] Thus, both electrostatic attraction and the known high affinity of Fe(III) towards oxygen-rich structures[208] contribute to the observed high Glu_3 binding which one could therefore rather expect to increase further with tag length. However, the finite number of available CUS[209] should also be considered. Compared to Glu_3, each individual Glu_6 tag molecule likely occupies more CUS. Additionally, steric and/or electrostatic repulsion between bulkier Glu_6 tag molecules might contribute to the observed reduced binding. In contrast, increasing the His tag length from His_3 to His_6 drastically enhanced the overall binding which seems to contradict the hypothesis of the number of occupied CUS being the decisive factor. For positively charged Lys tags, electrostatic repulsion is likely responsible for the lack of observed binding. Like Zr-*fum*, MIL-88A also utilizes non-aromatic fumaric acid as the linker component and also displays minor porosity. Accordingly, the absence of Ala_n tag binding was also observed for MIL-88A which was to be expected as the combination of Ala_n tag and MIL-88A does not allow for electrostatic attraction, major pore diffusion or π-stacking. Of all evaluated MOFs, MIL-100(Fe) displayed the lowest selectivity. Here, very high binding values were observed for all tags except Glu_6. As MIL-100(Fe) is highly porous[62] and contains aromatic trimesic acid as the linker component,[62] the combination of π-stacking between linkers and tag acridines combined with pore diffusion once again might account for the high binding of Ala_n tags. At neutral assay pH, MIL-100(Fe) shows a zeta potential of approximately -20 mV[169] which might explain why an influence of tag length was only observed for Glu_n tags. Here, elongating the tag from Glu_3 to Glu_6 strongly reduced the binding capacity as a consequence of the higher negative charge density of Glu_6 resulting in enhanced electrostatic repulsion. Notably, observed tag bindings for His_n and Lys_n were quite similar to the values determined for Ala_n which implies that for MIL-100(Fe) and the evaluated tag lengths, both electrostatic attraction (Lys_n tags) and coordinative binding (His_n tags) have little influence on tag binding capacities and that passive pore diffusion and π-stacking appear to be the determining

factors. For the highly porous MIL-101(Cr) which incorporates large pores of 29 and 34 Å,[146] binding capacities exceeding the amount of offered tag were observed multiple times. With the used assay setup, it was therefore not possible to investigate the coordinative His-tag attachment as unspecific pore adsorption already mediated binding of all the offered tag amounts. Looking at binding data for 100 µg MOF where the binding capacity is below the offered tag amount is also not helpful. For His_6, data initially seems to suggest an additional minor coordinative His binding effect. However, due to the standard deviations, no significant difference can be extracted. Additionally, looking at the literature reveals that for Cr^{3+} coordinative interactions may be expected to a bigger extent for oxygen-rich ligands[210] which was also observed here as exemplified by Glu_n tag bindings. Interestingly, the observed trend regarding Glu tag length was the same as for all the other screened MOFs, elongating the tag reduces the observed binding capacity. The highly positive zeta potential of MIL-101(Cr), about +45 mV at neutral pH,[171] results in diminished binding of Lys_n tags. Here, the influence of tag length shows in the data as elongating the tag from Lys_3 to Lys_6 once again reduces the binding due to additionally introduced electrostatic repulsion. For copper-based HKUST-1 which displays pores in the range between 5 and 14 Å[211] and a zeta potential of approximately -12 mV,[172] His_6 was identified as the best binder which is in line with immobilized transition metal ions such as Ni^{2+} [212] or Cu^{2+} [213] being frequently employed to purify hexahistidine-tagged structures in the context of IMAC chromatography.[214] Lys_6 showed the second highest overall binding. For Lys, shortening the tag length to Lys_3 reduced the binding, likely due to reduced electrostatic interaction with the reciprocally charged MOF. It was concluded that no meaningful binding was observed for His_3, Ala_n and Glu_n as no linear relationship between determined binding and offered amount of MOF could be observed as depicted in **Figure 14**.

4.1.2 Delivery of polyglutamylated methotrexate derivatives by attachment to selected metal-organic frameworks

In order to allow for the delivery of pre-polyglutamylated MTX derivatives, MOF binding capacities were determined in a first step.

Per 500 µg Zr-*fum*, initial photometric evaluation of E_3-based structures determined bindings of 31.11 ± 2.92 nmol, 44.65 ± 1.04 nmol and 31.6 ± 4.9 nmol (E_2-MTX, E_2-FolA and E_3-Acridin). For E_6-based structures, bindings of 16.6 ± 0.71 nmol, 10.57 ± 4.03 nmol and 14.7 ± 1.2 nmol (E_5-MTX, E_5-FolA and E_6-Acridin) were achieved per 500 µg Zr-*fum*.

Per 500 µg MIL-88A, E_3-based bindings of 111.05 ± 1.80 nmol, 94.96 ± 1.70 nmol and 128.4 ± 0.25 nmol (E_2-MTX, E_2-FolA and E_3-Acridin). For E_6-based structures, bindings of 76.7 ± 4.07 nmol, 68.68 ± 1.54 nmol and 98.5 ± 10.2 nmol (E_5-MTX, E_5-FolA and E_6-Acridin) were achieved per 500 µg MIL-88A.

Interestingly, apart from the slightly higher than expected E_2-FolA binding observed on Zr-*fum*, the determined E_n-MTX and E_n-FolA binding capacities are very similar to the respective E_n-Acridin tag bindings observed during the tag screening which further confirms that the E_n motif is indeed responsible for cargo attachment since the remaining structure differed. Whereas the E_n tags contained a short PEG spacer (STOTDA) and a tricyclic aromatic acridine moiety, no such features were present for E_n-MTX or E_n-FolA.

E_n-MTX attachment was further confirmed by zeta potential where the number of glutamates had a striking influence. On Zr-*fum* in HBG (36.8 ± 0.9 mV), both attachment of E_2-MTX (- 7.35 ± 0.15 mV) and E_5-MTX (- 31.7 ± 1.0 mV) mediated zeta potential inversion. Evaluation of MIL-88A in HBG (24.6 ± 1.5 mV) revealed the same trend with observed values of 14.8 ± 0.3 mV (E_2-MTX@MIL-88A) and 3.14 ± 0.25 mV (E_5-MTX@MIL-88A).

Testing the formulations *in vitro* using KB human cervix carcinoma or L1210 mouse lymphocytic leukemia cell lines revealed beneficial effects of MOF-based delivery for the KB cell line where reductions in EC_{50} values were observed. Here, respective EC_{50} values of 4.237 nM (MTX), 4.438 nM (E_2-MTX), 9.883 (E_5-MTX), 1.451 nM (E_2-MTX@Zr-*fum*) and 3.757 nM (E_5-MTX@Zr-*fum*) were calculated. Using MIL-88A, a minor increase in EC_{50} was observed between E_2-MTX (4.438 nM) and E_2-MTX@MIL-88A (4.890 nM) whereas delivery of E_5-MTX by MIL-88A very slightly reduced the EC_{50} (9.755 nM) compared to free E_5-MTX (9.883 nM). However, it is not clear why E_2-MTX@MIL-88A was found to be less potent compared to E_2-MTX@Zr-*fum*. Both reduced particle uptake or unsatisfactory E_2-MTX release might be responsible.

On L1210, treatment with E_5-MTX within the tested concentration range had no influence on cell viabilities and could therefore not be evaluated. Additionally, no MOF effect was observed as treatment with free MTX (0.568 nM) or E_2-MTX (2.120 nM) was more potent than either E_2-MTX@Zr-*fum* (4.411 nM) or E_2-MTX@MIL-88A (7.568 nM).

As free MTX is already highly potent on L1210 as reflected by the picomolar EC_{50}, potentially enhanced uptake by nanoparticular delivery does not seem to have a major effect on the achievable cell killing.

However, the good results obtained on rather resistant KB cells (MTX EC_{50} of 4.237 nM) might be related to the delivery of pre-polyglutamylated MTX which constitutes the active species and is more potent upon reaching the cytosol.

In order to reveal if the observed increase in potency is related to polyglutamylation status or uptake kinetics, a follow-up experiment using another porous MOF to deliver native MTX could be conducted. If enhanced uptake was the decisive factor, one would expect to observe the same effect here independent of pre-polyglutamylation.

4.2 Core-shell functionalized zirconium-pemetrexed coordination nanoparticles as carriers with a high drug content

This chapter was partially adapted from the following references:

B. Steinborn, P. Hirschle, M. Höhn, T. Bauer, M. Barz, S. Wuttke, E. Wagner, U. Lächelt. *Core-Shell Functionalized Zirconium-Pemetrexed Coordination Nanoparticles as Carriers with a High Drug Content*. Advanced Therapeutics **2019**, 2, 1900120.

B. Steinborn, U. Lächelt. *Metal-Organic Nanopharmaceuticals*. Pharmaceutical Nanotechnology **2020,** Manuscript accepted.

Coordinative interactions between multivalent metal ions and drug derivatives with Lewis base functions give rise to NCPs as delivery systems. As pharmacologically active agents are used as a main building block of the nanomaterial, very high drug loadings have been observed.[117a, 117b, 119a, 119b] By additionally selecting metal ions with favorable pharmacological or physicochemical properties, such as mediating imaging contrast[215] or radiosensitization[122], the obtained NCPs are predominantly composed of active components.

The assembly of drug molecules into NCPs also modulates their pharmacokinetics, combines pharmacological drug action with specific characteristics of metal components, allows for spatiotemporal co-delivery and provides a strategy to generate tailorable multifunctional nanoparticles with a wide range of possible biomedical applications.

A huge variety of suitable pharmaceutical building blocks combined with appropriate metal ions allows for innovative therapeutic and diagnostic nanosystems with clinical potential as illustrated by encouraging *in vivo* studies.

Thus, NCPs and MOFs currently receive a high research interest and numerous studies evaluated their feasibility for chemotherapeutic applications such as the delivery of platinum derivatives,[106b, 106d, 112, 119, 122] doxorubicin[109-111, 117a, 118, 216] or PDT[75, 99, 108a, 120] approaches.

Within this thesis, a novel approach for the assembly and subsequent core-shell functionalization of a chemotherapeutic drug carrier with a very high loading capacity, tunable stabilization against serum, surface shielding and the option for receptor targeting was presented.

The drug-containing core consists of PMX and Zr ions which assemble into nanocolloids via Lewis acid–base interactions. Here, the metal to drug stoichiometry turned out to be decisive, whereas particles could be obtained with an excess of PMX, no particle assembly was observed by increasing the amount of zirconium beyond 1:1. A possible reason may lie within a higher number of initially formed crystal nuclei which results in the NP growth being distributed over more individual particles thus leading to slower growth of single particles as described by Wang *et al.*[178]

Acidification during the synthesis also had to be controlled carefully. Without any acid, rapid clouding and immediate bulk formation occurred whereas too much acid strongly reduced the amount of obtained nanomaterial, likely due to increased protonation of PMX reducing its electrostatic interaction potential with zirconium and thus slowing the particle growth.

After synthesis, a sonication step was found to be necessary in order to disaggregate agglomerates generated during centrifugation and washing steps. Here, a duration of 5 minutes was sufficient. The developed synthetic protocol also displayed some flexibility with regard to the cargo that may be encapsulated as illustrated by calcein. Here, the addition of 5 % calcein did not notably affect the particle size and polydispersity and allowed for direct imaging of the NP without the need for additional labeling. Due to its charge, free calcein does not cross the cellular membrane. Importantly, the calcein signal observed by CLSM and flow cytometry thereby confirms that the NP is indeed able to mediate cellular uptake of an otherwise impermeable cargo.

Subsequent physicochemical characterization of the NP core revealed spherical, monodisperse particles. The absence of crystallinity suggests that the likely mesoporous Zr-PMX NPs can rather be classified as amorphous nanoscale coordination polymers than MOFs.

Strikingly, combined analysis by HPLC and ICP-AES revealed a very high NP core drug content of about 80% (m/m) which also corresponds approximately to the feed ratio during synthesis. As PMX displays a high binding affinity toward serum protein, uncoated NP cores disassembled rapidly in a serum-containing environment and required a thin silica shell for stabilization and simultaneous control of drug release. To generate the shell, TMSP was chosen due to its diethylenetriamine motif which provided direct interaction sites for coordinative and/or electrostatic attachment to the NCP surface. To the best of my knowledge, this is the first time that TMSP was used in a drug delivery setting.

For the coating process, time was identified as a decisive parameter. Whereas up to 5 h of reaction time still resulted in particles in the nano range, increasing the duration to 24 h led to bulk formation. The silica coating also mediated a zeta potential inversion, enhanced the NP uptake, but increased extracellular aggregation on multiple cell lines. The achieved stabilizing effect against serum depended on the used amount of TMSP which seems likely since one would expect that using more TMSP leads to a thicker silica shell.

Interestingly, this observation hints at the possibility of tuning the drug release kinetics of the developed NCP core by controlling the silica shell formation. For the used TMSP amount, SEM imaging indicated a shell thickness of about 5 nm. As PMX mediates its activity in a solubilized state, the achieved stabilization was considered to represent a suitable balance between required stability and lability.

In order to address the observed tendency for aggregation in a biological environment which initially offset the beneficial stabilizing and uptake-enhancing effects of the silica coating, a $pGlu_{31}$-*b*-$pSar_{160}$-N_3 block-copolymer was implemented as the outermost layer of the delivery system. It mediated surface shielding as reflected by neutral zeta potentials which were observed for the polymer-coated formulations.

The polymer coating also resulted in highly efficient colloidal stabilization observed in HBG, PBS but also under cell culture conditions which is evident by comparing images of formulations coated with the block-copolymer or TMSP only.

Attaching an additional fluorescence label to the polymer layer and evaluating its co-localization with the calcein signal using the Manders coefficient[196] revealed that the polymer mainly remained attached to the particle surface under serum conditions.

Moreover, the incorporated azides enabled modification with uptake-enhancing receptor ligands by click chemistry as shown for folate and transferrin and open up great flexibility towards the introduction of other functionalities. Both flow cytometry and CLSM revealed enhanced uptake of the targeted formulations.

In vitro evaluations confirmed the maintained pharmacological activity of PMX on KB human cervix carcinoma and L1210 mouse lymphocytic leukemia cells and the cellular uptake of otherwise impermeable co-encapsulated calcein.

The presented concept is considered to be exemplary of an envisioned ‘minimalist design’ of a nanopharmaceutical translatable to other suitable APIs. It features a very high drug-to-carrier material ratio meant to potentially minimize patient exposure to inactive nanocarrier material.

5 Summary

Metal-organic nanosystems such as metal-organic frameworks (MOFs) and nanoscale coordination polymers (NCPs) are highly attractive materials for a range of biomedical applications as exemplified by drug delivery,[42a, 102] imaging[49a, 100, 217] or photodynamic therapy.[75, 99, 108a, 120a] By directly utilizing active pharmaceutical ingredients (APIs) as linker molecules,[75, 99, 106b-d, 119c, 218] very high drug contents and spatiotemporal co-delivery may be realized. Additionally, multiple studies already illustrated potential biocompatibilities and encouraging chemotherapeutic *in vivo* results[75, 99, 106d, 112, 119c, 218] have already been reported.

Within the first part of this thesis, novel peptide sequences that allow for MOF cargo attachment were screened, identified and subsequently utilized for the delivery of polyglutamylated methotrexate (MTX). MOF drug loading may be achieved using different strategies, yet little is known on how the structure of the cargo influences the binding capacities. Thus, novel peptide-based anchoring motifs were screened on multiple MOFs. For Zr-*fum* and MIL-88A, the highest bindings were observed for the Glu_3 tag. For UiO-66 and MIL-100(Fe), His_3 was the most prominent binder. Of all screened MOFs, MIL-101(Cr) displayed the highest overall binding capacities. For microporous HKUST-1, the highest capacity was witnessed for His_6. To the best of my knowledge, no systematic screening of peptide-based MOF anchoring motifs has been conducted previously and just one similar study utilizing His-tags comes to mind.[96] Thus, this thesis identified novel peptide motifs able to confer pronounced MOF binding capacities.

As Zr-*fum* and MIL-88A are both perceived as suitable for biomedical applications, an exemplary application of the glutamate motif was pursued by using it to attach pre-polyglutamylated MTX which was simultaneously aimed at potentially addressing MTX resistance. For both Zr-*fum* and MIL-88A, Glu_n-MTX functionalization led to a significant reduction in zeta potential depending on the number of glutamates within the tag and additionally improved particle sizes and polydispersities. The potency of Glu_n-MTX@MOF was then evaluated on adherent human cervix carcinoma KB and suspension mouse lymphocytic leukemia cells lines. On KB, especially attachment of Glu_2-MTX to Zr-*fum* seemed to enhance its respective potency as determined by EC_{50}

values (Glu_2-MTX: 4.438 nM, Glu_2-MTX@Zr-*fum*: 1.451 nM, Glu_5-MTX: 9.883 nM, Glu_5-MTX@Zr-*fum:* 3.757 nM, MTX: 4.237 nM). Here, both Glu_2-MTX@Zr-*fum* and Glu_5-MTX@Zr-*fum* seem more potent than free MTX. Delivery by MIL-88A was found to be less effective. For the L1210 cell line, MOF attachment did not result in reduced EC_{50} values.

The second part of this thesis proceeded to explore the design of a minimalistic, 'carrier-free' chemotherapeutic drug delivery system that features a very high material economy. First, a novel NCP core was created by assembling PMX and zirconium ions into a coordinative nanoparticle using Lewis acid–base interactions. Since PMX itself comprises the primary building block of the NCP, the amorphous and likely mesoporous particle core could be obtained with an exceptionally high drug content of almost 80 % (weight/weight). Due to the labile nature of the linkage, NCPs typically display low serum stabilities which was also observed for the nanosystem developed here. Therefore, further functionalization with a thin silica shell was implemented in order control the particle stability. Instead of frequently used TEOS, TMSP was chosen as its diethylenetriamine motif provided direct interaction sites for coordinative and/or electrostatic surface attachment to the NCP surface. To the best of my knowledge, this is the first time that TMSP was used in a drug delivery setting. The obtained silica shell with a thickness of about 5 nm enhanced the serum stability and NP uptake, but promoted extracellular aggregation. The NCP was therefore further functionalized with a pGlu-*b*-pSar-N_3 block-copolymer which dramatically increased colloidal stabilities. Additionally, due to the terminal azide, it also allowed for modification with uptake-enhancing receptor ligands introduced by click chemistry. Such a targeting capacity was exemplified by folate and transferrin. Especially on KB cells, CLSM indicated strongly enhanced uptake of transferrin-targeted formulations. *In vitro* potencies of the formulations were then evaluated on KB cervix carcinoma and L1210 mouse lymphocytic leukemia cell lines. On KB, both transferrin- and folate-targeting led to a slightly enhanced potency compared to free PMX. Notably, cellular uptake of otherwise impermeable co-encapsulated calcein was observed and illustrates a certain flexibility with regard to the cargo that may be delivered utilizing the developed NCP. In sum, the presented NCP formulation is regarded exemplary for an envisioned 'minimalist design' of a nanopharmaceutical with a favorable multifunctional efficiency[113] based on the high drug-to-carrier material ratio.

6 Appendix

6.1 Abbreviations

ABC	Adenosine triphosphate binding cassette
ACN	Acetonitrile
ADC	Antibody drug conjugate
API	Active pharmaceutical ingredient
ATP	Adenosine triphosphate
Bix	1,4-bis(imidazol-1-ylmethyl)benzene
Boc	*tert*-Butoxycarbonyl protecting group
Ce6	Chlorin E6
CUS	Coordinatively unsaturated metal site
DAD	Diode array detector
DBCO	Dibenzocyclooctyne
DCM	Dichloromethane
DHFR	Dihydrofolate reductase
DIPEA	*N,N*-Diisopropylethylamine
DLS	Dynamic light scattering
DMEM	Dulbecco's modified Eagle's medium
DMF	*N,N*-Dimethylformamide
DNA	Desoxyribonucleic acid
DOX	Doxorubicin
EDTA	Ethylendiaminetetraacetic acid
E_n-MTX	Polyglutamylated MTX derivative containing n additional glutamates
EPR	Enhanced permeability and retention
FBS	Fetal bovine serum
FDA	U. S. Food and Drug Administration
Fmoc	Fluorenylmethoxycarbonyl protecting group
FolA	Folic acid
FR	Folate receptor
H_2BDC	Benzenedicarboxylic acid
H_2BTC	Benzenetricarboxylic acid
H_2DBP	5,15-di(*p*-benzoato)porphyrin
HBG	Hepes-buffered glucose
HBTU	2-(1H-benzotriazole-1-yl)-1,1,3,3-tetramethyluronium hexafluorophosphate
HEPES	*N*-(2-hydroxethyl) piperazine-N'-(2-ethansulfonic acid)
HOBt	1-Hydroxybenzotriazole
HKUST	Hong Kong University of Science and Technology
HPLC	High Performance Liquid Chromatography
ICP-AES	Inductively coupled plasma atomic emission spectroscopy
IMAC	Immobilized metal ion affinity chromatography
i.v.	intravenous

MDR	Multidrug resistance
MIL	Materials institute Lavoisier
mM	Millimolar
MRI	Magnetic Resonance Imaging
MTBE	Methyl *tert*-butyl ether
MTT	3-(4,5-dimethylthiazol-2-yl)-2,5-diphenyltetrazolium bromide
mV	Millivolt
MOF	Metal-organic framework
MTX	Methotrexate
MWCO	Molecular weight cut-off
NCP	Nanoscale coordination polymer
NHS	*N*-Hydroxysuccinimide
nm	Nanometer
nM	Nanomolar
NMP	*N*-Methyl-2-pyrrolidone
NP	Nanoparticle
PDI	Polydispersity index
PDT	Photodynamic therapy
PEG	Polyethylene glycol
pM	picomolar
PMX	Pemetrexed
PyBOP	Benzotriazol-1-yloxy-tripyrrolidinophosphonium hexafluorophosphate
RFC	Reduced Folate Carrier
RNA	Ribonucleic acid
RP-HPLC	Reversed-phase high performance liquid chromatography
RT	Room temperature
SBU	Secondary building unit
SEC	Size-exclusion chromatography
SEM	Scanning electron microscopy
siRNA	Small interfering RNA
SPAAC	Strain-promoted alkyne-azide cycloaddition
SPS	Solid-phase synthesis
STOTDA	N-Fmoc-N″-succinyl-4,7,10-trioxa-1,13-tridecanediamine
TFA	Trifluoroacetic acid
TIS	Triisopropylsilane
TMSP	N^1-(3 trimethoxysilylpropyl)diethylenetriamine
UiO	Universitetet I Oslo
µM	Micromolar

6.2 Summary of synthesized structures

Table 11 Summary of SPS derived structures

Name	Purpose	Structure (C to N)	Chapter
Ala_3	Tag screening	HOOC-Ala-Ala-Ala-STOTDA-acridine	3.1.1.
Ala_6	Tag screening	HOOC-Ala-Ala-Ala-Ala-Ala-Ala-STOTDA-acridine	3.1.1.
Glu_3	Tag screening	HOOC-Glu-Glu-Glu-STOTDA-acridine	3.1.1.
Glu_6	Tag screening	HOOC-Glu-Glu-Glu-Glu-Glu-Glu-STOTDA-acridine	3.1.1.
His_3	Tag screening	HOOC-His-His-His-STOTDA-acridine	3.1.1.
His_6	Tag screening	HOOC-His-His-His-His-His-His-STOTDA-acridine	3.1.1.
Lys_3	Tag screening	HOOC-Lys-Lys-Lys-STOTDA-acridine	3.1.1.
Lys_6	Tag screening	HOOC-Lys-Lys-Lys-Lys-Lys-Lys-STOTDA-acridine	3.1.1.
E_2-FolA	Control structure	HOOC-Glu-Glu-Glu-Pteroic acid	3.1.2.
E_5-FolA	Control structure	HOOC-Glu-Glu-Glu-Glu-Glu-Glu-Pteroic acid	3.1.2.
E_2-MTX	Chemo delivery	HOOC-Glu-Glu-Glu-4-[N-(2,4-Diamino-6-pteridinylmethyl)-N-methylamino]benzoic acid	3.1.2.
E_5-MTX	Chemo delivery	HOOC-Glu-Glu-Glu-Glu-Glu-Glu-4-[N-(2,4-Diamino-6-pteridinylmethyl)-N-methylamino]benzoic acid	3.1.2.

6.3 Analytical Data

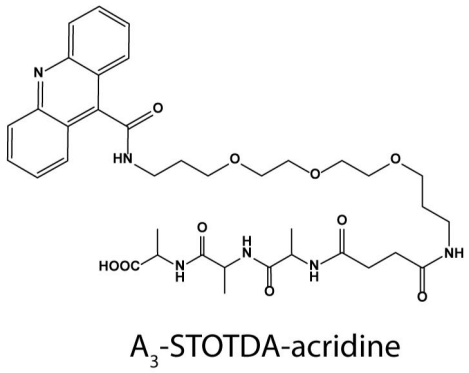

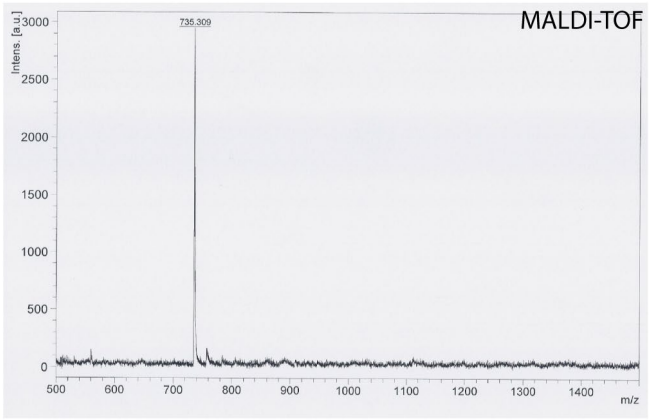

A_3-STOTDA-acridine. MALDI-TOF: $[M+H]^+$ calc. 739.4, $[M+H]^+$ found 735.3

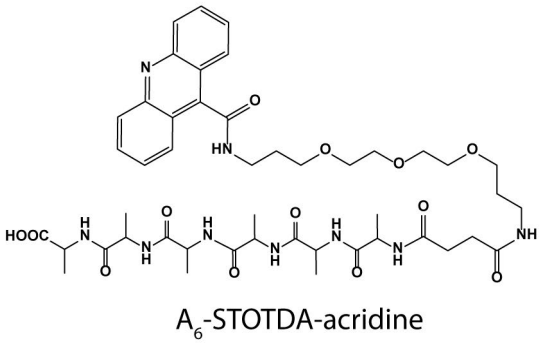

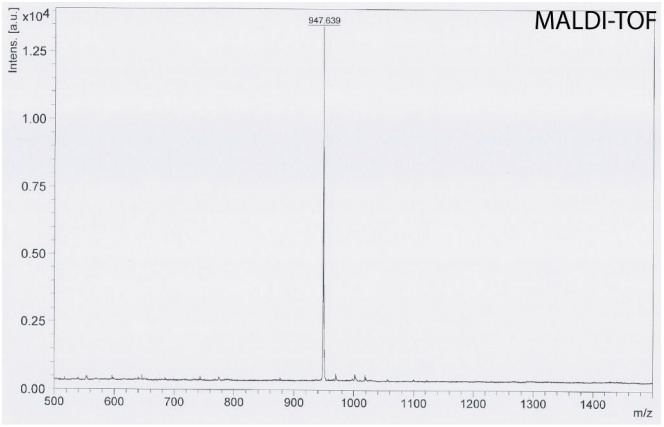

A_6-STOTDA-acridine. MALDI-TOF: $[M+H]^+$ calc. 951.5, $[M+H]^+$ found 947.6

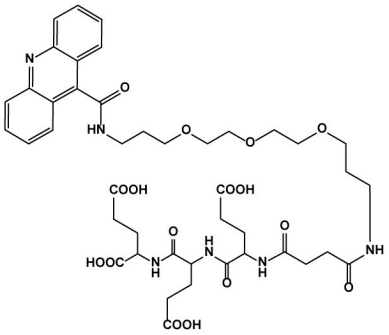

E_3-STOTDA-acridine

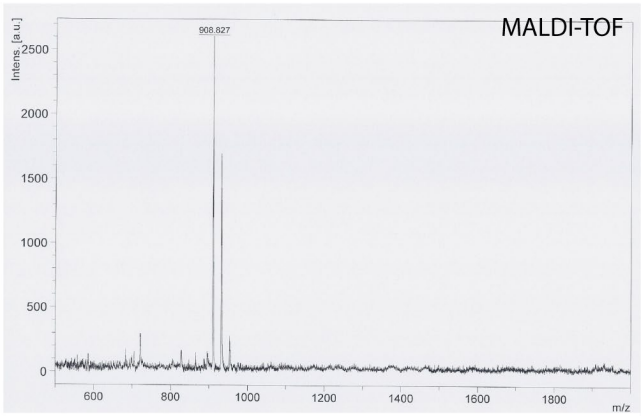

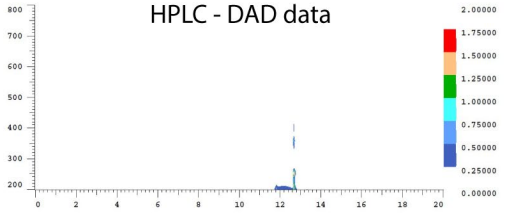

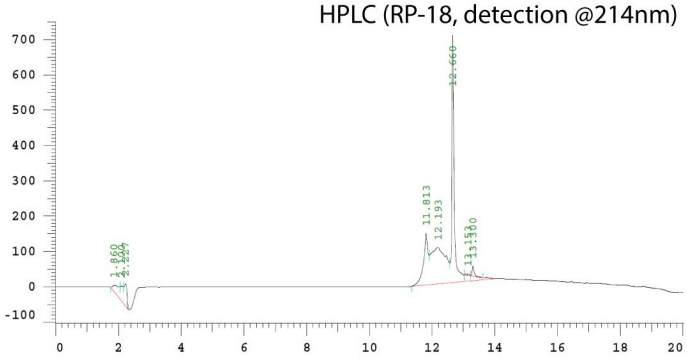

E_3-STOTDA-acridine. MALDI-TOF: $[M+H]^+$ calc. 913.4, $[M+H]^+$ found 908.8 and 930.8 $[M+Na]^+$. RP-18 HPLC: peak@12.66 min.

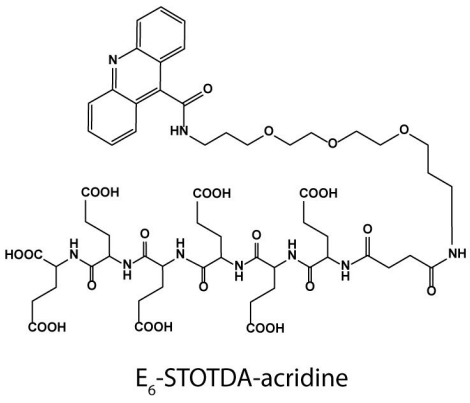

E_6-STOTDA-acridine

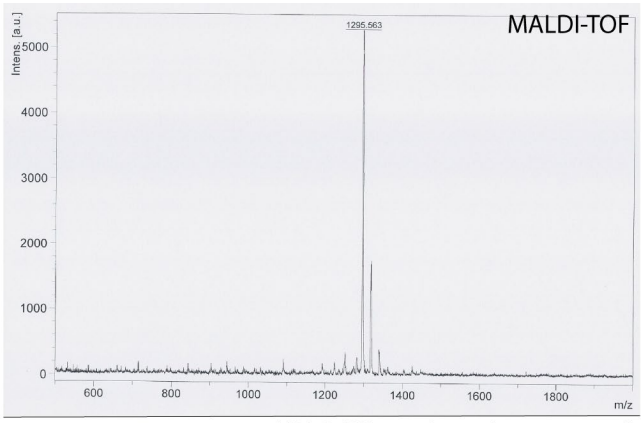

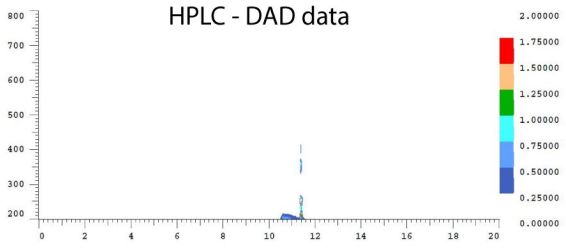

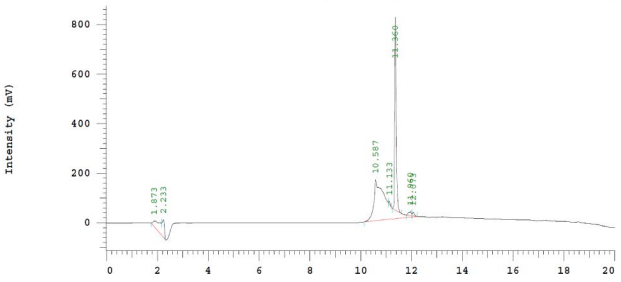

E_6-STOTDA-acridine. MALDI-TOF: $[M+H]^+$ calc. 1300.5, $[M+H]^+$ found 1295.6 and 1317.5 $[M+Na]^+$. RP-18 HPLC: peak@11.36 min.

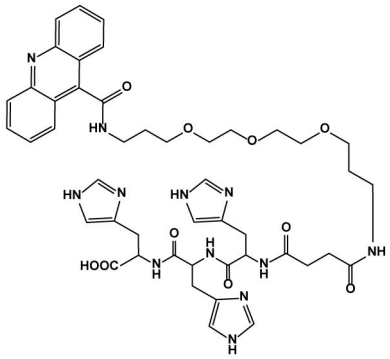

H_3-STOTDA-acridine

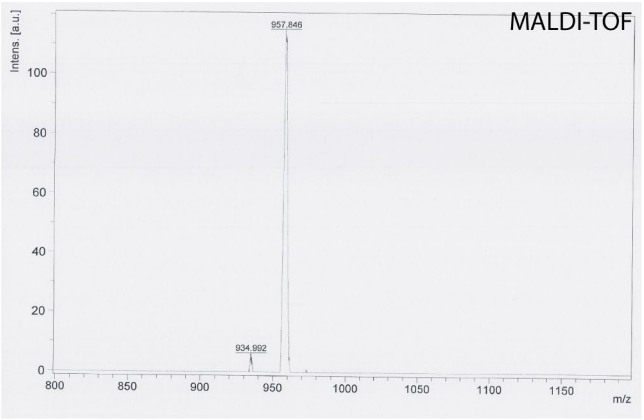

H_3-STOTDA-acridine. MALDI-TOF: $[M+H]^+$ calc. 937,4 $[M+H]^+$ found 935 and 957.8 $[M+Na]^+$.

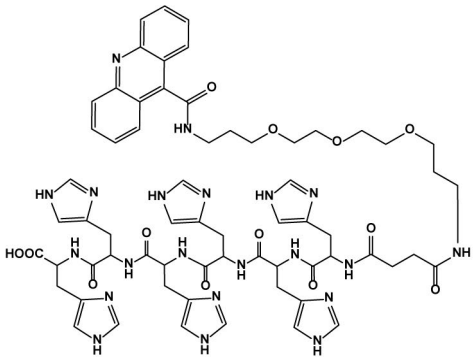

H_6-STOTDA-acridine

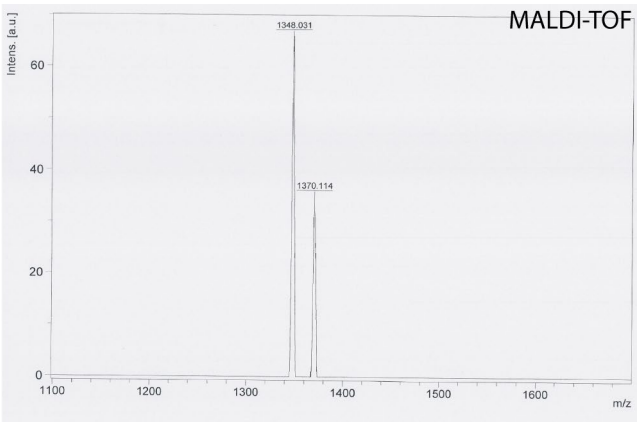

H_6-STOTDA-acridine. MALDI-TOF: $[M+H]^+$ calc. 1348.6 $[M+H]^+$ found 1348 and 1370.1 $[M+Na]^+$.

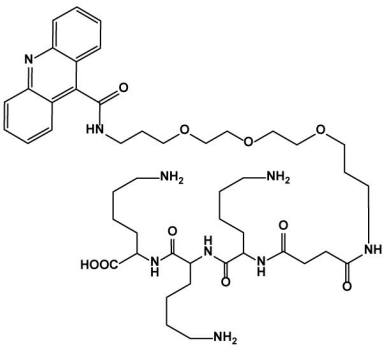

K_3-STOTDA-acridine

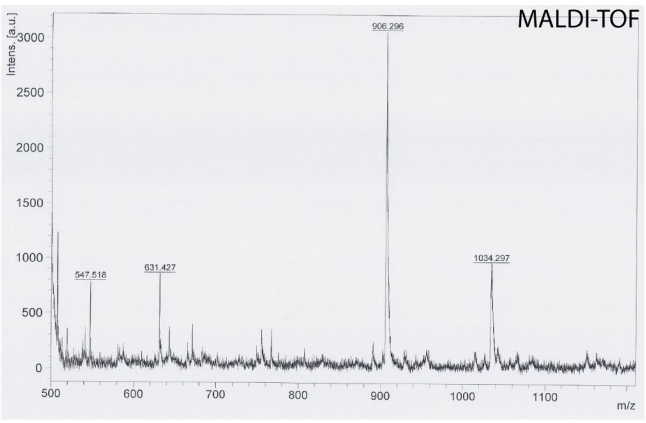

HPLC (RP-18, detection @214nm)

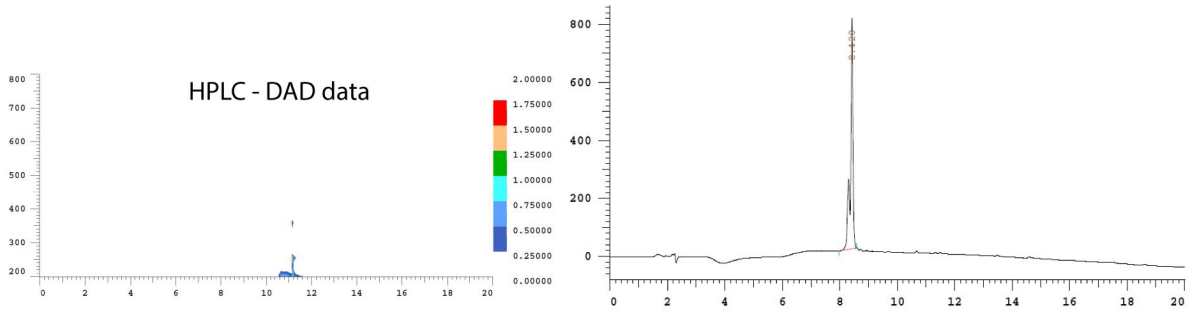

K_3-STOTDA-acridine. MALDI-TOF: $[M+H]^+$ calc. 910,5 $[M+H]^+$ found 906.3
RP-18 HPLC: peak@8.42 min.

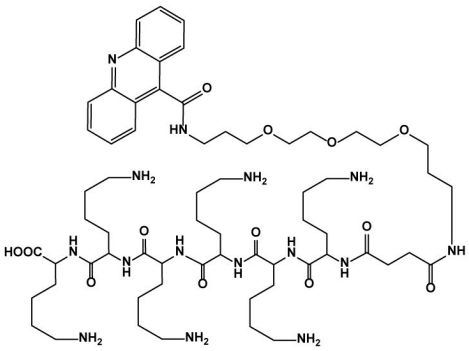

K_6-STOTDA-acridine

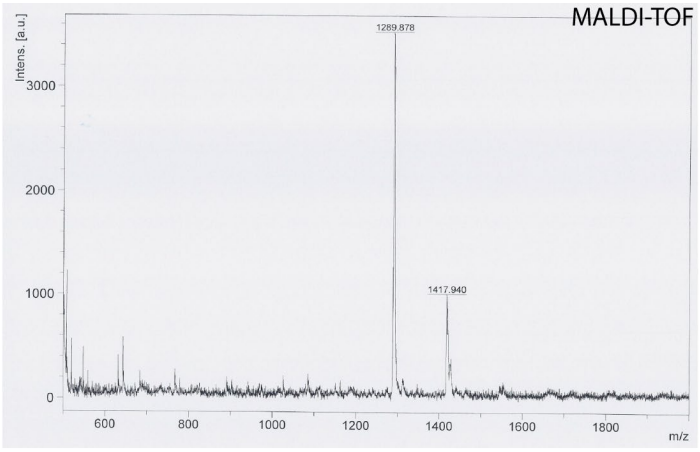

HPLC (RP-18, detection @214nm)

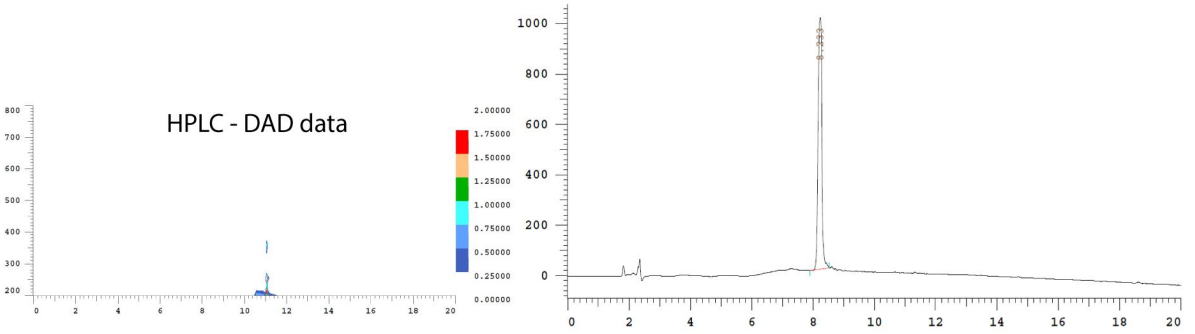

K_6-STOTDA-acridine. MALDI-TOF: $[M+H]^+$ calc. 1294.8 $[M+H]^+$ found 1289.9
RP-18 HPLC: peak@8.233 min.

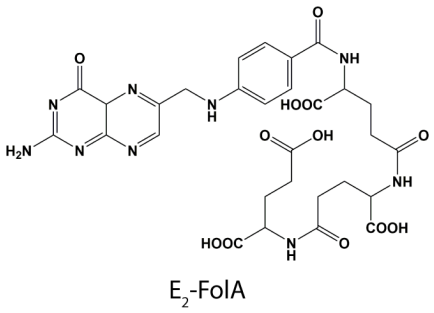

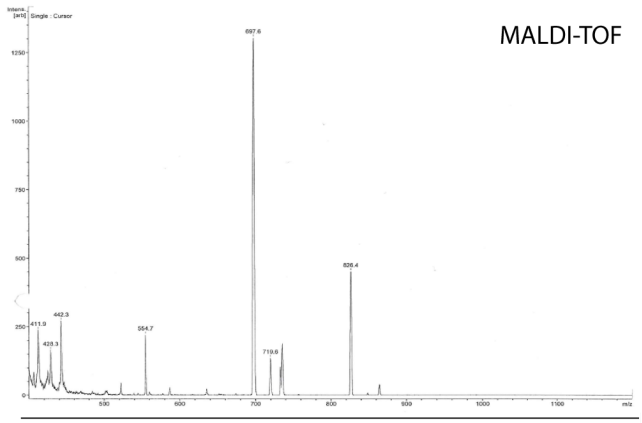

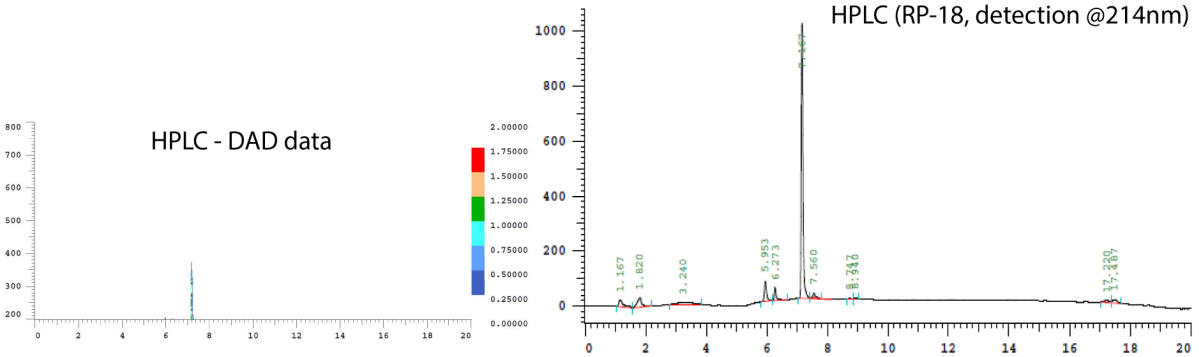

E_2-Folate. MALDI-TOF: [M+H]+ calc. 700.2 [M+H]+ found 697.6 and 719.6 [M+Na]+
RP-18 HPLC: peak@7.167 min.

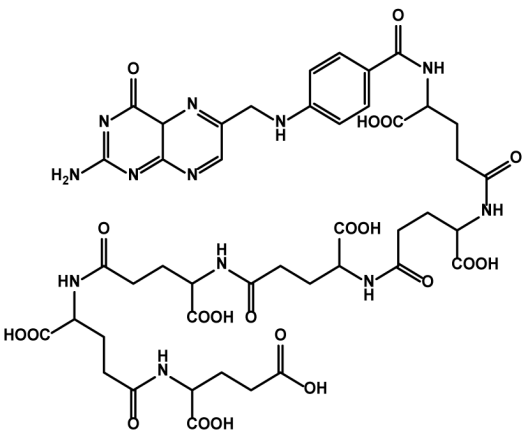

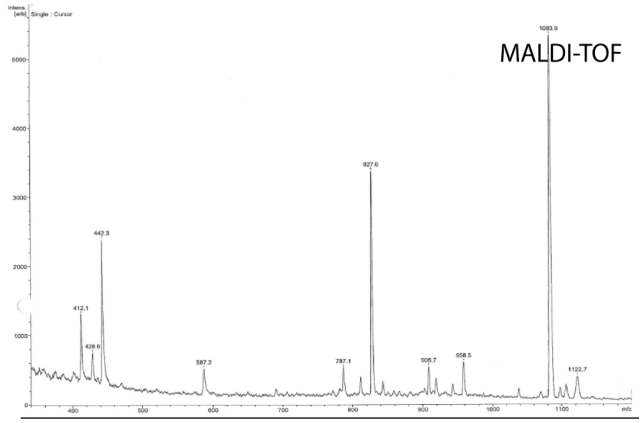

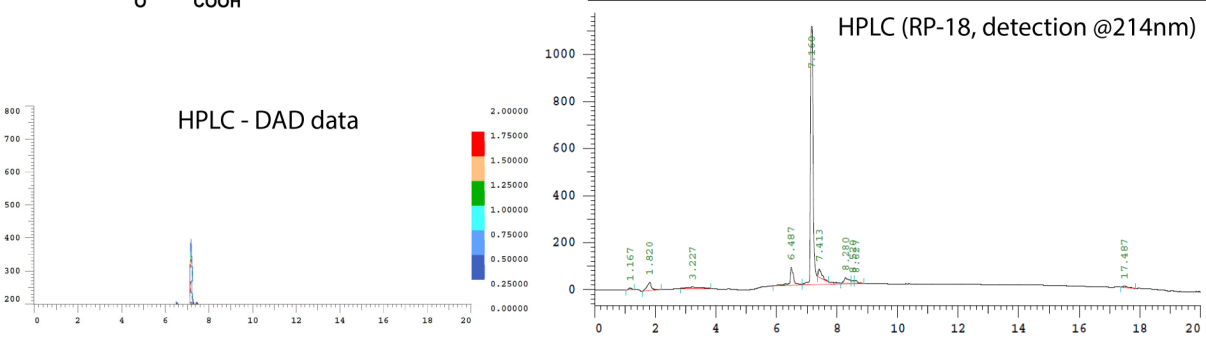

E_5-Folate. MALDI-TOF: [M+H]+ calc. 1087.3 [M+H]+ found 1083.9
RP-18 HPLC: peak@7.160 min.

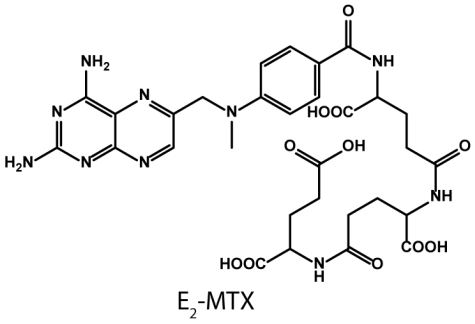

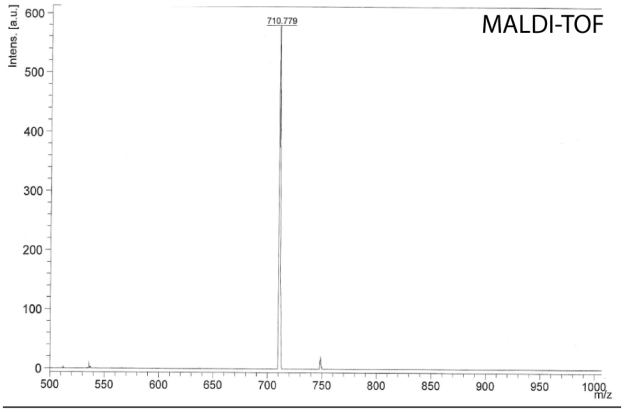

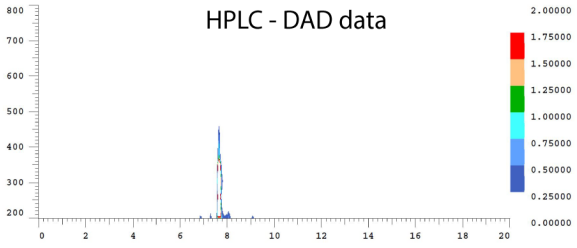

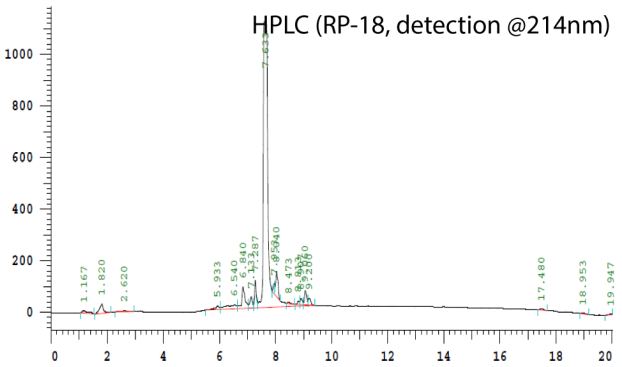

E_2-MTX. MALDI-TOF: [M+H]+ calc. 713.26 [M+H]+ found 710.78
RP-18 HPLC: peak@7.633 min.

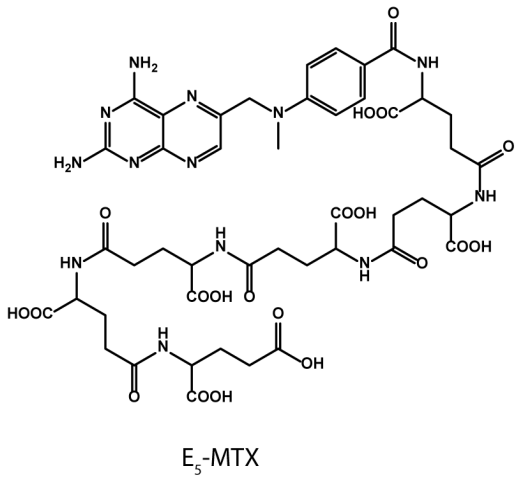

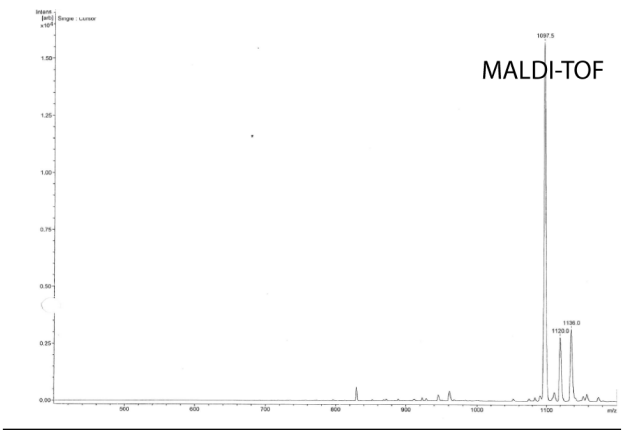

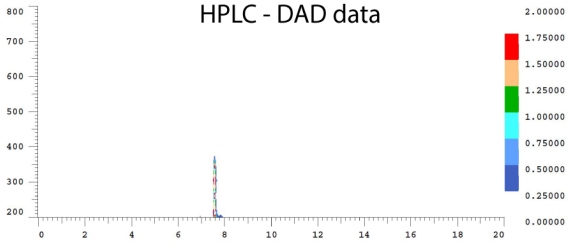

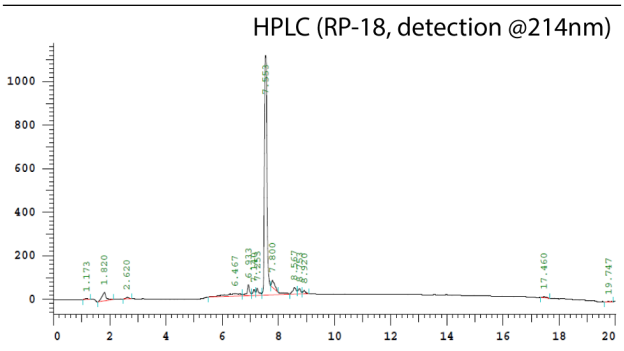

E_5-MTX. MALDI-TOF: [M+H]+ calc. 1100.38 [M+H]+ found 1097.5 and 1120 [M+Na]+
RP-18 HPLC: peak@7.553 min.

7 References

[1] V. Kontis, J. E. Bennett, C. D. Mathers, G. Li, K. Foreman, M. Ezzati, *Lancet (London, England)* **2017**, 389, 1323.

[2] P. D. Sasieni, J. Shelton, N. Ormiston-Smith, C. S. Thomson, P. B. Silcocks, *British Journal of Cancer* **2011**, 105, 460.

[3] J. K. Pedersen, G. Engholm, A. Skytthe, K. Christensen, R. Academy of Geriatric Cancer, *Acta Oncol* **2016**, 55 Suppl 1, 7.

[4] M. Lismont, L. Dreesen, S. Wuttke, *Advanced Functional Materials* **2017**, 27, 1606314.

[5] A. M. Scott, J. D. Wolchok, L. J. Old, *Nature Reviews Cancer* **2012**, 12, 278.

[6] F. M. Ferguson, N. S. Gray, *Nature Reviews Drug Discovery* **2018**, 17, 353.

[7] R. R. Weichselbaum, H. Liang, L. Deng, Y.-X. Fu, *Nature Reviews Clinical Oncology* **2017**, 14, 365.

[8] V. Velcheti, K. Schalper, *American Society of Clinical Oncology educational book. American Society of Clinical Oncology. Annual Meeting* **2016**, 35, 298.

[9] D. Castanotto, C. A. Stein, *Current Opinion in Oncology* **2014**, 26, 584.

[10] K. Cho, X. Wang, S. Nie, Z. G. Chen, D. M. Shin, *Clinical Cancer Research : an official journal of the American Association for Cancer Research* **2008**, 14, 1310.

[11] a) A. M. Rahman, S. W. Yusuf, M. S. Ewer, *International Journal of Nanomedicine* **2007**, 2, 567; b) A. Wicki, D. Witzigmann, V. Balasubramanian, J. Huwyler, *Journal of Controlled Release* **2015**, 200, 138.

[12] I. Freestone, N. Meeks, M. Sax, C. Higgitt, *Gold Bulletin* **2007**, 40, 270.

[13] M. Reibold, N. Pätzke, A. A. Levin, W. Kochmann, I. P. Shakhverdova, P. Paufler, D. C. Meyer, *Crystal Research and Technology* **2009**, 44, 1139.

[14] a) P. S. Gill, J. Wernz, D. T. Scadden, P. Cohen, G. M. Mukwaya, J. H. von Roenn, M. Jacobs, S. Kempin, I. Silverberg, G. Gonzales, M. U. Rarick, A. M. Myers, F. Shepherd, C. Sawka, M. C. Pike, M. E. Ross, *Journal of Clinical Oncology : Official Journal of the American Society of Clinical Oncology* **1996**, 14, 2353; b) W. J. Gradishar, S. Tjulandin, N. Davidson, H. Shaw, N. Desai, P. Bhar, M. Hawkins, J. O'Shaughnessy, *Journal of Clinical Oncology : Official Journal of the American Society of Clinical Oncology* **2005**, 23, 7794.

[15] N. R. H. Stone, T. Bicanic, R. Salim, W. Hope, *Drugs* **2016**, 76, 485.

[16] P. A. Bovier, *Expert Review of Vaccines* **2008**, 7, 1141.

[17] K. M. Day, N. M. Nair, D. Griner, L. A. Sargent, *The Journal of Craniofacial Surgery* **2018**, 29, 726.

[18] C. Fenton, C. M. Perry, *Drugs & aging* **2006**, 23, 421.

[19] Y.-X. J. Wang, *World J Gastroenterol* **2015**, 21, 13400.

[20] a) A. C. Anselmo, S. Mitragotri, *Bioengineering & Translational Medicine* **2016**, 1, 10; b) D. Bobo, K. J. Robinson, J. Islam, K. J. Thurecht, S. R. Corrie, *Pharmaceutical Research* **2016**, 33, 2373.

[21] D. Peer, J. M. Karp, S. Hong, O. C. Farokhzad, R. Margalit, R. Langer, *Nature Nanotechnology* **2007**, 2, 751.

[22] J. Han, S. S. Davis, C. Washington, *International Journal of Pharmaceutics* **2001**, 215, 207.

[23] M. Narvekar, H. Y. Xue, J. Y. Eoh, H. L. Wong, *AAPS PharmSciTech* **2014**, 15, 822.

[24] D. Rosenblum, N. Joshi, W. Tao, J. M. Karp, D. Peer, *Nature Communications* **2018**, 9, 1410.

[25] K. Liang, R. Ricco, C. M. Doherty, M. J. Styles, S. Bell, N. Kirby, S. Mudie, D. Haylock, A. J. Hill, C. J. Doonan, P. Falcaro, *Nature Communications* **2015**, 6, 7240.

[26] S. Wilhelm, A. J. Tavares, Q. Dai, S. Ohta, J. Audet, H. F. Dvorak, W. C. W. Chan, *Nature Reviews Materials* **2016**, 1, 16014.

[27] J. Fang, H. Nakamura, H. Maeda, *Adv Drug Deliv Rev* **2011**, 63, 136.

[28] a) H. S. Choi, W. Liu, P. Misra, E. Tanaka, J. P. Zimmer, B. Itty Ipe, M. G. Bawendi, J. V. Frangioni, *Nat Biotechnol* **2007**, 25, 1165; b) M. Yu, J. Zheng, *ACS Nano* **2015**, 9, 6655.

[29] X. Dong, *Theranostics* **2018**, 8, 1481.

[30] M. Yoshida, R. Takimoto, K. Murase, Y. Sato, M. Hirakawa, F. Tamura, T. Sato, S. Iyama, T. Osuga, K. Miyanishi, K. Takada, T. Hayashi, M. Kobune, J. Kato, *PloS one* **2012**, 7, e39545.

[31] S. Azarmi, W. H. Roa, R. Lobenberg, *Advanced Drug Delivery Reviews* **2008**, 60, 863.

[32] a) D. Chen, S. Ganesh, W. Wang, M. Amiji, *Nanoscale* **2019**, 11, 8760; b) F. Chen, G. Wang, J. I. Griffin, B. Brenneman, N. K. Banda, V. M. Holers, D. S. Backos, L. Wu, S. M. Moghimi, D. Simberg, *Nature Nanotechnology* **2016**, 12, 387.

[33] E. Frohlich, *Int J Nanomedicine* **2012**, 7, 5577.
[34] S. M. Moghimi, *Biochimica et Biophysica Acta (BBA) - Molecular Cell Research* **2002**, 1590, 131.
[35] J. S. Suk, Q. Xu, N. Kim, J. Hanes, L. M. Ensign, *Advanced Drug Delivery Reviews* **2016**, 99, 28.
[36] T. Wu, Y. Dai, *Cancer letters* **2017**, 387, 61.
[37] a) T. Boulikas, *Expert Opinion on Investigational Drugs* **2009**, 18, 1197; b) C. F. Jehn, T. Boulikas, A. Kourvetaris, G. Kofla, K. Possinger, D. Luftner, *Anticancer Research* **2008**, 28, 3961.
[38] A. Wang-Gillam, R. A. Hubner, J. T. Siveke, D. D. Von Hoff, B. Belanger, F. A. de Jong, B. Mirakhur, L. T. Chen, *European Journal of Cancer (Oxford, England : 1990)* **2019**, 108, 78.
[39] M. E. O'Brien, N. Wigler, M. Inbar, R. Rosso, E. Grischke, A. Santoro, R. Catane, D. G. Kieback, P. Tomczak, S. P. Ackland, F. Orlandi, L. Mellars, L. Alland, C. Tendler, *Annals of Oncology : Official Journal of the European Society for Medical Oncology* **2004**, 15, 440.
[40] Centerwatch, FDA-approved chemotherapeutics, https://www.centerwatch.com/drug-information/fda-approved-drugs/therapeutic-area/12/oncology, accessed on November 3rd, 2019.
[41] a) M. Eddaoudi, D. B. Moler, H. Li, B. Chen, T. M. Reineke, M. O'Keeffe, O. M. Yaghi, *Acc Chem Res* **2001**, 34, 319; b) B. F. Hoskins, R. Robson, *Journal of the American Chemical Society* **1989**, 111, 5962; c) H. Li, M. Eddaoudi, M. O'Keeffe, O. M. Yaghi, *Nature* **1999**, 402, 276; d) O. M. Yaghi, M. O'Keeffe, N. W. Ockwig, H. K. Chae, M. Eddaoudi, J. Kim, *Nature* **2003**, 423, 705; e) O. M. Yaghi, D. A. Richardson, G. Li, C. E. Davis, T. L. Groy, *MRS Proceedings* **1994**, 371, 15.
[42] a) P. Horcajada, R. Gref, T. Baati, P. K. Allan, G. Maurin, P. Couvreur, G. Férey, R. E. Morris, C. Serre, *Chemical Reviews* **2012**, 112, 1232; b) P. Z. Moghadam, A. Li, S. B. Wiggin, A. Tao, A. G. P. Maloney, P. A. Wood, S. C. Ward, D. Fairen-Jimenez, *Chemistry of Materials* **2017**, 29, 2618.
[43] S. M. J. Rogge, A. Bavykina, J. Hajek, H. Garcia, A. I. Olivos-Suarez, A. Sepúlveda-Escribano, A. Vimont, G. Clet, P. Bazin, F. Kapteijn, M. Daturi, E. V. Ramos-Fernandez, F. X. Llabrés i Xamena, V. Van Speybroeck, J. Gascon, *Chemical Society Reviews* **2017**, 46, 3134.
[44] Y. He, W. Zhou, G. Qian, B. Chen, *Chemical Society Reviews* **2014**, 43, 5657.
[45] K. Adil, Y. Belmabkhout, R. S. Pillai, A. Cadiau, P. M. Bhatt, A. H. Assen, G. Maurin, M. Eddaoudi, *Chemical Society Reviews* **2017**, 46, 3402.
[46] L. E. Kreno, K. Leong, O. K. Farha, M. Allendorf, R. P. Van Duyne, J. T. Hupp, *Chemical reviews* **2012**, 112, 1105.
[47] a) I. Abanades Lazaro, S. Haddad, S. Sacca, C. Orellana-Tavra, D. Fairen-Jimenez, R. S. Forgan, *Chem* **2017**, 2, 561; b) C. He, K. Lu, D. Liu, W. Lin, *Journal of the American Chemical Society* **2014**, 136, 5181; c) R. C. Huxford, J. Della Rocca, W. Lin, *Current Opinion in Chemical Biology* **2010**, 14, 262; d) T. Simon-Yarza, M. Gimenez-Marques, R. Mrimi, A. Mielcarek, R. Gref, P. Horcajada, C. Serre, P. Couvreur, *Angew Chem Int Ed Engl* **2017**, 56, 15565; e) L. Wang, M. Zheng, Z. Xie, *Journal of Materials Chemistry B* **2018**, 6, 707; f) M.-X. Wu, Y.-W. Yang, *Advanced Materials* **2017**, 29, 1606134.
[48] C.-C. Chueh, C.-I. Chen, Y.-A. Su, H. Konnerth, Y.-J. Gu, C.-W. Kung, K. C. W. Wu, *Journal of Materials Chemistry A* **2019**, 7, 17079.
[49] a) J. Della Rocca, W. Lin, *European Journal of Inorganic Chemistry* **2010**, 2010, 3725; b) P. Horcajada, T. Chalati, C. Serre, B. Gillet, C. Sebrie, T. Baati, J. F. Eubank, D. Heurtaux, P. Clayette, C. Kreuz, J. S. Chang, Y. K. Hwang, V. Marsaud, P. N. Bories, L. Cynober, S. Gil, G. Ferey, P. Couvreur, R. Gref, *Nature Materials* **2010**, 9, 172.
[50] A. E. Baumann, D. A. Burns, B. Liu, V. S. Thoi, *Communications Chemistry* **2019**, 2, 86.
[51] E. Sperr, PubMed by Year, https://esperr.github.io/pubmed-by-year/?q1=metal organic%20framework&startyear=1990&endyear=2018, accessed on November 5th, 2019.
[52] M. Eddaoudi, D. B. Moler, H. Li, B. Chen, T. M. Reineke, M. O'Keeffe, O. M. Yaghi, *Accounts of Chemical Research* **2001**, 34, 319.
[53] M. J. Kalmutzki, N. Hanikel, O. M. Yaghi, *Science Advances* **2018**, 4, eaat9180.
[54] H. Li, M. Eddaoudi, T. L. Groy, O. M. Yaghi, *Journal of the American Chemical Society* **1998**, 120, 8571.
[55] G. Ferey, C. Mellot-Draznieks, C. Serre, F. Millange, J. Dutour, S. Surble, I. Margiolaki, *Science* **2005**, 309, 2040.
[56] K. Koh, A. G. Wong-Foy, A. J. Matzger, *Journal of the American Chemical Society* **2009**, 131, 4184.

[57] a) O. K. Farha, I. Eryazici, N. C. Jeong, B. G. Hauser, C. E. Wilmer, A. A. Sarjeant, R. Q. Snurr, S. T. Nguyen, A. Ö. Yazaydın, J. T. Hupp, *Journal of the American Chemical Society* **2012**, 134, 15016; b) I. M. Hönicke, I. Senkovska, V. Bon, I. A. Baburin, N. Bönisch, S. Raschke, J. D. Evans, S. Kaskel, *Angewandte Chemie International Edition* **2018**, 57, 13780.

[58] B. L. Dunicz, *Journal of Chemical Education* **1961**, 38, 357.

[59] E. N. Domoroshchina, V. V. Chernyshev, G. M. Kuz'Micheva, A. V. Dorokhov, L. V. Pirutko, G. V. Kravchenko, R. B. Chumakov, *Applied Nanoscience* **2018**, 8, 19.

[60] S. Keskin, S. Kızılel, *Industrial & Engineering Chemistry Research* **2011**, 50, 1799.

[61] T. Chalati, P. Horcajada, R. Gref, P. Couvreur, C. Serre, *Journal of Materials Chemistry* **2011**, 21, 2220.

[62] P. Horcajada, S. Surblé, C. Serre, D.-Y. Hong, Y.-K. Seo, J.-S. Chang, J.-M. Grenèche, I. Margiolaki, G. Férey, *Chemical Communications* **2007,** 2820-2822.

[63] M. J. Katz, Z. J. Brown, Y. J. Colón, P. W. Siu, K. A. Scheidt, R. Q. Snurr, J. T. Hupp, O. K. Farha, *Chemical Communications* **2013**, 49, 9449.

[64] S. S. Y. Chui, S. M. F. Lo, J. P. H. Charmant, A. G. Orpen, I. D. Williams, *Science* **1999**, 283, 1148.

[65] G. Wißmann, A. Schaate, S. Lilienthal, I. Bremer, A. M. Schneider, P. Behrens, *Microporous and Mesoporous Materials* **2012**, 152, 64.

[66] a) A. Albanese, P. S. Tang, W. C. W. Chan, *Annual Review of Biomedical Engineering* **2012**, 14, 1; b) B. D. Chithrani, A. A. Ghazani, W. C. Chan, *Nano Lett* **2006**, 6, 662; c) C. Orellana-Tavra, S. A. Mercado, D. Fairen-Jimenez, *Advanced Healthcare Materials* **2016**, 5, 2261.

[67] Z. Ni, R. I. Masel, *J Am Chem Soc* **2006**, 128, 12394.

[68] E. Biemmi, S. Christian, N. Stock, T. Bein, *Microporous and Mesoporous Materials* **2009**, 117, 111.

[69] M. Ma, D. Zacher, X. Zhang, R. A. Fischer, N. Metzler-Nolte, *Crystal Growth & Design* **2011**, 11, 185.

[70] J. Cravillon, R. Nayuk, S. Springer, A. Feldhoff, K. Huber, M. Wiebcke, *Chemistry of Materials* **2011**, 23, 2130.

[71] S. Wang, M. Wahiduzzaman, L. Davis, A. Tissot, W. Shepard, J. Marrot, C. Martineau-Corcos, D. Hamdane, G. Maurin, S. Devautour-Vinot, C. Serre, *Nature Communications* **2018**, 9, 4937.

[72] G. Zhang, G. Wei, Z. Liu, S. R. J. Oliver, H. Fei, *Chemistry of Materials* **2016**, 28, 6276.

[73] J. Ren, N. M. Musyoka, H. W. Langmi, T. Segakweng, B. C. North, M. Mathe, X. Kang, *International Journal of Hydrogen Energy* **2014**, 39, 12018.

[74] Q.-H. Tan, Y.-Q. Wang, X.-Y. Guo, H.-T. Liu, Z.-L. Liu, *RSC Advances* **2016**, 6, 61725.

[75] K. Lu, C. He, W. Lin, *Journal of the American Chemical Society* **2014**, 136, 16712.

[76] D. K. Singha, P. Majee, S. K. Mondal, P. Mahata, *Journal of Photochemistry and Photobiology A: Chemistry* **2018**, 356, 389.

[77] M. Akram, *Cell biochemistry and biophysics* **2014**, 68, 475.

[78] C. Tamames-Tabar, D. Cunha, E. Imbuluzqueta, F. Ragon, C. Serre, M. J. Blanco-Prieto, P. Horcajada, *Journal of Materials Chemistry B* **2014**, 2, 262.

[79] S. Wuttke, A. Zimpel, T. Bein, S. Braig, K. Stoiber, A. Vollmar, D. Müller, K. Haastert-Talini, J. Schaeske, M. Stiesch, G. Zahn, A. Mohmeyer, P. Behrens, O. Eickelberg, D. A. Bölükbas, S. Meiners, *Advanced Healthcare Materials* **2017**, 6.

[80] T. Baati, L. Njim, F. Neffati, A. Kerkeni, M. Bouttemi, R. Gref, M. F. Najjar, A. Zakhama, P. Couvreur, C. Serre, P. Horcajada, *Chemical Science* **2013**, 4, 1597.

[81] T. Simon-Yarza, M. Giménez-Marqués, R. Mrimi, A. Mielcarek, R. Gref, P. Horcajada, C. Serre, P. Couvreur, *Angewandte Chemie* **2017**, 129, 15771.

[82] A. Phan, C. J. Doonan, F. J. Uribe-Romo, C. B. Knobler, M. O'Keeffe, O. M. Yaghi, *Accounts of Chemical Research* **2010**, 43, 58.

[83] A. Ruyra, A. Yazdi, J. Espin, A. Carne-Sanchez, N. Roher, J. Lorenzo, I. Imaz, D. Maspoch, *Chemistry* **2015**, 21, 2508.

[84] E. Bellido, T. Hidalgo, M. V. Lozano, M. Guillevic, R. Simon-Vazquez, M. J. Santander-Ortega, A. Gonzalez-Fernandez, C. Serre, M. J. Alonso, P. Horcajada, *Advanced Healthcare Materials* **2015**, 4, 1246.

[85] A. Zimpel, N. Al Danaf, B. Steinborn, J. Kuhn, M. Höhn, T. Bauer, P. Hirschle, W. Schrimpf, H. Engelke, E. Wagner, M. Barz, D. C. Lamb, U. Lächelt, S. Wuttke, *ACS Nano* **2019**, 13, 3884.

[86] J.-P. Zhang, H.-L. Zhou, D.-D. Zhou, P.-Q. Liao, X.-M. Chen, *National Science Review* **2017**, 5, 907.

[87] W. Lin, Q. Hu, K. Jiang, Y. Yang, Y. Yang, Y. Cui, G. Qian, *Journal of Solid State Chemistry* **2016**, 237, 307.

[88] a) W. Xu, Y. Lou, W. Chen, Y. Kang, *Biomedical Engineering / Biomedizinische Technik*, 0, 2019;
b) T. Xue, C. Xu, Y. Wang, Y. Wang, H. Tian, Y. Zhang, *Biomaterials Science* **2019**, 7, 4615.
[89] B. Miri, N. Motakef-Kazemi, S. A. Shojaosadati, A. Morsali, *Iran J Pharm Res* **2018**, 17, 1164.
[90] Y.-F. Song, L. Cronin, *Angewandte Chemie International Edition* **2008**, 47, 4635.
[91] M. E. Braun, C. D. Steffek, J. Kim, P. G. Rasmussen, O. M. Yaghi, *Chemical Communications* **2001**, 2532-2533.
[92] M. Eddaoudi, J. Kim, N. Rosi, D. Vodak, J. Wachter, M. O'Keeffe, O. M. Yaghi, *Science* **2002**, 295, 469.
[93] F. Vermoortele, R. Ameloot, A. Vimont, C. Serre, D. De Vos, *Chemical Communications* **2011**, 47, 1521.
[94] K. K. Tanabe, Z. Wang, S. M. Cohen, *Journal of the American Chemical Society* **2008**, 130, 8508.
[95] U. Fluch, B. D. McCarthy, S. Ott, *Dalton Transactions* **2019**, 48, 45.
[96] R. Röder, T. Preiß, P. Hirschle, B. Steinborn, A. Zimpel, M. Höhn, J. O. Rädler, T. Bein, E. Wagner, S. Wuttke, U. Lächelt, *Journal of the American Chemical Society* **2017**, 139, 2359.
[97] J. Liu, L. Chen, H. Cui, J. Zhang, L. Zhang, C.-Y. Su, *Chemical Society Reviews* **2014**, 43, 6011.
[98] M. E. Kimple, A. L. Brill, R. L. Pasker, *Current Protocols in Protein Science* **2013**, 73, Unit-9.9.
[99] K. Lu, C. He, W. Lin, *Journal of the American Chemical Society* **2015**, 137, 7600.
[100] M. Peller, K. Böll, A. Zimpel, S. Wuttke, *Inorganic Chemistry Frontiers* **2018**, 5, 1760.
[101] K. Ni, G. Lan, C. Chan, B. Quigley, K. Lu, T. Aung, N. Guo, P. La Riviere, R. R. Weichselbaum, W. Lin, *Nature Communications* **2018**, 9.
[102] C. He, D. Liu, W. Lin, *Chemical Reviews* **2015**, 115, 11079.
[103] J. Hungerford, K. S. Walton, *Inorganic Chemistry* **2019**, 58, 7690.
[104] D. Liu, S. A. Kramer, R. C. Huxford-Phillips, S. Wang, J. Della Rocca, W. Lin, *Chemical Communications (Cambridge, England)* **2012**, 48, 2668.
[105] a) N. C. Burtch, H. Jasuja, K. S. Walton, *Chemical Reviews* **2014**, 114, 10575; b) M. Ding, X. Cai, H.-L. Jiang, *Chemical Science* **2019**, 10, 10209.
[106] a) B. Steinborn, P. Hirschle, M. Höhn, T. Bauer, M. Barz, S. Wuttke, E. Wagner, U. Lächelt, *Advanced Therapeutics* **2019**, 2, 1900120; b) W. J. Rieter, K. M. Pott, K. M. Taylor, W. Lin, *Journal of the American Chemical Society* **2008**, 130, 11584; c) R. C. Huxford, K. E. Dekrafft, W. S. Boyle, D. Liu, W. Lin, *Chem Sci* **2012**, 3; d) C. He, C. Poon, C. Chan, S. D. Yamada, W. Lin, *Journal of the American Chemical Society* **2016**, 138, 6010; e) C. He, X. Duan, N. Guo, C. Chan, C. Poon, R. R. Weichselbaum, W. Lin, *Nature Communications* **2016**, 7, 12499.
[107] B. Steinborn, U. Lächelt, *Pharmaceutical Nanotechnology, manuscript submitted.*
[108] a) C. He, D. Liu, W. Lin, *ACS Nano* **2015**, 9, 991; b) R. C. Huxford-Phillips, S. R. Russell, D. Liu, W. Lin, *RSC Advances* **2013**, 3, 14438.
[109] P. F. Gao, L. L. Zheng, L. J. Liang, X. X. Yang, Y. F. Li, C. Z. Huang, *Journal of Materials Chemistry B* **2013**, 1, 3202.
[110] L. Tang, J. Shi, X. Wang, S. Zhang, H. Wu, H. Sun, Z. Jiang, *Nanotechnology* **2017**, 28, 275601.
[111] Z. He, P. Zhang, Y. Xiao, J. Li, F. Yang, Y. Liu, J.-R. Zhang, J.-J. Zhu, *Nano Research* **2018**, 11, 929.
[112] Y. Yang, L. Xu, W. Zhu, L. Feng, J. Liu, Q. Chen, Z. Dong, J. Zhao, Z. Liu, M. Chen, *Biomaterials* **2018**, 156, 121.
[113] R. Freund, U. Lächelt, T. Gruber, B. Ruhle, S. Wuttke, *ACS Nano* **2018**, 12, 2094.
[114] J. Cao, X. Li, H. Tian, *Current medicinal chemistry* **2019**, DOI: 10.2174/0929867326666190618152518.
[115] C. Zylberberg, S. Matosevic, *Drug Deliv* **2016**, 23, 3319.
[116] X.-Y. Zhang, P.-Y. Zhang, **2016**, 12, 1.
[117] a) L. Xing, H. Zheng, S. Che, *Chemistry* **2011**, 17, 7271; b) B. Steinborn, P. Hirschle, M. Höhn, T. Bauer, M. Barz, S. Wuttke, E. Wagner, U. Lächelt, *Advanced Therapeutics* **2019**, 2, 1900120 c) J. G. Heck, C. Feldmann, *Journal of Colloid and Interface Science* **2016**, 481, 69.
[118] a) K. Han, W.-Y. Zhang, J. Zhang, Z.-Y. Ma, H.-Y. Han, *Advanced Healthcare Materials* **2017**, 6, 1700470; b) I. Imaz, M. Rubio-Martínez, L. García-Fernández, F. García, D. Ruiz-Molina, J. Hernando, V. Puntes, D. Maspoch, *Chemical Communications* **2010**, 46, 4737; c) J. Liu, G. Yang, W. Zhu, Z. Dong, Y. Yang, Y. Chao, Z. Liu, *Biomaterials* **2017**, 146, 40.
[119] a) N. N. Adarsh, C. Frias, T. M. Ponnoth Lohidakshan, J. Lorenzo, F. Novio, J. Garcia-Pardo, D. Ruiz-Molina, *Chemical Engineering Journal* **2018**, 340, 94; b) D. Liu, C. Poon, K. Lu, C. He, W. Lin, *Nature Communications* **2014**, 5, 4182; c) C. Poon, C. He, D. Liu, K. Lu, W. Lin, *Journal of Controlled Release* **2015**, 201, 90.

[120] a) J. Liu, Y. Yang, W. Zhu, X. Yi, Z. Dong, X. Xu, M. Chen, K. Yang, G. Lu, L. Jiang, Z. Liu, *Biomaterials* **2016**, 97, 1; b) Y. Yang, W. Zhu, L. Feng, Y. Chao, X. Yi, Z. Dong, K. Yang, W. Tan, Z. Liu, M. Chen, *Nano Lett* **2018**, 18, 6867.
[121] E. Lecumberri, Y. M. Dupertuis, R. Miralbell, C. Pichard, *Clinical Nutrition* **2013**, 32, 894.
[122] J. Liu, Q. Chen, W. Zhu, X. Yi, Y. Yang, Z. Dong, Z. Liu, *Advanced Functional Materials* **2017**, 27, 1605926.
[123] a) G. Gatta, L. Botta, S. Rossi, T. Aareleid, M. Bielska-Lasota, J. Clavel, N. Dimitrova, Z. Jakab, P. Kaatsch, B. Lacour, S. Mallone, R. Marcos-Gragera, P. Minicozzi, M.-J. Sánchez-Pérez, M. Sant, M. Santaquilani, C. Stiller, A. Tavilla, A. Trama, O. Visser, R. Peris-Bonet, *The Lancet Oncology* **2014**, 15, 35; b) W. A. Kamps, K. M. van der Pal-de Bruin, A. J. P. Veerman, M. Fiocco, M. Bierings, R. Pieters, *Leukemia* **2010**, 24, 309.
[124] K. Al-Saleh, C. Quinton, P. M. Ellis, *Current Oncology (Toronto, Ont.)* **2012**, 19, e9.
[125] H. Montaudie, E. Sbidian, C. Paul, A. Maza, A. Gallini, S. Aractingi, F. Aubin, H. Bachelez, B. Cribier, P. Joly, D. Jullien, M. Le Maitre, L. Misery, M. A. Richard, J. P. Ortonne, *Journal of the European Academy of Dermatology and Venereology : JEADV* **2011**, 25 Suppl 2, 12.
[126] M. A. Lopez-Olivo, H. R. Siddhanamatha, B. Shea, P. Tugwell, G. A. Wells, M. E. Suarez-Almazor, *The Cochrane database of systematic reviews* **2014**, DOI: 10.1002/14651858.CD000957.pub2Cd000957.
[127] H. K. Mitchell, E. E. Snell, R. J. Williams, *Journal of the American Chemical Society* **1941**, 63, 2284.
[128] J. Walling, *Investigational New Drugs* **2006**, 24, 37.
[129] S. Farber, L. K. Diamond, R. D. Mercer, R. F. Sylvester, J. A. Wolff, *New England Journal of Medicine* **1948**, 238, 787.
[130] R. Hertz, M. C. Li, D. B. Spencer, *Proceedings of the Society for Experimental Biology and Medicine. Society for Experimental Biology and Medicine (New York, N.Y.)* **1956**, 93, 361.
[131] M. J. Spinella, K. E. Brigle, E. E. Sierra, I. D. Goldman, The *Journal of Biological Chemistry* **1995**, 270, 7842.
[132] J. A. Moscow, *Leukemia & lymphoma* **1998**, 30, 215.
[133] E. Giovannetti, P. A. Zucali, Y. G. Assaraf, N. Funel, M. Gemelli, M. Stark, E. Thunnissen, Z. Hou, I. B. Muller, E. A. Struys, M. Perrino, G. Jansen, L. H. Matherly, G. J. Peters, *Annals of Oncology : Official Journal of the European Society for Medical Oncology* **2017**, 28, 2725.
[134] D. C. Rees, E. Johnson, O. Lewinson, *Nature Reviews Molecular Cell Biology* **2009**, 10, 218.
[135] E. L. Volk, E. Schneider, *Cancer research* **2003**, 63, 5538.
[136] a) B. A. Chabner, C. J. Allegra, G. A. Curt, N. J. Clendeninn, J. Baram, S. Koizumi, J. C. Drake, J. Jolivet, *Journal of Clinical Investigation* **1985**, 76, 907; b) M. M. J. Schoo, Z. B. Pristupa, P. J. Vickers, K. G. Scrimgeour, *Cancer research* **1985**, 45, 3034; c) M. Visentin, R. Zhao, I. D. Goldman, *Hematology/Oncology Clinics of North America* **2012**, 26, 629.
[137] R. C. Cho, P. D. Cole, K. J. Sohn, G. Gaisano, R. Croxford, B. A. Kamen, Y. I. Kim, *Molecular Cancer Therapeutics* **2007**, 6, 2909.
[138] A. A. Adjei, *Annals of Oncology : Official Journal of the European Society for Medical Oncology* **2000**, 11, 1335.
[139] T. Yamamoto, K. Shikano, T. Nanki, S. Kawai, *Scientific Reports* **2016**, 6, 35615.
[140] Y. G. Assaraf, *Cancer Metastasis Reviews* **2007**, 26, 153.
[141] E. Chu, J. C. Drake, D. Boarman, J. Baram, C. J. Allegra, *Journal of Biological Chemistry* **1990**, 265, 8470.
[142] H. B. Brooks, T. I. Meier, S. Geeganage, K. R. Fales, K. J. Thrasher, S. A. Konicek, C. D. Spencer, S. Thibodeaux, R. T. Foreman, Y.-H. Hui, K. D. Roth, Y.-W. Qian, T. Wang, S. Luo, A. Torrado, C. Si, J. L. Toth, J. R. Mc Cowan, K. Frimpong, M. R. Lee, R. D. Dally, T. A. Shepherd, T. B. Durham, Y. Wang, Z. Wu, P. W. Iversen, F. G. Njoroge, *Scientific Reports* **2018**, 8, 15458.
[143] U. Lächelt, V. Wittmann, K. Müller, D. Edinger, P. Kos, M. Hohn, E. Wagner, *Molecular Pharmaceutics* **2014**, 11, 2631.
[144] A. R. Hanauske, V. Chen, P. Paoletti, C. Niyikiza, *The Oncologist* **2001**, 6, 363.
[145] R. Zhao, I. D. Goldman, *Oncogene* **2003**, 22, 7431.
[146] S. Bhattacharjee, C. Chen, W.-S. Ahn, *RSC Advances* **2014**, 4, 52500.
[147] Y. Zhao, Q. Zhang, Y. Li, R. Zhang, G. Lu, *ACS Applied Materials & Interfaces* **2017**, 9, 15079.
[148] J. Huo, M. Brightwell, S. El Hankari, A. Garai, D. Bradshaw, *Journal of Materials Chemistry A* **2013**, 1, 15220.
[149] a) R. Holm, K. Klinker, B. Weber, M. Barz, *Macromolecular Rapid Communications* **2015**, 36, 2083; b) A. Birke, D. Huesmann, A. Kelsch, M. Weilbächer, J. Xie, M. Bros, T. Bopp, C. Becker, K. Landfester, M. Barz, *Biomacromolecules* **2014**, 15, 548.

[150] a) J. Yoo, A. Birke, J. Kim, Y. Jang, S. Y. Song, S. Ryu, B. S. Kim, B. G. Kim, M. Barz, K. Char, *Biomacromolecules* **2018**, 19, 1602; b) O. Schäfer, K. Klinker, L. Braun, D. Huesmann, J. Schultze, K. Koynov, M. Barz, *ACS Macro Letters* **2017**, 6, 1140.

[151] D. M. Loy, P. M. Klein, R. Krzysztoń, U. Lächelt, J. O. Rädler, E. Wagner, *PeerJ Materials Science* **2019**, 1, e1.

[152] M. M. Bradford, *Analytical Biochemistry* **1976**, 72, 248.

[153] A. Zimpel, N. Al Danaf, B. Steinborn, J. Kuhn, M. Hohn, T. Bauer, P. Hirschle, W. Schrimpf, H. Engelke, E. Wagner, M. Barz, D. C. Lamb, U. Lächelt, S. Wuttke, *ACS Nano* **2019**, DOI: 10.1021/acsnano.8b06287.

[154] X. Meng, B. Gui, D. Yuan, M. Zeller, C. Wang, *Science Advances* **2016**, 2, e1600480.

[155] B. Illes, P. Hirschle, S. Barnert, V. Cauda, S. Wuttke, H. Engelke, *Chemistry of Materials* **2017**, 29, 8042.

[156] R. S. Forgan, *Dalton Transactions* **2019**, 48, 9037.

[157] M. Giménez-Marqués, E. Bellido, T. Berthelot, T. Simón-Yarza, T. Hidalgo, R. Simón-Vázquez, Á. González-Fernández, J. Avila, M. C. Asensio, R. Gref, P. Couvreur, C. Serre, P. Horcajada, *Small* **2018**, 14, 1801900.

[158] A. Zimpel, T. Preiß, R. Röder, H. Engelke, M. Ingrisch, M. Peller, J. O. Rädler, E. Wagner, T. Bein, U. Lächelt, S. Wuttke, *Chemistry of Materials* **2016**, 28, 3318.

[159] J. Liang, F. Mazur, C. Tang, X. Ning, R. Chandrawati, K. Liang, *Chemical Science* **2019**, 10, 7852.

[160] A. Huang, N. Wang, C. Kong, J. Caro, *Angewandte Chemie International Edition* **2012**, 51, 10551.

[161] C.-M. Wu, M. Rathi, S. P. Ahrenkiel, R. T. Koodali, Z. Wang, *Chemical Communications* **2013**, 49, 1223.

[162] a) S. Liu, L. Zhai, C. Li, Y. Li, X. Guo, Y. Zhao, C. Wu, *ACS Appl Mater Interfaces* **2014**, 6, 5404; b) M. D. Rowe, D. H. Thamm, S. L. Kraft, S. G. Boyes, *Biomacromolecules* **2009**, 10, 983.

[163] B. Illes, S. Wuttke, H. Engelke, *Nanomaterials (Basel, Switzerland)* **2017**, 7, 351.

[164] G. Fan, C. M. Dundas, C. Zhang, N. A. Lynd, B. K. Keitz, *ACS Appl Mater Interfaces* **2018**, 10, 18601.

[165] I. Abánades Lázaro, S. Haddad, J. M. Rodrigo-Muñoz, R. J. Marshall, B. Sastre, V. del Pozo, D. Fairen-Jimenez, R. S. Forgan, *ACS Applied Materials & Interfaces* **2018**, 10, 31146.

[166] D. Chen, D. Yang, C. A. Dougherty, W. Lu, H. Wu, X. He, T. Cai, M. E. Van Dort, B. D. Ross, H. Hong, *ACS nano* **2017**, 11, 4315.

[167] S. Hu, W. Ouyang, L. Guo, Z. Lin, X. Jiang, B. Qiu, G. Chen, *Biosensors and Bioelectronics* **2017**, 92, 718.

[168] Q. Chen, Q. He, M. Lv, Y. Xu, H. Yang, X. Liu, F. Wei, *Applied Surface Science* **2015**, 327, 77.

[169] F.-C. Tsai, Y. Xia, N. Ma, J.-J. Shi, T. Jiang, T.-C. Chiang, Z.-C. Zhang, W.-C. Tsen, *Desalination and Water Treatment* **2016**, 57, 3218.

[170] S. Wang, X. Li, Z. Zhao, Z. Li, *Adsorption Science & Technology* **2015**, 33, 279.

[171] C. Chen, M. Zhang, Q. Guan, W. Li, *Chemical Engineering Journal* **2012**, 183, 60.

[172] S. Chen, L. Wen, F. Svec, T. Tan, Y. Lv, *RSC Advances* **2017**, 7, 21205.

[173] H.-L. Liu, Y. Ho, C.-M. Hsu, *Journal of Biomolecular Structure and Dynamics* **2003**, 21, 31.

[174] G. J. Doherty, H. T. McMahon, *Annual Review of Biochemistry* **2009**, 78, 857.

[175] a) I. Abanades Lazaro, S. Haddad, J. M. Rodrigo-Munoz, R. J. Marshall, B. Sastre, V. Del Pozo, D. Fairen-Jimenez, R. S. Forgan, *ACS Appl Mater Interfaces* **2018**, 10, 31146; b) C. Arcuri, L. Monarca, F. Ragonese, C. Mecca, S. Bruscoli, S. Giovagnoli, R. Donato, O. Bereshchenko, B. Fioretti, F. Costantino, *Nanomaterials (Basel, Switzerland)* **2018**, 8, 867.

[176] M. Kandiah, M. H. Nilsen, S. Usseglio, S. Jakobsen, U. Olsbye, M. Tilset, C. Larabi, E. A. Quadrelli, F. Bonino, K. P. Lillerud, *Chemistry of Materials* **2010**, 22, 6632.

[177] J. G. Heck, C. Feldmann, *J Colloid Interface Sci* **2016**, 481, 69.

[178] X. G. Wang, Q. Cheng, Y. Yu, X. Z. Zhang, *Angewandte Chemie International Edition* **2018**, 57, 7836.

[179] E. Blanco, H. Shen, M. Ferrari, *Nature Biotechnology* **2015**, 33, 941.

[180] E. Bagherzadeh, S. M. Zebarjad, H. R. M. Hosseini, *European Journal of Inorganic Chemistry* **2018**, 2018, 1909.

[181] P. Hirschle, T. Preiß, F. Auras, A. Pick, J. Völkner, D. Valdepérez, G. Witte, W. J. Parak, J. O. Rädler, S. Wuttke, *CrystEngComm* **2016**, 18, 4359.

[182] S. Brunauer, P. H. Emmett, E. Teller, *Journal of the American Chemical Society* **1938**, 60, 309.

[183] J. G. Heck, J. Napp, S. Simonato, J. Mollmer, M. Lange, H. M. Reichardt, R. Staudt, F. Alves, C. Feldmann, *Journal of the American Chemical Society* **2015**, 137, 7329.

[184] a) Y. Kobayashi, H. Katakami, E. Mine, D. Nagao, M. Konno, L. M. Liz-Marzan, *Journal of Colloid and Interface Science* **2005**, 283, 392; b) S. Liu, M. Y. Han, *Chem Asian J* **2010**, 5, 36; c) G. Y. Xu, C. H. Zong, Y. A. Sun, X. X. Wang, N. Zhang, F. Wang, A. X. Li, Q. H. Li, *Journal of Nanoscience and Nanotechnology* **2019**, 19, 5893.

[185] R. Kishor, A. K. Ghoshal, *RSC Advances* **2016**, 6, 898.

[186] W. Stöber, A. Fink, E. Bohn, *Journal of Colloid and Interface Science* **1968**, 26, 62.

[187] C. Graf, D. L. J. Vossen, A. Imhof, A. van Blaaderen, *Langmuir* **2003**, 19, 6693.

[188] L. M. Liz-Marzán, M. Giersig, P. Mulvaney, *Langmuir* **1996**, 12, 4329.

[189] N. J. Curtin, A. N. Hughes, *The Lancet. Oncology* **2001**, 2, 298.

[190] a) F. Alexis, E. Pridgen, L. K. Molnar, O. C. Farokhzad, *Mol Pharm* **2008**, 5, 505; b) Y. Y. Khine, M. Callari, H. Lu, M. H. Stenzel, *Macromolecular Chemistry and Physics* **2016**, 217, 2302.

[191] A. Birke, D. Huesmann, A. Kelsch, M. Weilbacher, J. Xie, M. Bros, T. Bopp, C. Becker, K. Landfester, M. Barz, *Biomacromolecules* **2014**, 15, 548.

[192] a) A. Birke, J. Ling, M. Barz, *Progress in Polymer Science* **2018**, 81, 163; b) K. Klinker, M. Barz, *Macromolecular Rapid Communications* **2015**, 36, 1943; c) B. Weber, A. Birke, K. Fischer, M. Schmidt, M. Barz, *Macromolecules* **2018**, 51, 2653.

[193] D. Finsinger, J. S. Remy, P. Erbacher, C. Koch, C. Plank, *Gene Ther* **2000**, 7, 1183.

[194] a) C. He, Y. Hu, L. Yin, C. Tang, C. Yin, *Biomaterials* **2010**, 31, 3657; b) Y. Yamamoto, Y. Nagasaki, Y. Kato, Y. Sugiyama, K. Kataoka, *Journal of Controlled Release* **2001**, 77, 27.

[195] K.-H. Yeon, H. Park, S.-H. Lee, Y.-M. Park, S.-H. Lee, M. Iwamoto, *Korean Journal of Chemical Engineering* **2008**, 25, 1040.

[196] E. M. M. Manders, F. J. Verbeek, J. A. Aten, *Journal of Microscopy* **1993**, 169, 375.

[197] C. P. Leamon, P. S. Low, *Proceedings of the National Academy of Sciences* **1991**, 88, 5572.

[198] L. E. Kelemen, *International Journal of Cancer* **2006**, 119, 243.

[199] J. Sudimack, R. J. Lee, *Advanced Drug Delivery Reviews* **2000**, 41, 147.

[200] G. L. Zwicke, G. Ali Mansoori, C. J. Jeffery, *Nano Reviews* **2012**, 3, 18496.

[201] K. Müller, E. Kessel, P. M. Klein, M. Hohn, E. Wagner, *Molecular Pharmaceutics* **2016**, 13, 2332.

[202] T. R. Daniels, E. Bernabeu, J. A. Rodriguez, S. Patel, M. Kozman, D. A. Chiappetta, E. Holler, J. Y. Ljubimova, G. Helguera, M. L. Penichet, *Biochimica et Biophysica Acta* **2012**, 1820, 291.

[203] H. Block, B. Maertens, A. Spriestersbach, N. Brinker, J. Kubicek, R. Fabis, J. Labahn, F. Schafer, *Methods in Enzymology* **2009**, 463, 439.

[204] Q. Yang, A. D. Wiersum, P. L. Llewellyn, V. Guillerm, C. Serre, G. Maurin, *Chemical Communications* **2011**, 47, 9603.

[205] S. E. Wheeler, J. W. G. Bloom, *The Journal of Physical Chemistry A* **2014**, 118, 6133.

[206] A. H. Ibrahim, W. A. El-Mehalmey, R. R. Haikal, M. E. A. Safy, M. Amin, H. R. Shatla, S. G. Karakalos, M. H. Alkordi, *Inorganic Chemistry* **2019**, 58, 15078.

[207] R. Mejia-Ariza, J. Huskens, *Journal of Materials Chemistry B* **2016**, 4, 1108.

[208] V. Gaberc-Porekar, V. Menart, *Journal of Biochemical and Biophysical Methods* **2001**, 49, 335.

[209] N. T. Xuan Huynh, O. M. Na, V. Chihaia, D. N. Son, *RSC Advances* **2017**, 7, 39583.

[210] T. Kline, *Handbook of Affinity Chromatography*, CRC Press, **1993**.

[211] S. D. Worrall, M. A. Bissett, P. I. Hill, A. P. Rooney, S. J. Haigh, M. P. Attfield, R. A. W. Dryfe, *Electrochimica Acta* **2016**, 222, 361.

[212] E. Hochuli, W. Bannwarth, H. Döbeli, R. Gentz, D. Stüber, *Bio/Technology* **1988**, 6, 1321.

[213] J. Porath, J. Carlsson, I. Olsson, G. Belfrage, *Nature* **1975**, 258, 598.

[214] J. Watly, E. Simonovsky, R. Wieczorek, N. Barbosa, Y. Miller, H. Kozlowski, *Inorganic Chemistry* **2014**, 53, 6675.

[215] a) Q. Jin, W. Zhu, D. Jiang, R. Zhang, C. J. Kutyreff, J. W. Engle, P. Huang, W. Cai, Z. Liu, L. Cheng, *Nanoscale* **2017**, 9, 12609; b) D. Liu, C. He, C. Poon, W. Lin, *Journal of Materials Chemistry B* **2014**, 2, 8249; c) R. Solórzano, O. Tort, J. García-Pardo, T. Escribà, J. Lorenzo, M. Arnedo, D. Ruiz-Molina, R. Alibés, F. Busqué, F. Novio, *Biomaterials Science* **2019**, 7, 178.

[216] J. Zhao, Y. Yang, X. Han, C. Liang, J. Liu, X. Song, Z. Ge, Z. Liu, *ACS Applied Materials & Interfaces* **2017**, 9, 23555.

[217] S. Suárez-García, N. Arias-Ramos, C. Frias, A. P. Candiota, C. Arús, J. Lorenzo, D. Ruiz-Molina, F. Novio, *ACS Applied Materials & Interfaces* **2018**, 10, 38819.

[218] Y. Hu, T. Lv, Y. Ma, J. Xu, Y. Zhang, Y. Hou, Z. Huang, Y. Ding, *Nano Letters* **2019**, 19, 2731.

8 Publications

Original articles (*indicates equal contributions)

B. Steinborn, P. Hirschle, M. Höhn, T. Bauer, M. Barz, S. Wuttke, E. Wagner, U. Lächelt. *Core-Shell Functionalized Zirconium-Pemetrexed Coordination Nanoparticles as Carriers with a High Drug Content*. Advanced Therapeutics **2019**, 2, 1900120.

B. Steinborn*, I. Truebenbach*, S. Morys, U. Lächelt, E. Wagner, W. Zhang. *Epidermal growth factor receptor targeted methotrexate and small interfering RNA co-delivery*. The Journal of Gene Medicine **2018**, 20, e3041.

P. Zhang, **B. Steinborn**, U. Lächelt, S. Zahler, E. Wagner. *Lipo-Oligomer Nanoformulations for Targeted Intracellular Protein Delivery*. Biomacromolecules **2017**, 18, 2509

A. Zimpel, N. Al Danaf, **B. Steinborn**, J. Kuhn, M. Höhn, T. Bauer, P. Hirschle, W. Schrimpf, H. Engelke, E. Wagner, M. Barz, D. C. Lamb, U. Lächelt, S. Wuttke. *Coordinative Binding of Polymers to Metal-Organic Framework Nanoparticles for Control of Interactions at the Biointerface*. ACS Nano **2019**, 13, 3884.

R. Röder, T. Preiß, P. Hirschle, **B. Steinborn**, A. Zimpel, M. Höhn, J. O. Rädler, T. Bein, E. Wagner, S. Wuttke, U. Lächelt. *Multifunctional Nanoparticles by Coordinative Self-Assembly of His-Tagged Units with Metal–Organic Frameworks*. Journal of the American Chemical Society **2017**, 139, 2359.

Reviews

B. Steinborn, U. Lächelt. *Metal-Organic Nanopharmaceuticals*. Pharmaceutical Nanotechnology **2020,** Manuscript accepted.

9 Acknowledgements

Now that my time as a PhD student is rapidly approaching its conclusion, it is my great pleasure to reflect upon the very nice years I've spent at our lab and express my sincere gratitude towards all the people who have actively contributed to the whole experience being so enjoyable.

First of all, I would like to thank Professor Ernst Wagner for giving me the opportunity to work on my thesis in his research group. I highly appreciate the received trust, guidance, friendly working climate and all the obtained feedback which helped me develop my personal and scientific skillset. Learning about our mutual interest in skiing and the collective skiing trips you initiated also was a pleasant surprise.

Pursuing a PhD comes with a steep learning curve and in this regard, I also owe a lot to Dr. Ulrich Lächelt – thank you for creating a great atmosphere, patiently teaching me the tricks of the trade, pointing out potential issues with experiments early on and providing good advice and additional context which was really helpful with seeing the bigger picture and developing a sense on how to conduct science efficiently. I am also grateful for the numerous discussions we've had, scientific or otherwise. They always provided new impulses and food for thought that eventually led to valuable insights.

Additionally, I want to thank Professor Stefan Wuttke for numerous passionate and always fruitful discussions. With my pharmaceutical background, initially I only had a somewhat basic grasp on the whole materials science angle regarding nanomaterials. Your patient advice and feedback helped me a lot with bridging that gap while the provided context and fresh ideas allowed for the emergence of new perspectives and directions for which I am grateful.

Miriam also contributed a lot to this thesis since she expertly handled the cell culture studies, and, along the way, taught me many practical aspects of flow cytometry and confocal microscopy. Additionally, whenever I had spontaneously concocted a new formulation to screen, you always managed to somehow find the right cell line and time to do an experiment on very short notice, thanks.

Of course, I should also acknowledge the remaining 'MOF crew', in general for the very nice atmosphere and specifically due to their individual contributions. Thanks to Dr. Ruth Röder for teaching me the basics during the early days and thanks to Dr. Patrick Hirschle and Dr. Andreas Zimpel for keeping the MOF supply flowing and showing me the practical side of XRDs and other physicochemical characterization methods I had only heard of theoretically before.

I want to thank Dr. Steffen Schmidt for all the SEM sessions and the nice discussions we've had while going through my numerous samples. Additionally, I am grateful for the detailed and patient explanations regarding the technical backgrounds and limitations of various types of electron microscopy.

Many thanks to Tobias Bauer and Dr. Matthias Barz from the Johannes Gutenberg-University Mainz for providing pGlu-*b*-pSar-N_3 which turned out to be quite essential for stabilizing my nanoparticles.

The importance of my family also cannot be overstated, I am very grateful for your continuous support which I don't take for granted. During the finest days and darkest moments, you've always had my back and it is safe to say that your encouragement and perspectives mean a lot to me. From all the families out there, by chance I was born into an especially awesome one, what are the odds.

All of my other colleagues not mentioned so far also deserve credit – thanks for being great and making sure our atmosphere was always pleasant. Especially, I would like to thank Dome for being my bench mate, Jasmin for the tasty food, Özgür for numerous thought-provoking discussions on geopolitics, philosophy, artificial intelligence, ethics, history and the Turkish perspective on life, Mina for providing insights into the Iranian mentality, Lindomar for doing the same regarding Brazil and Raneem since she helped me understand the background of Syria. Apart from the scientific exchanges, I would also like to thank PK and Sören for our discussions on cryptocurrencies – I learned a lot. Thanks to Anna for sharing a green thumb and all the plant saplings we kept exchanging, I hope the vanilla is still doing well. Thanks to Franzi, Jasmin and Simone for all the nice talks we've had and the laughs we shared while supervising the biochemistry lab courses. Thanks to all my Chinese colleagues; especially Jie, Lun, Meng and Faqian made me laugh a lot and taught me what spicy actually means, I had no idea. Thanks to Teo for professionally redecorating my desk (good one) and our countless discussions about art, although I am sorry buddy – I still think Franz von Stuck is too dark and cannot possibly compete with Franz Marc, August Macke or Gabriele Münter. Ursula, Wolfgang, Markus, Miriam and Olga made sure the lab kept on running smoothly for which I am very grateful. Additionally, thanks for all the support and friendly banter during difficult days.

Among my former students, especially Chrissi and Maike did a great job by efficiently helping me with experiments and creating a great atmosphere during their brief internship at our lab. Both of you made me laugh countless times.

Thus, it is safe to say that I will miss all of my colleagues, our atmosphere and lab a lot.